Journal of Electrical and Computer Engineering

Intelligent Control of Electrical Systems

Lead Guest Editor: Ahmed A. Zaki Diab
Guest Editors: Hamdy Soltan, Ton D. Do, and Almoataz Youssef Abdelaziz

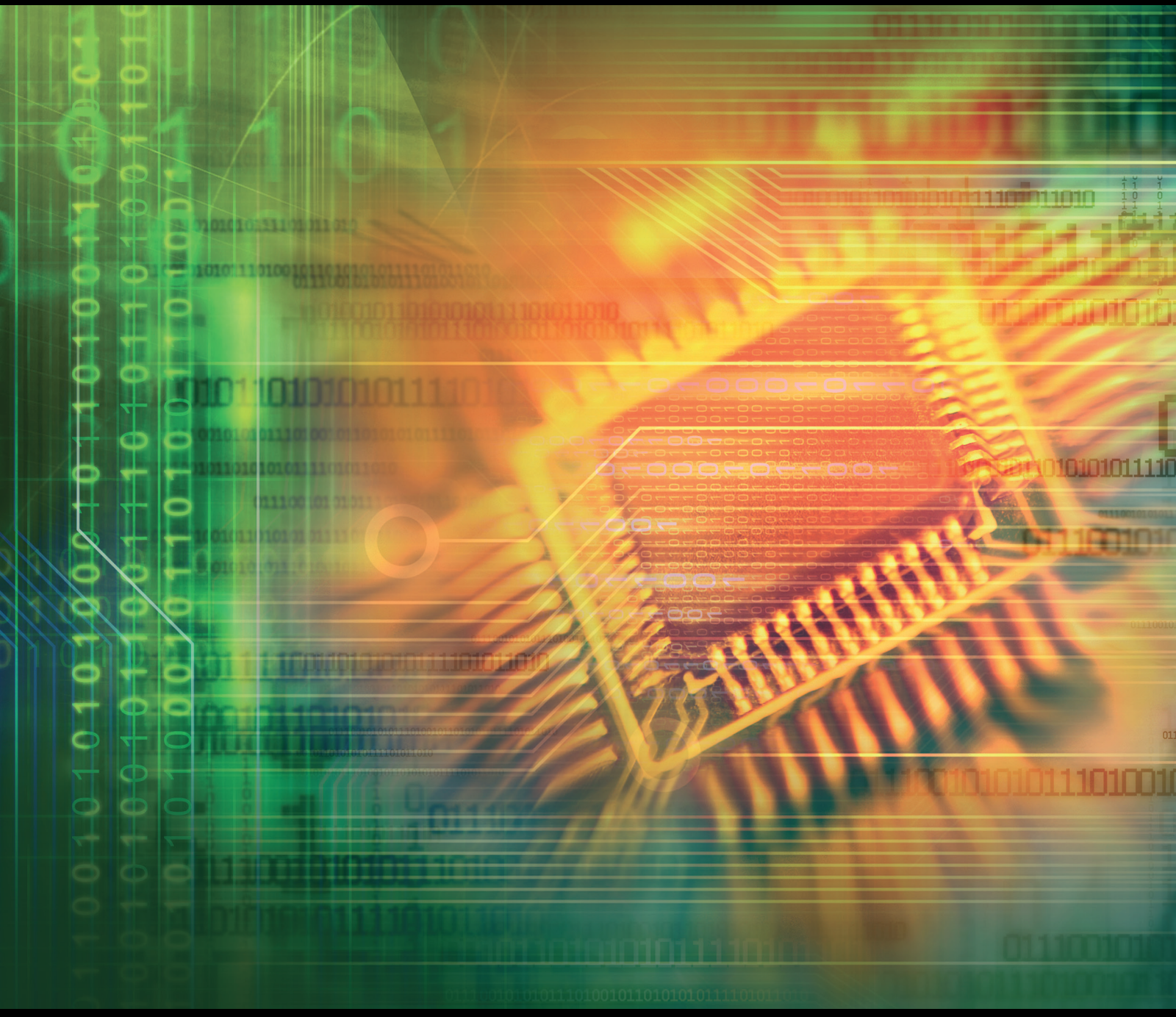

Intelligent Control of Electrical Systems

Journal of Electrical and Computer Engineering

Intelligent Control of Electrical Systems

Lead Guest Editor: Ahmed A. Zaki Diab
Guest Editors: Hamdy Soltan, Ton D. Do, and Almoataz Youssef Abdelaziz

Contents

Hindawi
Journal of Electrical and Computer Engineering
Volume 2023, Article ID 8617388, 23 pages
https://doi.org/10.1155/2023/8617388

Research Article

Synchronization and Optimal Operation of a 140 kVA Inverter in On-Grid Mode Using Mamdani Controllers in Cascade

Jesús Rodríguez-Flores,[1] **Victor Herrera-Perez**,[2] **Javier Gavilanes**,[3] **Andrés Morocho**,[4] **and Jorge Hernandez-Ambato**[4]

[1]*Universidad Regional Autónoma de Los Andes, Ambato 180101, Ecuador*
[2]*Colegio de Ciencias e Ingenierías, Universidad San Francisco de Quito-USFQ, Quito 170901, Ecuador*
[3]*Facultad de Mecánica, Escuela Superior Politécnica de Chimborazo-ESPOCH, Riobamba 060155, Ecuador*
[4]*Facultad de Informática y Electrónica, Escuela Superior Politécnica de Chimborazo-ESPOCH, Riobamba 060155, Ecuador*

Correspondence should be addressed to Victor Herrera-Perez; vherrera@usfq.edu.ec

Received 13 June 2022; Revised 29 October 2022; Accepted 24 November 2022; Published 3 February 2023

Academic Editor: Ton D. Do

This paper addresses the synchronization and operation of a 140 kVA inverter system connected to the main grid as part of a decentralized microgeneration system. The considerations for the supply of electrical energy stored in battery banks, mostly of photovoltaic origin, involve a study of the details of a rigid nonlinear system, which parallels the generation and distribution standards typical of hydroelectric and thermoelectric plants. Considering aspects related to power electronics operation, this paper presents both the modeling and the controlling aspects necessary to synchronize and ensure a stable operation of the microgeneration systems when connected to the main grid. Statistical processing was developed to guarantee synchronization between the systems without presenting electric shocks by simulating the magnetic link in asynchronous generators to meet this aim. The proposed model simulates the increase in power by a phase shift by maintaining a constant frequency based on a Chirp wave generator. The proposed process considers a generation power baseband operation. A Mamdani-type fuzzy proportional-integral controller is used to determine the power setpoint, which sets the Chirp generator phase shift setpoint, which includes a Mamdani fuzzy proportional-type controller. Both controllers are connected in a cascade. The applied correlational technique to achieve the synthesis of the sinusoid and the synchronization presented optimal performance when using 17 samples per signal period. The design of the transformer primarily, guaranteed a phase shift of −4.3018°, allowed for a THD below 2.75%.

1. Introduction

When a project on a microgeneration system is carried out, the study focuses on the primary energy source (whether wind, photovoltaic, or other), considering electronic aspects of switching and electrical regulation. However, it does not deal with issues related to interconnection with the main electric system, its implications, or possible limitations during the operation of the on-grid and off-grid switching [1].

In particular, an aspect such as regulation must be limited, since this topic is broad and in detail, many aspects must be considered. However, there are aspects to take into account that are common to any electric generation unit that needs to be synchronized with its main grid. Generally, of the four variables to be considered, such as voltage amplitude, frequency, and phase, only voltage amplitude and frequency are controlled [2]. In contrast, the phase is left relatively random until, given the conditions, the generation power switch can be closed. However, when the electric generation unit is the electronic inverter type, it can regulate and continuously monitor the three variables to be considered for synchronization [3–5]. Since these three parameters are electronically created, synchronism may be lost. The mentioned conditions differ in hydroelectric or thermoelectric generation units that keep the generating unit synchronized once the electromagnetic link is synchronized.

In the same way, the state-of-the-art of controllers for frequency control in power systems with multiple areas has been carried out using fuzzy techniques, even though the fractional component, both for the integral and differential effects, becomes less practical. This is due to weighted parameters, which are difficult to obtain with usual numerical methods and require convolution techniques that demand a lot of memory resources and computation time [6–8]. However, the tendency to incorporate studies using fuzzy logic for control to improve power quality in microgrids that use batteries and energy storage systems can be seen in works such as the one presented in [9], as well as the search for the maximum power transfer point, as shown in [10].

Likewise, studies related to voltage regulation and load sharing have been carried out for standard generation systems [11] and the case for alternative energy systems such as wind power are also being analyzed [2]. However, the appropriate way to share the load with statist systems more efficiently is still being evaluated. The research presented in [12] proposes a nonlinear way of compensating the frequency deviation in such a way that the power supplied to the system varies depending on the condition of the deviation, and it is intended to subtract weight from the compensation when the frequency deviation is too large. However, it is clear that in hybrid generation processes, whether with thermal, wind, or solar sources, compensation for power droop is present, as presented in [13].

Considering that the study on a generation system of the electronic type, where an inverter phase is involved, is similar to other electrical generation systems, the implementation of a grid frequency compensation mechanism is an aspect that must be considered during the control and operation development [4]. In particular, this factor should be considered when the aspects of operations and degree of participation in the supply of active and reactive power to the grid are analyzed. Furthermore, since partitioning with reactive energy is not commonly considered in research studies, the active power correlation study is pertinent to protecting the equipment.

Another aspect considered, in terms of protection, is the inductive nature of the transformers and the line emulated for transmission, making it necessary to propose the study and topology to provide suppressors of transient voltage peaks using MOV [5, 6].

The generation using power electronics devices distorts the voltage profile due to the low generation of reactive power and the operation in a baseband of power generation. The traditional generation from relatively low-power generation systems aims at the simple generation and injection of active power [7] without considering other aspects, such as the grid frequency variation.

Fuzzy controls based on the Mamdani approach have been widely and effectively used in various applications where they have proven their best performance compared to other classical control techniques. Wang and Li proposed a nonlinear hybrid fuzzy system by adjusting Mamdani's parameters, and their results showed that the proposed fuzzy system has better approximation performance based on the variable universe (nonlinear constraints for applications that require quick response and high stability precision) than comparing with other control systems [14].

Fuzzy controls have been successfully applied in electrical networks and distributed generation environments. Sharma et al. proposed a dual-structured fuzzy (Mamdani-based) to switch between proportional and integral actions to improve the frequency regulation in a microgrid, including a wind-diesel generator system combined with an ultra-capacitor storage unit [15]. Barakat presented a Mamdani-based fuzzy logic control to reduce load frequency control issues and step load perturbations in terms of peaks and settling time under different multisource interconnected power systems (reheat, hydro, and gas units with and without HVDC links) [16]. Fayez et al. developed a fuzzy controller to command battery energy storage and a resistor brake to mitigate subsynchronous resonance oscillatory torque and speed response in steam turbines connected to power grids. The results showed that the proposed control scheme could reduce the intensive computational burdens due to the applications of 3 fuzzy rules compared to more complex control techniques [17]. Manas et al. presented a methodology based on a Mamdani fuzzy expert system to determine the optimal sizing and placement of distributed generators in the distribution grid of Tezpur University (India), showing the effectiveness of the fuzzy algorithm in terms of loss reduction and voltage profile improvement [18].

In addition, this type of fuzzy control has shown its efficiency and improved the performance of power electronics devices. Acikgoz et al. presented a control topology for an electronic power transformer (containing a three-phase pulse width modulation rectifier that converts 800 Vrms AC to 2000 V DC bus at the input stage, a dual active bridge converter that provides a 400 V DC bus with 5:1 high-frequency transformer at the isolation stage, and a three-phase two-level inverter that is used to obtain AC output at the output stage) based on a fuzzy controller to improve compensation ability for voltage harmonics, voltage flicker, and voltage sag/swell conditions [19]. Agarwal et al. proposed a fault analysis method (fuzzy-based) for voltage source converters in high voltage direct current (HVDC) transmission lines, which probed to be better than conventional methods in terms of computational requirements, less number of protections relays, implementation complexity, and required signals with 100% accuracy discrimination of AC and DC sections faults[20].

Finally, Mamdani-type fuzzy controls have been studied as alternative techniques for classical controls of motors and generation machines. Cross and Ma compared different techniques for model-based condition monitoring systems applied in wind turbines, such as linear model, artificial neural networks, state-dependent "pseudo" transfer function, and Mamdani fuzzy-based approach, where this last technique demonstrated to be practically feasible to be implemented [21]. Errouha et al. introduce the Mamdani fuzzy logic techniques as an alternative approach to conventional direct torque control (DTC) to control induction motors for water pumping systems, where the results showed that the fuzzy control could improve the

performance by minimizing the flux and torque ripples, reducing overshoot and undershoot, and enhancing the response time [22].

The use of fuzzy inference in the protection and controller implementation process has two advantages. On the one hand, in the implementation of controllers (to generate and synchronize the inverter signal), more parameters allow for achieving the desired results with a computational cost only present during the training process. On the other hand, in correlation protection, fuzzy characterization allows implementation with elementary mathematical operations whose execution times are much lower and whose accuracy is acceptable for the desired purpose.

This research presents aspects related to the synchronization of a power inverter to operate in on-grid mode and its efficient performance. In this way, algorithms are proposed to carry out the correlation and adjustment function minimized by a decreasing gradient to modify the identification of the signal and parameters of the grid before synchronizing. The way of generating the sinusoid signal, whose amplitude, frequency, and phase are controlled, is based on a chirp generator. The novelty of the proposed control is based on a structure capable of creating a numerically stable condition that achieves a gradual phase adjustment of the sync chirp generator and produces an equivalent in amplitude, frequency, and phase with the addition of phase adjustment [23]. The effect is like cloning the synchronized signal and adding the missing component to achieve the phase adjustment that allows power flow to the electrical grid.

The aforementioned nonlinear conditions cannot be faced with classical control tools. The use of Mamdani-type fuzzy controllers has been implemented due to the increased degree of freedom that implies the operation of this kind of controller. Based on this fact, another significant contribution of this paper is to present approximate models that allow an initial tuning of neuro-fuzzy controllers connected in cascade, which are subsequently tuned until the desired performance is achieved.

2. Materials and Methods

2.1. Nomenclature

MOV Metal oxide varistor

PLL Phase-locked loop

THD Total harmonic distortion (–)

V_{RMS} Root mean square grid voltage (V)

$V_{1_{RMS}}$ Root mean square voltage of the first harmonic of the grid voltage (V)

$V_{n_{RMS}}$ Root mean square voltage of the nth harmonic of the grid voltage (V)

S Apparent power (VA)

Z Impedance (Ω)

η Efficiency (–)

S_1 Apparent power for the fundamental harmonic (VA)

S_{overall} Total apparent power (VA)

ρ Efficiency complement, $1-\eta$ (–)

λ Sinusoidal fundamental harmonic amplitude condition (V)

θ Cosine fundamental harmonic amplitude condition (V)

N Number of log samples for correlational processing

T_s Log sampling time (–)

ω_i Frequency in (rad/s) in correspondence with the theoretical 60 Hz

y_i Line voltage recording (V)

i Indexer

β_i Amplitude correlated initial condition (V)

ψ_i Correlated phase initial condition (rad)

J Cost function

ω_f Identified final frequency (rad/s)

β_f Identified amplitude correlated end condition (V)

ψ_f Identified end condition of correlated phase (rad)

P_s Active power supplied by the electronic system (W)

Q_s Reactive power supplied by the electronic system (VAR)

P_R Active power received by the reference electrical bar (W)

Q_R Reactive power received by the reference electrical bar (VAR)

X_L Inductive reactance of the simulated line (Ω)

V_S Voltage provided by the electronic system (V)

V_R Reference bar voltage (V)

δ Phase condition between the bus and the electronic system (rad)

Q_{av} Average reactive power on the simulated line (VAR)

R Simulated line resistor (Ω)

P_{line} Active power on the simulated line (W)

E_i Error between an i-th prediction and its i-th sample

α Participation factor for error (cost function) (–)

β Participation factor for derivative error (cost function) (–)

μ Degree of truth of a membership function (–)

γ Degree of truth of a membership function (–)

μ_i Degree of truth of an i-th membership function (–)

x Variable of the fuzzy universe

x_i Abscissa value of the vertex of the i-th membership function

x_{i-1} Abscissa value of the extreme left of the i-th membership function

x_{i+1} Abscissa value of the right end of the i-th membership function

Δ Width of the base of the membership function

V_i Voltage output of the transformer (V)

V_{0_i} Transformer voltage output in the first harmonic (V)

L Inductance of the simulated line (H)

V_{L_i} i-th voltage of the inductance in the simulated line inductance (V)

I_{L_i} i-th current of the inductance in the simulated line inductance (A)

f Frequency of the i-th voltage and current of the simulated line inductance (Hz)

$\widehat{P}_i$ i-th power prediction (p.u.)

P_i i-th power (p.u.)

ARX Exogenous regression analysis

K Gain of the linear model of the phase generator

φ_g Phase generator output (rad)

sp_φ Phase setpoint (rad)

PI Integral proportional control

P Proportional control

SP_p Power setpoint (p.u.)

$\widehat{P}_{l_i}$ i-th linear power prediction (p.u.)

P_{nl_i} i-th nonlinear power prediction (p.u.)

T_1 Time constant 1 (s)

T_2 Time constant 2 (s)

T_3 Time constant 3 (s)

T Time constant (s)

K_v Speed error constant

I_{MOV} MOV current (A)

$\widehat{I}_{MOV}$ MOV current prediction (A)

P_{MOV} MOV power (W)

V_{MOV} MOV voltage (V)

V_{ref} MOV threshold voltage (V)

q MOV characterization exponent (–)

2.2. Grid Modeling. In this section, methodological aspects are covered to determine the quality of the grid operation. Statistical knowledge of the electrical supply signal behavior allows drawing strategies for synchronizing the inverter power electronics system. Taking into account the aim proposed in this paper, the first step is to study the grid's aspects and characterize them using statistical identification techniques such as the correlation for sinusoidal systems. The objective is to achieve a minimum error in the global relative percentage deviation and a high value in the Pearson quadratic correlation factor using a minimum number of samples per period.

This section can be subdivided into the following subsections: First, statistics for evaluating and identifying the grid to replicate conditions for synchronization. Second, the grid model and its Thevenin simplification is developed in a three-bar electrical diagram for the study of static power flow. Thirdly, we perform the dynamic power flow study of the simplified electrical system using the obtained model.

2.2.1. Distribution Grid: Electrical Signal Sample Recording and Processing. The study's first phase consists of taking a record of the electrical signal from the distribution grid. This exploratory phase is sampled at 25 (kHz) for 1.27996 (s). The recording was made using an ACUTE DS-1202 digital oscilloscope, high-quality PC-based 2-channel DSO, with 200 (MHz) bandwidth, 200 (MSample/s) sampling rate, and 512 (Kbyte) memory.

A sinusoidal quality assessment of the grid's electrical energy is carried out considering the harmonic distortion factor, or THD, for which the square root of the equation is used.

$$\begin{aligned}\mathrm{THD}^2 &= \frac{V_{\mathrm{RMS}}^2 - V_{1_{\mathrm{RMS}}}^2}{V_{1_{\mathrm{RMS}}}^2} \\ &= \frac{\sum_{n=2}^{\infty} V_{n_{\mathrm{RMS}}}^2}{V_{1_{\mathrm{RMS}}}^2}.\end{aligned} \tag{1}$$

The impact of the value of the harmonic distortion factor is considered when an efficiency factor is established based on the active power used when the fundamental frequency is considered. For this purpose, the following equations are used based on the analysis proposed in Figure 1:

$$\begin{aligned}S &= \frac{V_{\mathrm{RMS}}^2}{|Z|} \\ &= \frac{V_{1_{\mathrm{RMS}}}^2}{|Z|} + \frac{\sum_{n=2}^{\infty} V_{n_{\mathrm{RMS}}}^2}{|Z|},\end{aligned} \tag{2}$$

$$\eta = \frac{S_1}{S_{\mathrm{TOTAL}}} = \frac{V_{1_{\mathrm{RMS}}}^2/|Z|}{V_{1_{\mathrm{RMS}}}^2/|Z| + \sum_{n=2}^{\infty} V_{n_{\mathrm{RMS}}}^2/|Z|} = \frac{V_{1_{\mathrm{RMS}}}^2}{V_{1_{\mathrm{RMS}}}^2 + \sum_{n=2}^{\infty} V_{n_{\mathrm{RMS}}}^2}, \tag{3}$$

$$\eta = \frac{V_{1_{\mathrm{RMS}}}^2}{V_{1_{\mathrm{RMS}}}^2 + V_{1_{\mathrm{RMS}}}^2 \mathrm{THD}^2} = \frac{1}{1 + \mathrm{THD}^2}. \tag{4}$$

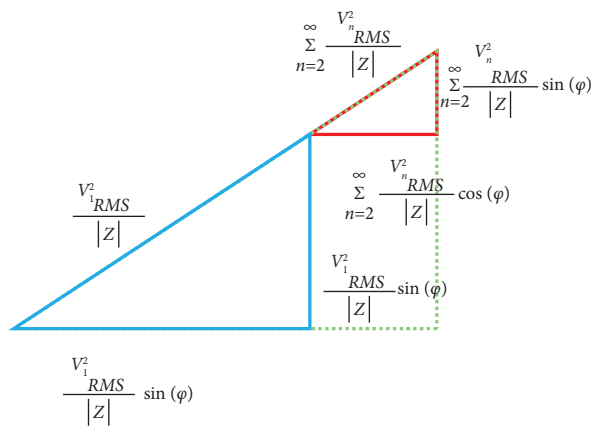

FIGURE 1: Power triangle considering the harmonic effect.

Figure 1 shows the power triangle made up of both the fundamental and harmonic components. The harmonic content, being of high frequency, is not broadly useable, because energy is lost in heat, both in static and dynamic machines.

The same result is obtained when determining the energy efficiency due to the harmonic effect based on equation (3), if active or reactive power is considered instead of using apparent power.

The importance of equation (5) is clear to establish the quality of the sinusoid, where its tendency to zero gives information about purity in the generation process. On the other hand, its tendency to unity, typical of synthesized alternating signals such as square waves, is generally not acceptable for all electrical devices. However, from the energy point of view, the efficiency measured from equation (4) is an alternative way to determine the quality of the signal injected into the main grid. The following equation represents a way of presenting the energy losses due to the signal's harmonic content:

$$\rho = \frac{\mathrm{THD}^2}{1 + \mathrm{THD}^2}. \tag{5}$$

The algorithm proposed in this paper is based on a double correlation, the first being an algorithm that offers a closed mathematical adjustment expression to determine the amplitude and phase, assuming that the frequency is 60 (Hz). The second correlation is an improvement that uses the result of the first correlation as a starting point and whose result is the product of an iterative search process using the decreasing gradient method.

The following equation allows for determining amplitude conditions, which are determined with the help of equation (7) based on the amplitude and phase of the sinusoid of the grid-sampled voltage.

$$\begin{bmatrix} \lambda \\ \theta \end{bmatrix} = \begin{bmatrix} \dfrac{\sin(2NT_s\omega - T_s\omega)}{4\sin(T_s\omega)} + \dfrac{(2N+1)}{4}\dfrac{\cot(T_s\omega)}{4} - \dfrac{\cos(2NT_s\omega - T_s\omega)}{4\sin(T_s\omega)} \\ \dfrac{\cot(T_s\omega)}{4} - \dfrac{\cos(2NT_s\omega - T_s\omega)}{4\sin(T_s\omega)}\dfrac{(2N-1)}{4} - \dfrac{\sin(2NT_s\omega - T_s\omega)}{4\sin(T_s\omega)} \end{bmatrix}^{-1} \cdot \begin{bmatrix} \sum_{i=0}^{N-1} y_i \cdot \cos(T_s i\omega) \\ \sum_{i=0}^{N-1} y_i \cdot \sin(T_s i\omega) \end{bmatrix}, \tag{6}$$

$$\beta = \sqrt{\lambda^2 + \theta^2} \wedge \psi = \arctan\left(\frac{\lambda}{\theta}\right). \tag{7}$$

Besides, the following equation is the cost function that, when minimized with the decreasing gradient method, allows obtaining a much more accurate value of the amplitude, phase, and frequency of the sampled electrical signal of the system.

$$J = \frac{1}{2}\sum_{i=0}^{N-1} \left(\beta \sin(\omega i T_s + \psi) - y_i\right)^2. \tag{8}$$

However, equation (9) is used to establish a relative parameter in the evaluation process for the identification of rest of the parameters. Therefore, equation (9) can be related with equation (10), which is the multivariable correlation factor of Pearson presented in the process of identification of systems.

$$\varepsilon = 100 \times \sqrt{\frac{\sum_{i=0}^{N-1} \left(\beta \sin(\omega i T_s + \psi) - y_i\right)^2}{\sum_{i=0}^{N-1} y_i^2}}, \tag{9}$$

$$R_y^2 = 1 - \frac{\sum_{i=0}^{N-1} \left(\beta \sin(\omega i T_s + \psi) - y_i\right)^2}{\sum_{i=0}^{N-1} \left(y_i - \overline{y}_i\right)^2}. \tag{10}$$

It is worth mentioning that equations (8)–(10) are presented based on i-index samples because they are part of a sampling process defined based on N samples that can correspond to one or more periods, even a fraction thereof. This study proposes sampling with a buffer of two and a half periods to consider a 60 (Hz) signal. Nevertheless, the registered and parameterized signal does not have to have this value since the reality of the generation process presents a variation in the frequency that is usually below 1%, which could be much more under fault conditions.

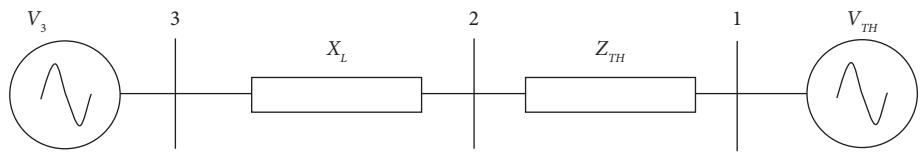

Figure 2: Simplified 3-bar model based on the Thevenin equivalent circuit of the electrical grid seen by the inverter system.

2.2.2. Generated Power and Load Flow in the Coupling Line to the Grid Bar. The power generated and supplied to the grid depends on the power angle δ. The power angle allows establishing the active power generated, supplied, and received by the grid bar, determined by following equations, as well as reactive powers, also defined by the following equations [1]:

$$P_s = \frac{1}{X}\left(|V_S||V_R|\sin\delta\right)[W], \tag{11}$$

$$Q_s = \frac{1}{X}\left(|V_S|^2 - |V_S||V_R|\cos\delta\right)[\text{VAR}], \tag{12}$$

$$P_R = \frac{1}{X}\left(|V_S||V_R|\sin\delta\right)[W], \tag{13}$$

$$Q_R = \frac{1}{X}\left(|V_S||V_R|\cos\delta - |V_S|^2\right)[\text{VAR}]. \tag{14}$$

From equations (11) and (13), it is concluded that the maximum active power supplied by the generator (when the generator voltage is equal to the network bus voltage) is 90 degrees. Under this condition, the reactive power is equal in magnitude to the active power; therefore, the generator's maximum power is approximately 142 (kVA).

The reactive power in the grid for a relatively small electrical grid with negligible resistance is of interest, as shown in equation (15). In the case of considering the resistance of the coupling grid, the active power can be determined using the equation (16) [1].

From equation (15), the value of the reactive power in the line is negligible. However, it is necessary to consider deviations in the voltage regulation, which is why it cannot be wrongly dimensioned and must be considered the worst of cases to avoid failure of this device.

$$Q_{av} = \frac{1}{2X_L}\left(|V_S|^2 - |V_R|^2\right)[\text{VAR}], \tag{15}$$

$$P_{\text{line}} = \frac{\left(P_S^2 - Q_S^2\right)R}{|V_S|^2}[W]. \tag{16}$$

The reactive power in the grid is essential when designing the coupling reactor that emulates the short transmission line. From equation (15), it can be concluded that the value of the reactive power in the line is negligible. However, it is necessary to consider its deviations in the voltage regulation, the reason why it cannot be wrongly dimensioned, and, in the worst case, should be considered to avoid breakdowns on this device.

Table 1: Parameter for the per unit model of the grid.

Base parameters	Impedance and reactance of the model
$\text{VAR}_{\text{base}} = 1.11$ (MVA)	$RL_i = 1.875e-6$
$V_{\text{base}} = 13.8$ (kV)	$XL_i = 9.26e-7$
$I_{\text{base}} = \text{VAR}_{\text{base}}/V_{\text{base}}$	$XC_i = -5995397.84$
$Z_{\text{base}} = V_{\text{base}}/I_{\text{base}}$	$Z_i = 2278 + 1104.25i$

Additionally, implementing a transient suppressor of the MOV or Crowbar type in parallel with the reactor should be considered to suppress transients in case of differential voltage.

Although the active power is negligible before minimum values of R, this must be considered at the moment of the design of the reactor and at the moment of quantifying the active power that will not be delivered to the reference bar, as shown in equation (16).

From the previous equations, it can be concluded that the power angle determines the contribution of active power to the bus. However, reactive power is generated by keeping the power angle at zero and only by varying the voltage.

2.2.3. Static Power Flow Modeling. Considering as a case study a small town with an electrical demand of approximately 3 (MW) of active power and around 8,000 subscribers to the electrical service. An empirical model of three bars has been considered to study the static and dynamic power flow from the inverter system to the main grid.

As shown in Figure 2, the three-bar model contemplates the generator bar, whose voltage at bar 1 corresponds to the Thevenin voltage of the model, and the voltage at bar 2 corresponds to the voltage at the substation or coupling transformer of the inverter system. Finally, bar 3 corresponds to the voltage generated by the inverter system.

The Thevenin model of the system was obtained under the following considerations:

(i) The regulations for the national interconnected system of Ecuador consider a system efficiency of around 95%, with an approximate power factor of 0.9.

(ii) Considering a distribution voltage of 13.8 (kV), there is an apparent power of 3.33 (MVA) in the system, with 72.64 (kVAR) corresponding to reactive losses in the line. From this value, 1.48 (kVAR) corresponds to the capacitive effects of the line and 74.13 (kVAR) to inductive effects, with 150 (kW) losses arising due to the Joule effect.

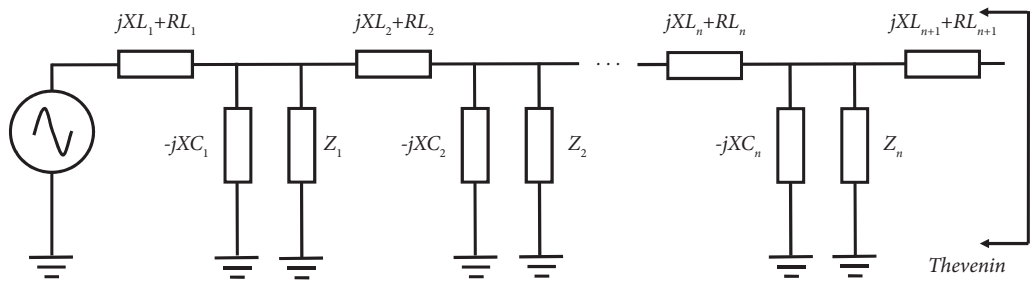

Figure 3: Thevenin model for the grid seen by the inverter system.

Table 2: Parameter for the Thevenin model of the grid.

Thevenin parameters
$Z_{TH} = 0.01474 + 0.00728i$
$V_{TH} = 0.9741$
$X_L = 11.11$

Considering 8,000 subscribers to the electrical service, the distribution of electrical impedances and reactances for the model is obtained, in per unit, as detailed in Table 1.

Figure 3 shows how the loads connected to the network are distributed and the consideration of the line impedances by sections, where the line and load impedances keep the same value. In this model, 8,000 sections have been considered to correspond to the total subscribers of the case study.

Under the defined considerations, the Thevenin model has been calculated, in per unit, seen from the coupling bar 2 of the inverter system with the corresponding values described in Table 2.

As shown in Figure 4(a), taking into account the phase difference between bus bars 2 and 3, it is possible to obtain the active and reactive powers, in per unit, as depicted in Figures 4(b) and 4(c), respectively.

To determine the phase condition in buses 2 and 3, as well as the generator voltage, the following considerations have been defined:

$$V_3 = V_2, \qquad \varphi_3 = \delta + \varphi_2, \tag{17}$$

$$P = \frac{V_2^2 \sin(\delta)}{X_L}, \tag{18}$$

$$V_2\angle\varphi_2 = \left(\frac{V_2\angle(\delta+\varphi_2) - V_1\angle 0}{X_L + Z_{TH}}\right) Z_{TH} + V_1\angle 0. \tag{19}$$

Solving the system, using equations (18) and (19), to determine V_2 and φ_2, the values for V_3 and φ_3 are obtained. Under the evaluated conditions, Figure 5(a) shows the evolution of the voltage of the inverter system in bus 3. To achieve the phase difference between bus 3 and 2, such that the desired active power flow is fulfilled, the phases of bars 2 and 3 are evaluated concerning bar 1, as shown in Figures 5(b) and 5(c), respectively.

2.2.4. Dynamic Power Flow Modeling. Using the simplified model of the three busbars electrical system (Figure 2), a representation in the state space has been defined considering a state to reproduce the response of the grid to the power supply by the inverter system. Due to their electronic nature, time considerations for power supply (which are typical of inversion systems) allow times between 2 and 5 seconds [11, 24]. Although the time for the supply of power is very short, this is typical of distributed networks and is present in generation systems of an electronic nature.

The state space that allows obtaining the dynamic behavior of the voltage in bus 2, as well as the current that flows through the line that connects buses 3 and 2, as shown in the following equation:

$$[\dot{x}] = \begin{bmatrix} \frac{-R_{TH}}{L_{TH}+L} \end{bmatrix} [x] + \begin{bmatrix} \frac{1}{L_{TH}+L} & \frac{-1}{L_{TH}+L} \end{bmatrix} \begin{bmatrix} V_3 \\ V_1 \end{bmatrix},$$

$$\begin{bmatrix} V_L \\ I_L \\ V_2 \end{bmatrix} = \begin{bmatrix} \frac{-R_{TH}L}{L_{TH}+L} \\ 1 \\ \frac{-R_{TH}L_{TH}}{L_{TH}+L} \end{bmatrix} [x] + \begin{bmatrix} \frac{L}{L_{TH}+L} & \frac{-L}{L_{TH}+L} \\ 0 & 0 \\ \frac{L_{TH}}{L_{TH}+L} & 1 - \frac{L_{TH}}{L_{TH}+L} \end{bmatrix} \begin{bmatrix} V_3 \\ V_1 \end{bmatrix}. \tag{20}$$

Figure 6 shows the dynamic behavior of the power in the transmission line, represented in p.u., which corresponds to the power generated by the inverter system. The model's dynamic order is increased in estimating the active power of the line, for which the weighted integral of the instantaneous power is approximated based on the state.

$$[\dot{x}] = [-6][x] + [6][V_3 \cdot I_L], \qquad [P_{\text{line}}] = [1][x] + [0][V_3 \cdot I_L]. \tag{21}$$

As depicted in Figure 6, creating a positive phase shift (or in advance) produces an increase in power in the grid. This increase in power produces an increase in the voltage of the system. Although the model presented cannot reproduce the phenomenon associated with the increase in frequency, that is another variable is dynamically affected by the injection of power from the electrical grid. This is why power flow dynamics are studied to anticipate and compensate for grid oscillations that cause undesirable frequency oscillations.

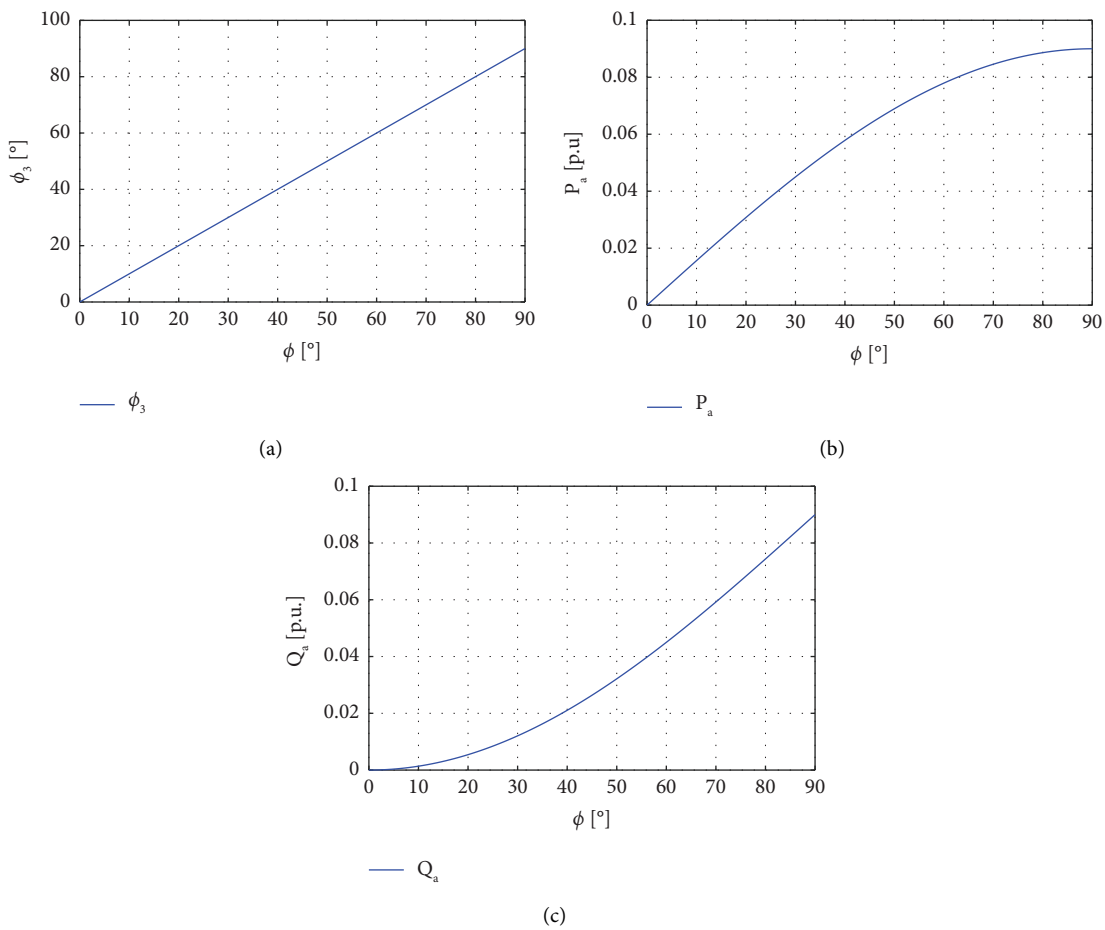

Figure 4: Electrical behavior between bars 2 and 3: (a) phase, (b) active power flow, and (c) reactive power flow.

2.2.5. Comparison of the Dynamic Power Flow between the Proposed Model and the Measurement with PMUs. This section summarizes power flux transmission measurements using ABB's RES670 phasor measurement unit (PMU). Measurements were made on the line made up of the coupling inductor between the inversion system and the substation. For the comparison, the same generation set points used during the simulation were considered. The results obtained are shown in Figure 7.

The results show that the experimental measurements converge to the same simulated values for reasons of adjusting the power set point of the inversion system. However, the dynamics is affected by the randomness of the connected loads and the consideration of a higher dynamic order reality, or simply of distributed parameters present in the network.

It is important to highlight that the principles of scalarity, typical of linear systems, are no longer fulfilled since the load-taking times are slightly increased as the power set point increases. It is important to highlight that during the experimentation, the AGC (automatic generation control) of the system was not inhibited, which is why the thermogenerators and hydrogenerators played an uncontrolled role in the secondary regulation, which affected the dynamics to be studied.

However, the results show the ability to guarantee fast load taps for low power set points, and the response being slightly slower for when the power set point tends to 100% of the power capable of supplying the inversion system.

2.3. Control Systems for ON-GRID Operation. In this section, control strategies based on neuro-fuzzy techniques are outlined for the implementation of cascade controllers that allow the regulation of the power supplied by the inverter system, as well as a gradual adjustment in the phase condition that allows the flow of desired power to guarantee the supply of power to the network. Although the study was designed for a 100 (kW) system, the modeling, and proposed control can be applied to a system of greater or lesser power, as can the interpretation of the results (presented in p.u.).

2.3.1. Mamdani-Type Fuzzy Inference System Processing. The Mamdani-type fuzzy inference system has been implemented to characterize both the angular speed for the offset contribution in the inverter, once the generation unit is synchronized, as well as to adapt proportional and integral values of the closed-loop control of the active power that allows setting the offset setpoint value.

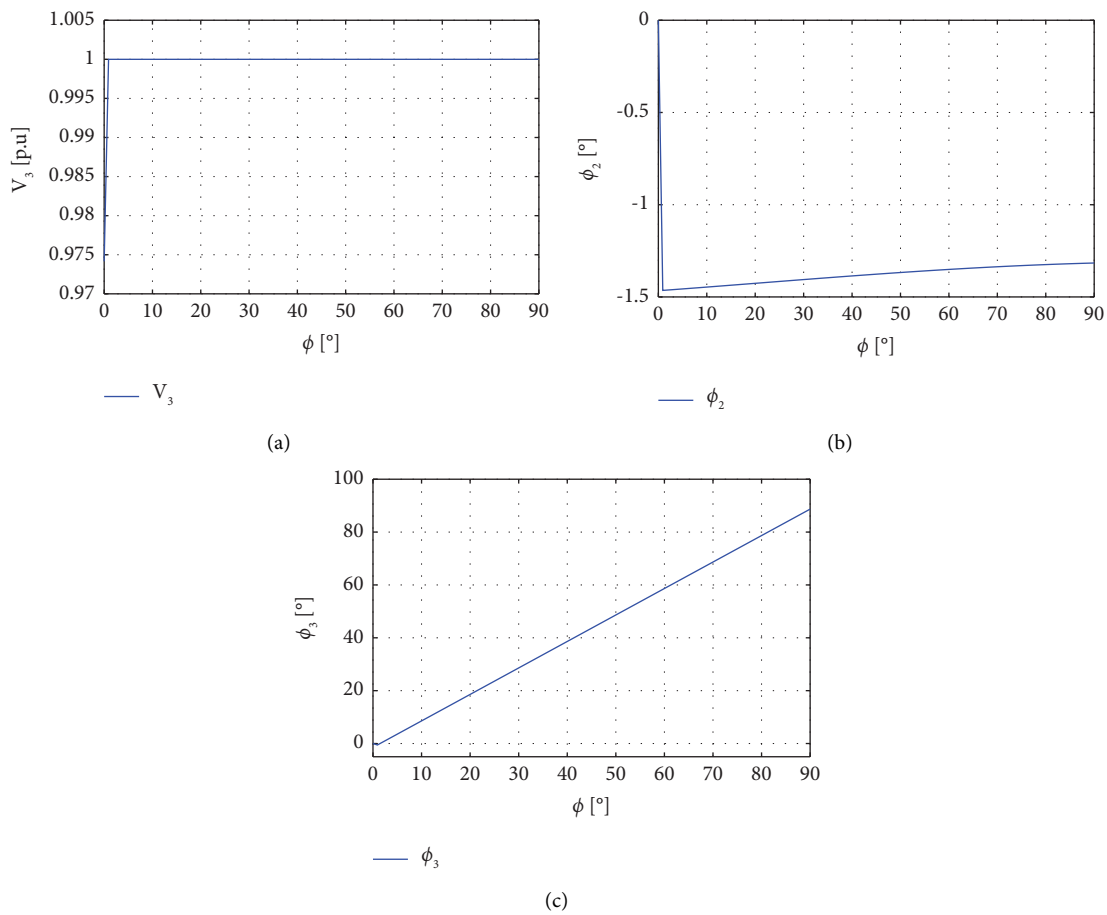

Figure 5: Electrical behavior between bars 1, 2, and 3: (a) voltage in bar 3 provided by the inverter system, (b) phase of bar 2 with respect to bar 1, and (c) phase of bar 3 with respect to bar 1.

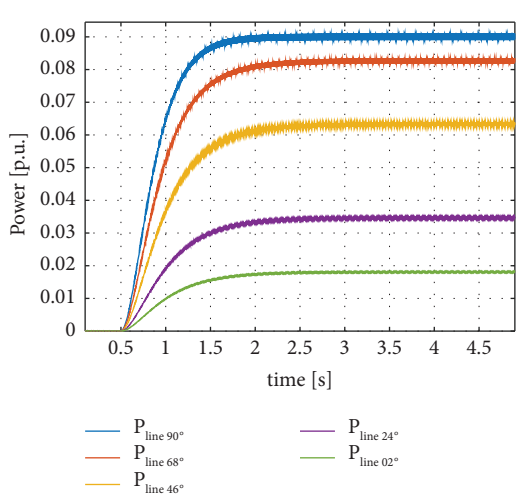

Figure 6: Active power on the simulated transmission line.

For this particular case, inferences are presented with two universes of discussion, whose implication is achieved using a producer of the degrees of truth of the membership functions. If the conjunction of these degrees of truth is needed, it is carried out by implementing the probabilistic OR. The consequent is achieved through the aggregation of the rules implementing a sum, while the defuzzification or single-valued value is achieved through the centroid method.

To facilitate the calculation of the rules, the range of the universe of discussion is obtained under the expert knowledge of the behavior of the signals, taking into consideration the possible extreme values that can be reached under the dynamics of the regulation, being the membership functions assigned using a regular partition following the rule of overlap.

The membership functions of the rules in the consequent are adjusted using an optimization method based on the decreasing gradient. This optimization defines a cost function that values the behavior of the fuzzy dynamic system, considering the control deviation and its variation. Equation (22) shows the cost function, whose minimization guarantees the achievement of the setpoint under the condition of minimum stress of the system or actuators.

$$J = \sum_{i=0}^{N-1} \left(\alpha E_i^2 + \beta \left(\frac{d}{dt} E_i \right)^2 \right). \tag{22}$$

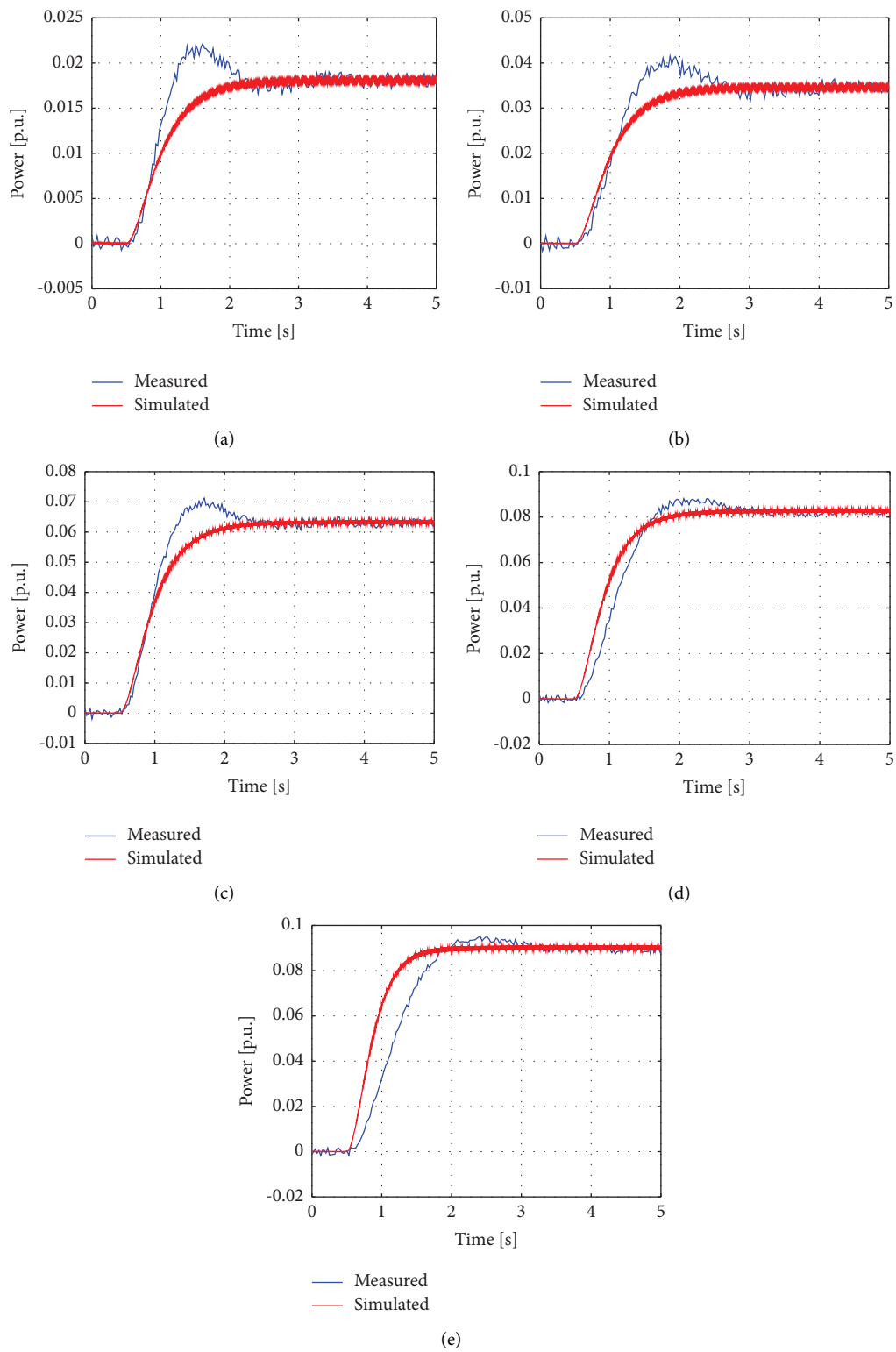

Figure 7: Response in per unit of the power flow dynamics (simulated and measured) when the generation set point corresponds to: (a) 20%, (b) 38%, (c) 70%, (d) 91%, and (e) 99%.

2.3.2. Considerations for PI and PControllers of the Mamdani Fuzzy Type. The degrees of freedom a fuzzy controller offers are directly related to the number of rules. The redundancy of degrees of freedom allows adjustments that guarantee a higher performance than a classic controller. However, there is a compromise between the number of rules and the complexity of reaching a global minimum on a cost function surface.

For all the universes of discussion, the membership functions must be the simplest to calculate; therefore, delta or triangular type functions are used.

$$\mu_i = \max\left(\min\left(\frac{(x - x_{i-1})}{(x_i - x_{i-1})}, 1\right), 0\right) - \max\left(\min\left(\frac{(x - x_i)}{(x_{i+1} - x_i)}, 1\right), 0\right). \tag{23}$$

The fuzzy AND has been implemented with the product, and the fuzzy OR has been implemented with the probabilistic OR, as shown in equations (24) and (25), respectively.

$$\mu \& \beta = \mu \times \beta, \tag{24}$$

$$\mu | \beta = \mu + \beta - \mu \times \beta. \tag{25}$$

In fuzzy inference aggregation, an OR has been implemented by addition, as shown in the following equation:

$$\mu | \beta = \mu + \beta. \tag{26}$$

Implementing the sum as OR in the aggregation of rules allows obtaining a unique value in the defuzzification by implementing a centroid weighting of the membership functions of the activated rules.

$$y = \frac{\sum_{i=1}^{n} (\Delta \cdot \mu_i/2) x_i}{\sum_{i=1}^{n} (\Delta \cdot \mu_i/2)}. \tag{27}$$

In equation (27), Δ is the width of the membership function of the rule, i is the i-th activated rule or its degree of truth, and is the value, in the universe of discussion, where the vertex of the triangular or delta membership function is located and which represents its centroid.

In a simplified consideration, each i-th membership function associated with the output presents an i-th area that depends on the degree of truth of the consequent, which in this case, being triangular functions, is considered to have the same bases. The consideration of equal bases in the property functions of the outputs allows us to establish the relationship between the Mamdani inference and that of Takagi Sugeno Kang of order zero. Note the following simplification:

$$\begin{aligned} y &= \frac{\Delta/2 \cdot \sum_{i=1}^{n} \mu_i \cdot x_i}{\Delta/2 \cdot \sum_{i=1}^{n} \mu_i} \\ &= \frac{\sum_{i=1}^{n} \mu_i \cdot x_i}{\sum_{i=1}^{n} \mu_i}, \end{aligned} \tag{28}$$

$$y = \frac{\sum_{i=1}^{n} \mu_i \cdot C_i}{\sum_{i=1}^{n} \mu_i}. \tag{29}$$

In equation (28), x_i corresponds to the i-th singleton C_i, evidencing the equivalence between Mamdani fuzzy inference and Sugeno or TSK0, as seen in equation (29).

Considering equations (27)–(29), it is concluded that Sugeno's method is computationally more efficient and, indeed, a better option to train function characterization systems. However, it is well known that Sugeno's inference method modifies the general Mamdani fuzzy inference method. Additionally, the efficiency of Sugeno's method is increased when the overlap method is used and programmed so that only the activated rules are evaluated. Under these considerations, there is a maximum of 2^n as the total number of activated rules, where n is the number of variables or inputs of the fuzzy inference system.

Therefore, Sugeno's method is conceptually better for the implementation of instantaneous systems in characterization processes, and therefore, it is also better for the implementation of dynamic systems. However, the reason for the implementation of this study using Mamdani is because it is better known than Takagi Sugeno Kang of zero order (or higher) and additionally because its performance, assessed with Matlab, is slightly more efficient in terms of time, with an estimate in the time relation of Tmamdani/Tsugeno equal to a mean of 0.9802.

The adjustments to the fuzzy systems are made in two stages. The first stage corresponds to the phase allocator, in which the membership functions of the consequent are adjusted (their position in the universe of discourse) based on a cost function that penalizes the error and the correction speed, as seen in Figure 8.

The second stage corresponds to the fuzzy PI control that guarantees compliance with the power setpoint and establishes the setpoint for the phase angle. The adjustment is made under the same considerations as the previous stage. The modeling of the active power measurement instrumentation is considered of the first order and closing the loop directly from the phase parameter, as shown in Figure 9.

2.3.3. Variable Frequency Sinusoidal Signal Generator. The variable-frequency sinusoidal generator implements the Chirp function based on a sine function of variable frequency and phase. The variable frequency implementation allows for the generated signal's adaptation to the frequency of the main electrical grid. The variable phase allows gradual adjustment until reaching the desired phase shift to achieve the power angle that allows supplying the desired active power.

3. Results and Discussion

The process of synchronization and generation of a 140 (kVA) inverter to an electrical grid using Mamdani controllers in cascade are analyzed in this section under the following criteria:

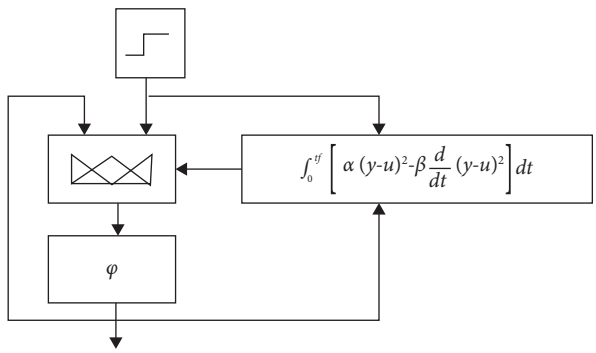

Figure 8: Phase allocator regulated by a Mamdani-type fuzzy proportional controller.

(a) Periodic processing of the reference bar voltage signal: this study guarantees the synchronization of the inversion system to the grid efficiently and at the lowest computational cost, using the correlational technique presented in the methodology section. In addition, the harmonic content's effect and its implication in unused active power are also shown.

(b) Considerations for synchronization: this section explains how the coupling transformer of the inverter system contributes to the filtering of the voltage signal and how this produces an offset in delay that must be compensated when synchronizing the electronic generation unit by the inverter.

(c) Charging or power outlet: This section presents how to determine the experimental value of the specified inductance for one of the 10 (kW) inverters. Besides, this section shows the way to establish the power correlation, based on a fuzzy estimator, to be able to establish the deviation in the process of the generation that shows a failure.

(d) Protection for the line inductor: in this section, the model for the MOV is presented as an element for suppressing voltage peaks, and the arrangement in the electrical topology of the transformer to reach the electronic inverter system is protected at all times.

(e) Contribution of power droop for system frequency compensation: This section shows how the control diagram is structured such that the electronic generation system, by inversion, can contribute to the recovery of the frequency of the electrical system or interconnected grid. These conditions are studied when disturbances occur either due to load or generation rejections or due to regulation effects during peak hours, satisfying the concept of power stagnation and the proposed American standard of 4% frequency variation capable of producing 100% of generation power variation.

(f) Electronic inversion system coupled with a transformer with 10 windings: This section integrates the idea of generating electronic inversion units (precisely 10 units), which coupled with a transformer with 10 primaries allows conceiving the 140 (kVA) system, managed under the criteria of a central, which allows the increase of the reliability.

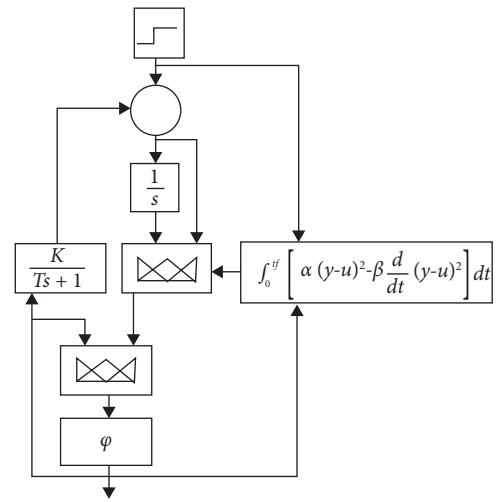

Figure 9: Active power allocator regulated by a Mamdani-type fuzzy integral proportional controller.

3.1. Periodic Processing of the Reference Bus Voltage Signal. Figure 10 shows 30 periods of the reference bar stress calculated with equations (6) and (7) and adjusted with equation (8), allowing the correlated signal that is shown in Figure 11. Besides, in Figure 10, the harmonic content present in the reference bus voltage is observed.

Based on equation (4), the percentage efficiency of the reference voltage, determined by taking into account the harmonic distortion, is 99.87%. Therefore, the previous percentage efficiency value is a good value, considered absolute.

Taking into account, as an example, the Ecuadorian electrical system, which for the year 2020 registered 8,712.29 (MW) of nominal power and 8,095.25 (MW) of effective power [2], with annual energy generated between 20,095.49 (GWh) [3] and 25,024.20 (GWh) gross or 24,805.71 (GWh) of available energy [25, 26]. Therefore, an average annual generated power between 2,294 and 2,857 (MW) is inferred, of which between 2.76 and 3.44 (MW) are lost due to the harmonic effect, as determined using equation (5).

To select the number of samples to be taken per period of the electrical signal, a study was carried out regarding a record of 416 samples per period for 30 cycles. The reference values of RMS voltage, frequency in (Hz), and phase in degrees are shown in Table 3.

Table 4 shows the execution time for 17 samples per period, yielding satisfactory results if the percentage global deviation is considered an indicator that highlights the goodness of fit concerning the samples. In this case, the Pearson quadratic correlation factor was applied.

3.2. Considerations for Synchronization. The synchronization of the inverter system must consider filtering aspects associated with the coupling transformer of the inverter so

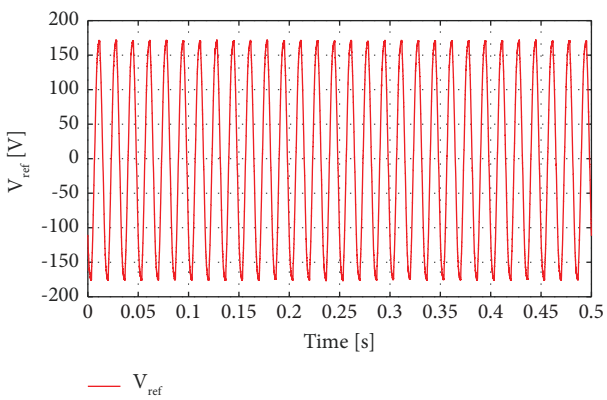

Figure 10: Sample of 30 periods of the electrical grid signal.

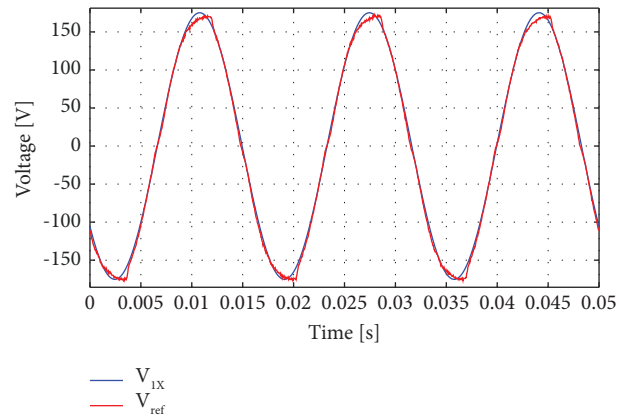

Figure 11: 50 millisecond sample of the electrical grid signal.

that harmonic distortion values are satisfied. The harmonic distortion value has been set to be below 5%, a value estimated with equation (30), being V_i transformer output voltage, and V_{o_i} is the signal of the first harmonic of this output voltage.

$$\mathrm{THD} = \sqrt{\frac{\sum_{i=1}^{N}\left(V_i - 1/N\sum_{i=1}^{N}V_i\right)^2 - \sum_{i=1}^{N}\left(V_{0_i} - 1/N\sum_{i=1}^{N}V_i\right)^2}{\sum_{i=1}^{N}\left(V_{0_i} - 1/N\sum_{i=1}^{N}V_i\right)^2}}. \tag{30}$$

Considering a triangular signal with a frequency 100 times greater than the nominal frequency of the grid (6 (kHz)) and considering a phase shift due to the filtering action of the power transformer −4.3018°, the harmonic distortion factor is around 0.027595 (2.75%). This offset, necessary to satisfy the THD condition, which is naturally introduced by the transformer, must be considered by the algorithm when compensating the offset to achieve synchronization with a zero-degree offset concerning the reference bar the microgeneration system wants to inject power.

Figure 12 shows the filtering effect of the power transformer and its inherent delay offset φ. Equations (6)–(8) applied to each of the signals allow for determining the gap between these signals. This process of determining the gap due to the filtering effect is carried out only once during the evaluation and start-up phase of the system. Later, it will be carried out as part of a predictive maintenance routine to guarantee the adjustments.

Therefore, considering that the synchronization makes periodic use of the equations (6)–(8), once the parameters have been determined, the algorithm performs offset angle compensation by filtering the effect.

3.3. Charging or Power Outlet. Once the synchronization of the inverter system and the network is given, the switch is closed. After closing, the load or power is taken. The power intake is governed by a power setpoint assigned based on a secondary control in correspondence with an algorithm that responds to the needs of the energy market. Then, based on equation (11), the phase angle adjustment for the generation of active power is carried out.

The dependence of the active power generated on the line inductance requires its experimental determination in the first instance before starting the system's operation. Line inductance is calculated by equations:

$$L = \frac{1}{2\pi f}\sqrt{\frac{\sum_{i=1}^{N}\left(V_{L_i} - 1/N\sum_{i=1}^{N}V_{L_i}\right)^2}{\sum_{i=1}^{N}\left(I_{L_i} - 1/N\sum_{i=1}^{N}I_{L_i}\right)^2}}, \tag{31}$$

$$L = \frac{1}{2}\frac{\sum_{i=1}^{N}\left(V_{L_i} + V_{L_{i-1}}\right)^2}{\sum_{i=1}^{N}\left(V_{L_i} + V_{L_{i-1}}\right)\left(\mathrm{d}I_{L_i}/\mathrm{d}t\right)}. \tag{32}$$

The use of any of the equations presents a deviation in the order of 0.03%. Therefore, the value of the calculated inductance was 3.82 (mH), for a 100 (kW) power plant with ten units of 10 (kW) each. It is important to highlight that equation (31) is worth knowing the excitation frequency of the sinusoidal signal, and equation (32) is more sensitive to noise because it presents the current derivative. However, it is essential to mention that equation (32) is much more unbiased than equation (31).

During the operation of the inverter system, it is crucial to monitor the power differential between the generated and estimated power. For this, the variables of the offset angle in the bus bar between the coupling point and the terminal voltage of the inverter are used, considering that the inverter voltage is at the same amplitude as the bus voltage. With these variables and a neuro-fuzzy power correlation system, the power is estimated and contrasted with the power measured by instrumentation in the feedback. In the event of a severe discrepancy, it is necessary to produce a shutdown or emergency stop of the inverted transistorized generating unit.

Table 3: Samples per period selection criteria.

	30 periods 416 samples per period
Samples	12500
Vrms: (V)	123.8733
f: (Hz)	60.0056
Phase: (°)	37.1615
Processing time (s)	0.1323195

Table 4: Samples per period selection criteria.

	2.5 periods 9 samples per period	2.5 periods 17 samples per period	2.5 periods 33 samples per period
Samples	22	42	82
Vrms (V)	124.2519	124.4235	124.2813
f (Hz)	60.0477	60.0259	60.0176
Phase (°)	36.8646	36.9020	36.9904
Global deviation (%)	0.8582	0.82813	0.5662
R_y^2	0.998463	0.998472	0.998474
Processing time (s)	0.0005179	0.0005569	0.0016463

Considering the bus voltage and the inverter voltage with the same amplitude, the behavior of the active power supplied to the bus is as shown in Figure 13.

Its fuzzy implementation allows the theoretical determination of power at a lower computational cost by implementing a 25-rule Mamdani algorithm. Figure 14 presents the universe of discussion of the variable ρ in a range between 0° and 90° with five membership functions.

Figure 15 shows the universe of the discussion of the variable V_s considered $V_R = V_S$ in a range of probable existence for V_S, between 100 (V) and 200 (V), with five membership functions. Figure 16 presents the universe of discussion for the prediction output P in a range between 0 (kW) and 30 (kW), with twenty-one membership functions. Figure 17 shows the surface characterization resulting from the power given by the fuzzy system.

The standard deviation of the power prediction is ±66.6084 (W), with the percentage relative mean square error being ±0.66% concerning 10 (kW) of the active power of each inverter unit. Tables 5–7 present the construction parameters of the triangular functions of the fuzzy system.

The execution of the fuzzy inference system in the power correlation characterization uses 25 rules whose simplified matrix is summarized in Table 8.

The adjustments of the membership functions of the power were made by minimizing the cost function between the estimated theoretical power and the power predicted by the neuro-fuzzy system using N points of power generated by the inversion system in the operating range, considering an approximate surplus of 30%. Equation (33) presents the minimized cost function using the decreasing gradient.

$$J = \frac{1}{2}\sum_{i=1}^{N}\left(\widehat{P}_i - P_i\right)^2. \tag{33}$$

For load taking or power generation, a nonlinear system has been implemented to adjust the offset angle between bars, which is controlled by a fuzzy system that improves the behavior of a proportional controller. This system is located downstream of a fuzzy integral proportional controller that guarantees compliance with the power setpoint.

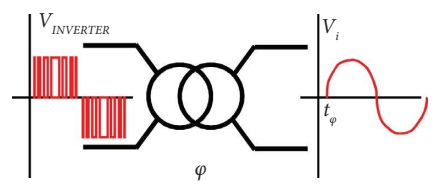

Figure 12: Offset introduced by the inverter power transformer.

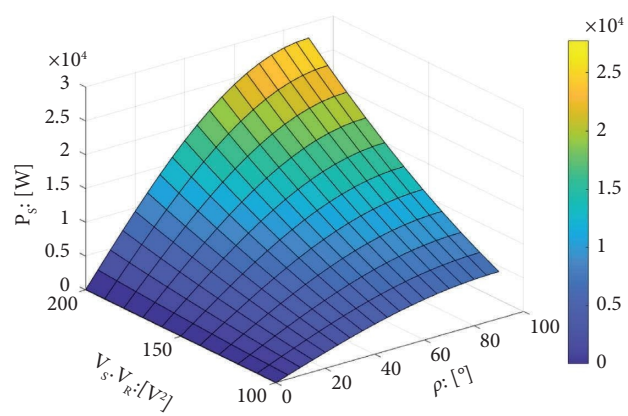

Figure 13: Behavior of the power before the variation of phase angle and equal bus-inverter voltage.

Considering that the system is of the rigid type, the controllers are tuned by taking the feedback from the phase output and incorporating a gain conversion from radians to power. This conversion is processed by a first-order dynamic that characterizes the behavior of the power measurement instrumentation. For control reasons, the open-loop system considers the power setpoint as input and the instrument's power measurement as output, where the series controller must be able to meet performance conditions under this condition.

Figure 18(a) shows a linear equivalent of the system that allows an adjustment with less commitment and, therefore, is more expeditious when training and improving the

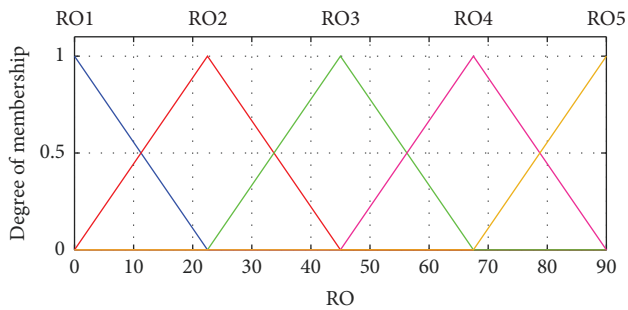

Figure 14: Membership functions of the degrees of gap.

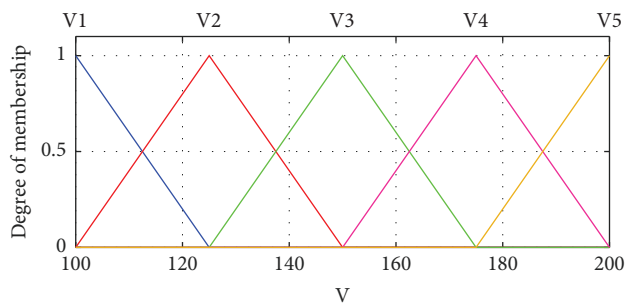

Figure 15: Membership functions the bus voltage and inverter voltage when they have the same amplitude.

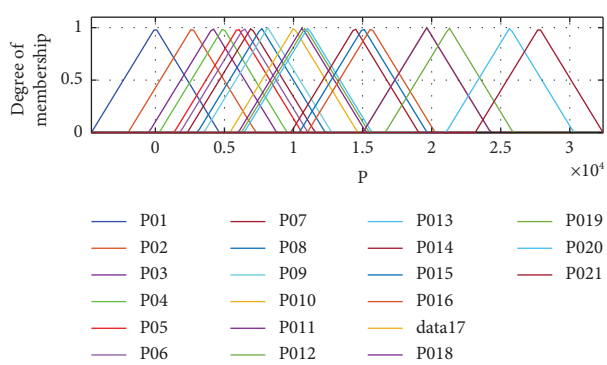

Figure 16: Membership functions as the power obtained by correlation.

location of the membership functions associated with the outputs of the controllers. Figure 18(b) proceeds to carry out the training and give the fine adjustments of the membership functions of the universe of discourse associated with the outputs of the controllers for the nonlinear behavior.

The estimate of the gain related to the integral model approximated by the phase adjustment is carried out by equation (34), obtained starting from an ARX identification of a maximum precision integral model.

$$K = \frac{1}{12T_s} \frac{\sum_{i=1}^{N} (25y_i - 48y_{i-1} + 36y_{i-2} - 16y_{i-3} + 3y_{i-4})u_i}{\sum_{i=1}^{N} u_i^2}. \tag{34}$$

Both PI and P fuzzy controllers for the nonlinear model are presented, considering their structure and the tables that allow their behavior to be reproduced. Considering basic

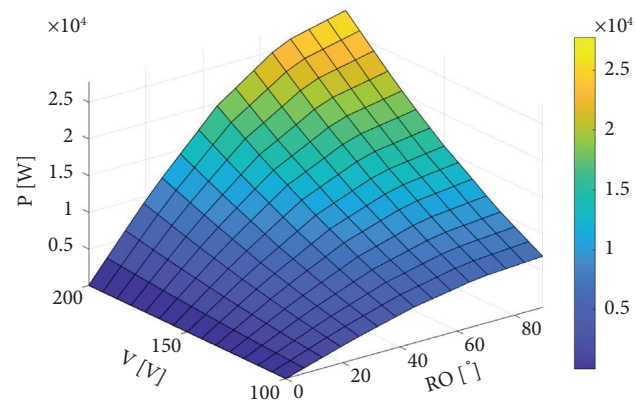

Figure 17: Fuzzy prediction of the behavior of the power in response to the variation of the phase angle and the same bus-inverter voltage.

Table 5: Triangular membership functions corresponding to the gap between the bar and the inverter.

mf	Parameters (°)		
$RO1$	−22.5	0	22.5
$RO2$	0	22.5	45
$RO3$	22.5	45	67.5
$RO4$	45	67.5	90
$RO5$	67.5	90	112.5

Table 6: Triangular membership functions corresponding to the bus voltage and the inverter.

mf	Parameters (V)		
$V1$	75	100	125
$V2$	100	125	150
$V3$	125	150	175
$V4$	150	175	200
$V5$	175	200	225

control concepts, the power deviation in (p.u), for the worst case, can only vary between ±1, with a partition given by three membership functions, as shown in Figure 19.

Regarding the universe of the discussion of the integral effect, if the maximum deviation is unity (in absolute value) and if a triangular slope of the error is considered, until reaching zero in a time of 0.16 seconds (approximate time at 10 periods of a 60 (Hz) signal) the area under the curve is around 0.08 (p.u.s). This result defines why the interval of the universe of discussion is confined to an absolute value of 0.08, with a partition given by three membership functions, as shown in Figure 20.

The phase can be between ±180°, which in radians can be limited between ±3, with a partition given by nine membership functions, as depicted in Figure 21. Tables 9–11 present the construction parameters of the triangular functions of the fuzzy system.

The execution of the fuzzy inference system in the prediction of the phase command uses 9 rules whose simplified matrix is as shown in Table 12.

Table 7: Triangular membership functions corresponding to power prediction.

mf	Parameters (V)		
$P1$	−4630	0	4629
$P2$	−1973	2657	7287
$P3$	−478	4152	8782
$P4$	280	4910	9540
$P5$	1349	5979	10609
$P6$	1786	6415	11045
$P7$	2314	6944	11574
$P8$	3042	7672	12302
$P9$	3509	8138	12768
$P10$	5395	10024	14654
$P11$	6000	10630	15259
$P12$	6221	10850	15480
$P13$	6418	11048	15678
$P14$	9805	14435	19065
$P15$	10408	15038	19667
$P16$	10995	15625	20254
$P17$	15012	19641	24271
$P18$	15018	19648	24278
$P19$	16637	21267	25896
$P20$	21033	25663	30292
$P21$	23148	27777	32407

Table 8: Rules matrix of the power correlation characterization system.

Rule	mf ρ	mf V	mf $\widehat{P}$	Weight	Operator And 1 Or 2
1	1	1	1	1	1
2	1	2	1	1	1
3	1	3	1	1	1
4	1	4	1	1	1
5	1	5	1	1	1
6	2	1	2	1	1
7	2	2	3	1	1
8	2	3	5	1	1
9	2	4	9	1	1
10	2	5	11	1	1
11	3	1	4	1	1
12	3	2	8	1	1
13	3	3	13	1	1
14	3	4	15	1	1
15	3	5	17	1	1
16	4	1	6	1	1
17	4	2	10	1	1
18	4	3	14	1	1
19	4	4	18	1	1
20	4	5	20	1	1
21	5	1	7	1	1
22	5	2	12	1	1
23	5	3	16	1	1
24	5	4	19	1	1
25	5	5	21	1	1

On the other hand, the real phase can only be present between $\pm 90^{\circ}$. This value is bounded between $\pm 1.571 \cong \pi/2$, with a partition given by three membership functions, as shown in Figures 22 and 23, respectively.

It is possible to establish the universe of the discussion of the variation of the phase-in time, considering its linear approximation based on an integral obtained discretely with the maximum precision (Figure 24). Based on the approximate model, given the high gain, if it is desired that the output of the integral system reaches $\pi/2$ in $1/60$ (s), considering a phase target of $\pi/2$ there must be a rate of change of $(\pi/2)/1000$. This value is close to 0.001571 (rad/s), whose absolute value defines the interval of the output of the fuzzy inference system of the phase controller.

Tables 13–15 present the construction parameters of the triangular functions of the fuzzy system of the phase controller.

The execution of the fuzzy inference system in the characterization of the phase variation uses 9 rules, whose simplified matrix is shown in Table 16.

Tests of linear and nonlinear models, controlled with fuzzy systems, presented similar responses. However, it is evident that, due to fuzzy controllers, both systems fail to fully comply with the scalar factor, typical of linear dynamic systems. This effect is shown in Figure 25, with tests of 30, 60, 90, and 100% of the nominal power of the inverter system.

In operation, an initial test of the complete system has been performed for a load lasting 20 cycles. This test verifies the ability of the system to synchronize and produce the gradual phase shift to satisfy the load condition. However, this is a preliminary test since, in operation, the system must meet standards such that the load intake is not perceived as a load rejection. Under this consideration, a gradient control is incorporated in the assignment of the setpoint. Figure 26 shows the complete simulation scheme for this evaluation, with a graphical result depicted in Figure 27.

Figure 27 shows the synchronization result, using simulation, of a 100% load tap, presenting the variables per unit (p.u), with the red line being the bus voltage signal and the green line showing the synchronization order. Once the algorithm has been performed, the correlation and assignment of parameters to the chirp generator must be done. The blue line is the voltage signal of the unit's inverter system, which is gradually out of phase until the power condition is satisfied, and the pink line is the power signal.

By implementing the identification of the system's behavior, a candidate model has been chosen, as shown in equation (35), initializing the variables by trial with the values $T\_1 = 1/30$, $T\_2 = 1/50$ y $T\_3 = 1/60$.

$$g(s) = \frac{1}{(T_1 s + 1)(T_2 s + 1)(T_3 s + 1)}. \tag{35}$$

By applying the decreasing gradient method to find optimal values of the time constants, it was possible to minimize the cost function given by equation (36). In this equation, $\widehat{y}_i$ is the linear prediction of the power from the model obtained with the proposed transfer function, as shown in (37), and y_i is the power of the nonlinear model with the fuzzy controller, being u_i the setpoint, which corresponds to a step by step synchronized with the closing order of the power switch.

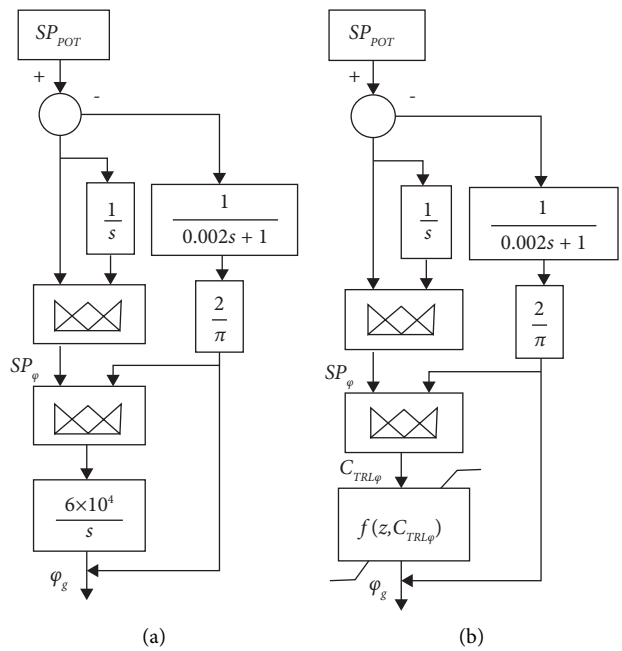

Figure 18: Fuzzy controller (a) applied to a simplified linear model for generating the shift angle for power generation, (b) applied to a nonlinear model for generating the shift angle for power generation.

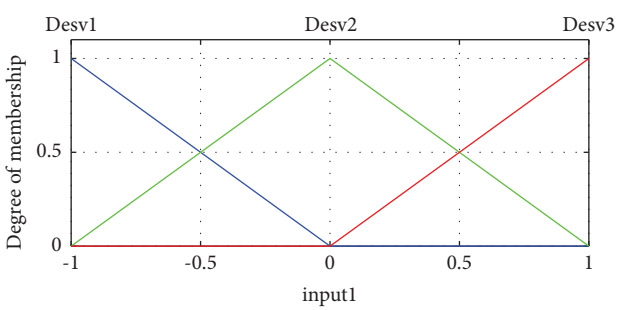

Figure 19: Membership functions of the power deviation.

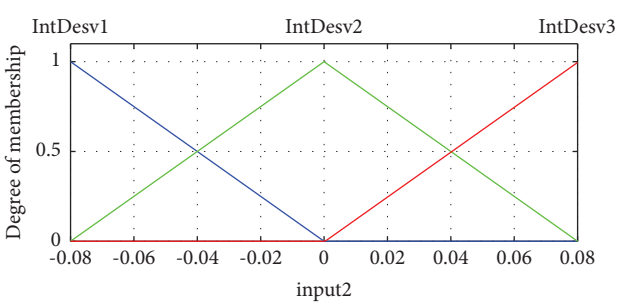

Figure 20: Membership functions of the power deviation integral.

$$J = \sum_{i=1}^{N} \left(\hat{y}_i - y_i\right)^2, \tag{36}$$

$$\hat{y}_i = \mathscr{L}^{-1}\left\{\frac{u(s)}{(T_1 s+1)(T_2 s+1)(T_3 s+1)}\right\}. \tag{37}$$

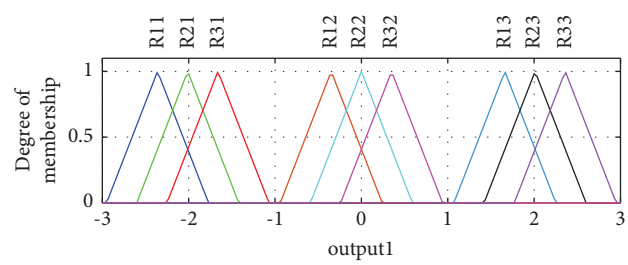

Figure 21: Membership functions of the phase setpoint prediction.

Table 9: Triangular membership functions of the universe of discourse corresponding to the power deviation.

mf	Parameters (p.u.)		
Desv1	−2	−1	0
Desv2	−1	0	1
Desv3	0	1	2

Table 10: Triangular membership functions corresponding to the integral of the power deviation.

mf	Parameters (p.u.s)		
IntDesv1	−0.16	−0.081	0
IntDesv2	−0.082	$2.602e-18$	0.083
IntDesv3	0.000338	0.080338	0.160338

The evolution in generations of the cost function is shown in Figure 28, observing the evolution of the parameters in Figure 29.

Table 11: Triangular membership functions corresponding to the prediction of the phase setpoint.

mf	Parameters (rad)		
$R11$	−2.9508	−2.3606	−1.7705
$R12$	−0.9398	−0.3496	0.2405
$R13$	1.0712	1.6614	2.2515
$R21$	−2.6012	−2.0111	−1.4209
$R22$	−0.5902	0	0.5901
$R23$	1.4208	2.011	2.6011
$R31$	−2.2516	−1.6615	−1.0713
$R32$	−0.2406	0.3495	0.9397
$R33$	1.7704	2.3605	2.9507

Table 12: Rules matrix of the phase setpoint characterization system.

Rule	mf DesPot	mf IntDesPot	mf phase	Weight	Operator And 1 Or 2
1	1	1	11	1	1
2	1	2	12	1	1
3	1	3	13	1	1
4	2	1	21	1	1
5	2	2	22	1	1
6	2	3	23	1	1
7	3	1	31	1	1
8	3	2	32	1	1
9	3	3	33	1	1

From Figure 29 a simplified function can be defined for the model as shown in (38), which can be represented, as shown in equation (39).

$$g(s) = \frac{1}{(Ts+1)^3}, \tag{38}$$

$$g(s) = \frac{1/Ts\left(T^2s^2 + 3Ts + 3\right)}{1 + 1/Ts\left(T^2s^2 + 3Ts + 3\right)}. \tag{39}$$

Therefore, for the model presented in (38), $K_v = 3T$, the value of T found by optimization is about 0.025 seconds, which allows estimating a $K_v = 13.0762$. Hence, the speed of tracking error is around 0.076 (for the estimated model), which contrasts with the nonlinear model. Furthermore, when it is excited with a unit ramp setpoint, the tracking error is around 0.0621, resulting in a $K_v = 16.0815$. Due to this, the control system does not require tracking or speed compensation, which is sufficient to control the rate of change of the power setpoint in the standard range between 1/60 (s) to 1/120 (s) as a maximum power setpoint gradient of change.

3.4. Protection for Line Inductor. Two widely used techniques for suppressing electromagnetic transients that generate high voltage are crowbar protection and MOV protection. Considering that MOV devices are more common in transmission lines and their compensation, this device is considered for the protection of the inductor. This system emulates the connection line [5] where the dynamics

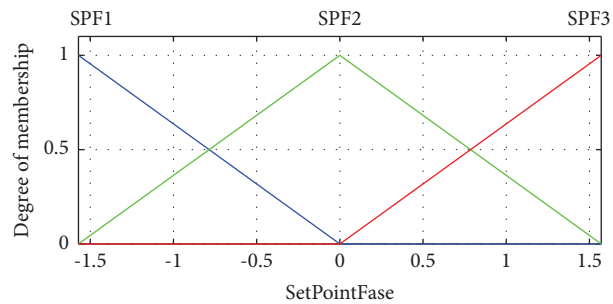

Figure 22: Membership functions of the phase setpoint.

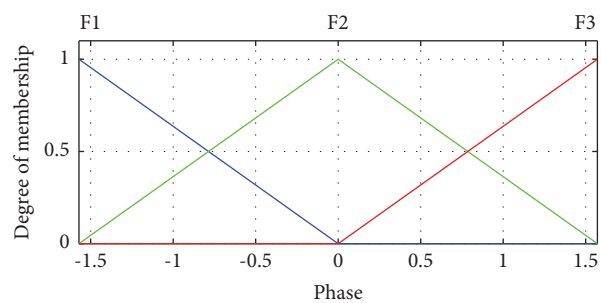

Figure 23: Membership functions of the real phase.

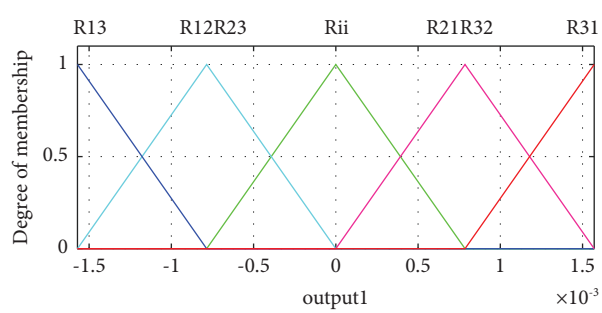

Figure 24: Membership functions of the phase variation prediction.

introduce a hysteresis behavior which can be simplified with the instantaneous equation presented in [6], as shown in equation (41), being I_{MOV} the MOV current, P the current per unit flowing through the MOV for when the voltage is applied V_{ref}, and $q = 7.2048$ the exponent that characterizes the MOV.

$$I_{\mathrm{MOV}} = P\left(\frac{V}{V_{\mathrm{ref}}}\right)^q. \tag{40}$$

The experimental case presented in [6] shows that $P = 155.9184$ (A), $V_{\mathrm{ref}} = 125.3540$ (V), and $q = 7.2048$ are the values obtained by applying the decreasing gradient to the experimental values in [5] according to the cost function presented in (41) and whose evolution is observed in Figure 30.

$$J = \frac{1}{2}\sum_{i=1}^{N}\left(\hat{I}_{\mathrm{MOV}} - I_{\mathrm{MOV}}\right)^2. \tag{41}$$

Table 13: Triangular membership functions corresponding to the phase setpoint.

mf	Parameters (p.u.)		
SPF1	−3.142	−1.571	0
SPF2	−1.571	$5.551e-17$	1.571
SPF3	0	1.571	3.142

Table 14: Triangular membership functions corresponding to the phase.

mf	Parameters (p.u.s)		
$F1$	−3.142	−1.571	0
$F2$	−1.571	0	1.571
$F3$	0	1.571	3.142

Table 15: Triangular membership functions corresponding to the prediction of the phase variation.

mf	Parameters (rad)		
$R1$	−0.000786	0	0.000785
$R2$	−0.001571	−0.000786	0
$R3$	−0.002357	−0.001571	−0.000786
$R4$	0	0.000785	0.00157
$R5$	0.000785	0.00157	0.002356

Considering that the transformer itself has an inductive effect, a protection connection is proposed as shown in Figure 31, making use of MOV S20K75 [6]. It is possible to model it by conserving the parameter $q = 7.2048$, and placing the values $P = 100$ (A) and $P = 100$ (A) as presented in the manufacturer's datasheet.

3.5. Power Droop Contribution to System Frequency Compensation. Studies aimed to evaluate the impact of reactive power (as a way of compensating the voltage profile of transmission grids) based on the administration of reactive power given by the participation of generating units with inverter systems with renewable energy as the primary source have been studied in [7].

However, even more necessary is the study that aims to improve participation by droop control for both active and reactive power to improve the participation of inverter electronic generating units working in parallel in a microgrid [27]. The work presented in [12] considers static, dynamic, and nonlinear droop to compensate for the frequency using power droop.

In this paper, the contribution due to power drooping of the inversion electronic generating units is proposed using the classic concept of the frequency dead band, with a drooping power corresponding to 4%, equivalent to a gain of 25, and a frequency dead band of 0.3%. Its implementation contributes effectively to the recovery of the system frequency in a way that affects the contribution of active power to the grid.

Table 16: Rules matrix of the phase variation characterization system.

Rule	mf DesPot	mf IntDesPot	mf phase	Weight	Operator And 1 Or 2
1	1	1	1	1	1
2	1	2	2	1	1
3	1	3	3	1	1
4	2	1	4	1	1
5	2	2	1	1	1
6	2	3	2	1	1
7	3	1	5	1	1
8	3	2	4	1	1
9	3	3	1	1	1

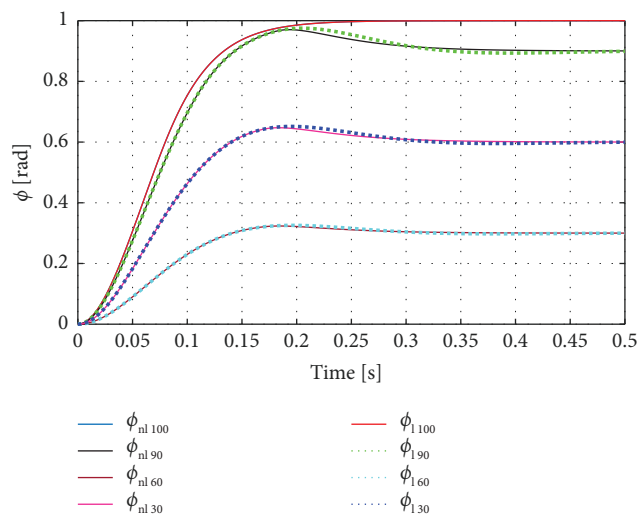

Figure 25: Phases of the linear and nonlinear models with fuzzy controllers for power setpoints of 30%, 60%, 90%, and 100%.

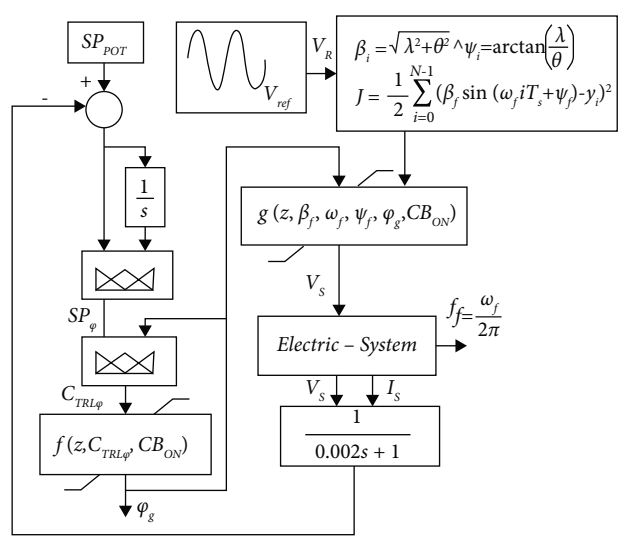

Figure 26: Model of the power control system, synchronization, and load taking.

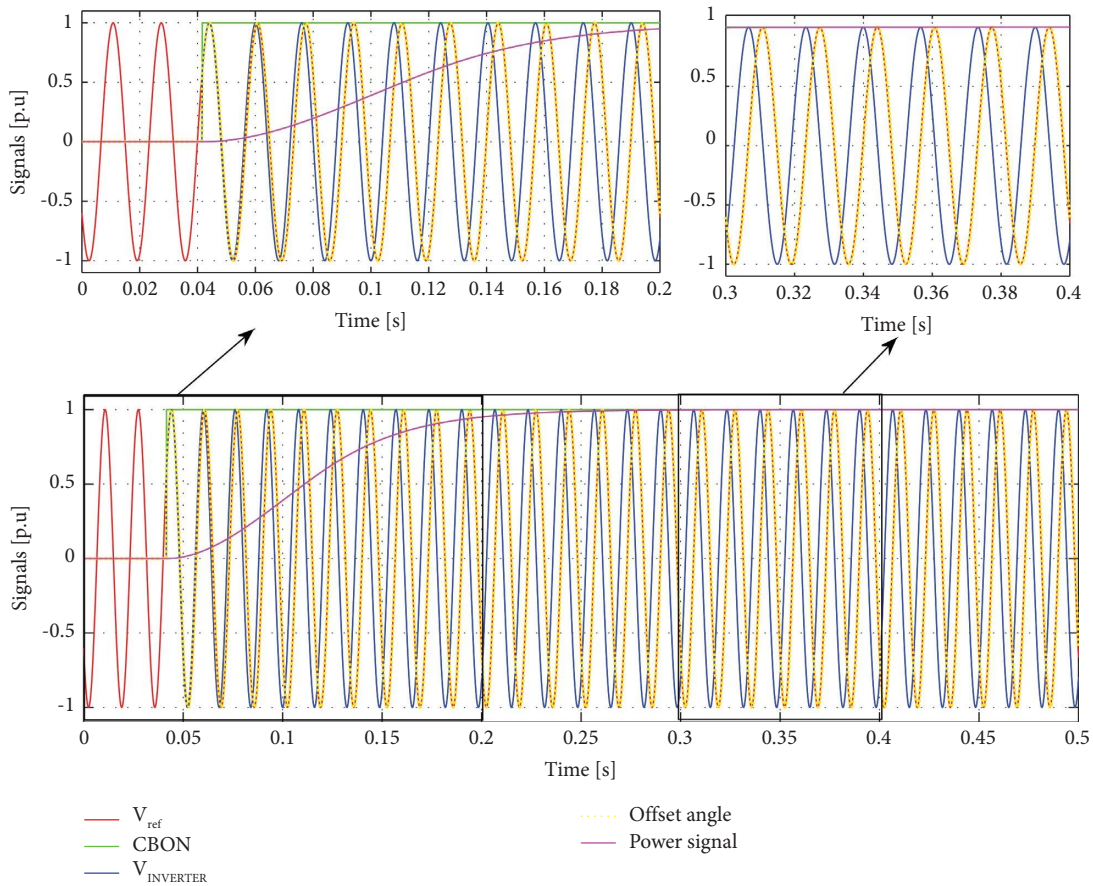

Figure 27: Simulation of the synchronization process: (blue) bus voltage signal, (red) signal breaker closing order, (orange) signal inversion system voltage, and (green) signal generated power.

Figure 32 shows the simulation diagram for evaluating the frequency compensation when the power regulation mode presents a power droop. Under the simulation condition, a frequency disturbance of ±2.3% is presented with a dead zone of 0.3%. Therefore, the process is done for ±2% of frequency variation for compensation purposes. This variation causes a compensation of ±50% of the power. Due to this fact, the simulation presents a setpoint of 50% such that the inverter system has control capacity.

When the frequency exceeds the regulation band of 0.3%, the power droop compensates for 2% above the regulation band, and the power must drop 50%. Therefore, if the setpoint is at 50%, the power must be at zero, and the phase condition must be 0° or 0 radians (or 0 in p.u.). Otherwise, if the frequency is below the regulation band of 0.3%, the power droop compensates for 2% below the regulation band. Here, the power must rise 50%, so if the setpoint is at 50%, the power must be at 100%, and the phase condition is 90° or $\pi/2$ radians (or 1 in p.u.).

Figure 33 shows this operating condition for power regulation during a frequency disturbance.

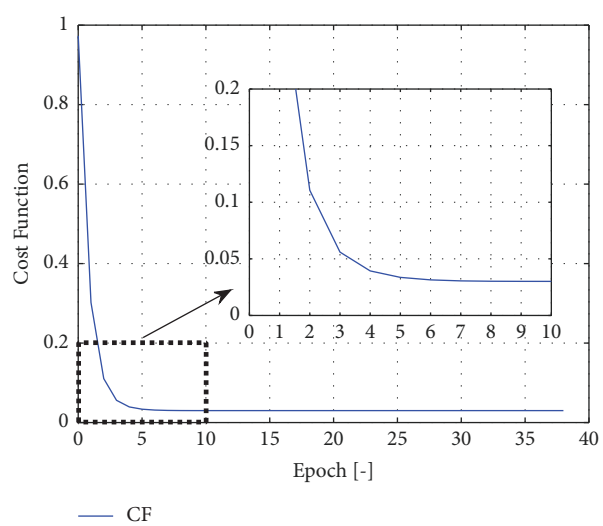

Figure 28: Simulation of the synchronization process: (blue) bus voltage signal and (red) signal breaker closing order evolution of the adjustment cost function of T_1, T_2, and T_3, of the equivalent power system.

3.6. Electronic Inverter System Coupled with a 10-Winding Transformer. In Section 3.4, the MOV was presented as protection for the line inductor, and Figure 30 showed the physical location of the MOV protection to suppress transients at the time of disconnection [24, 27]. This figure represents the connection of only one 10 (kW) inverter unit.

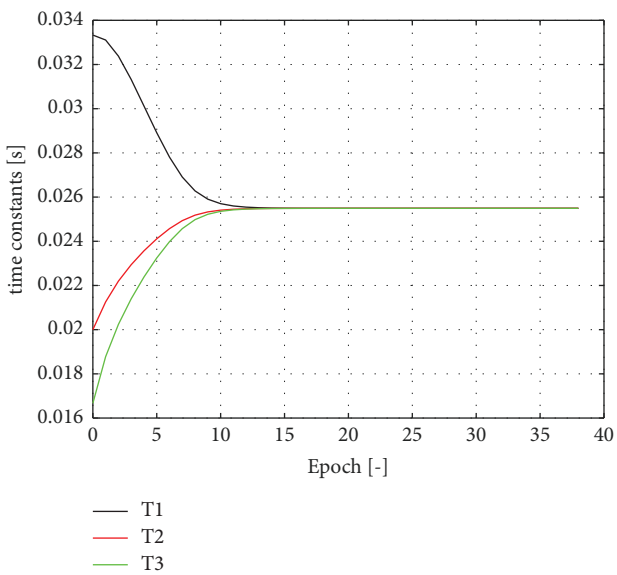

Figure 29: Evolution of the values of parameters T_1, T_2, and T_3.

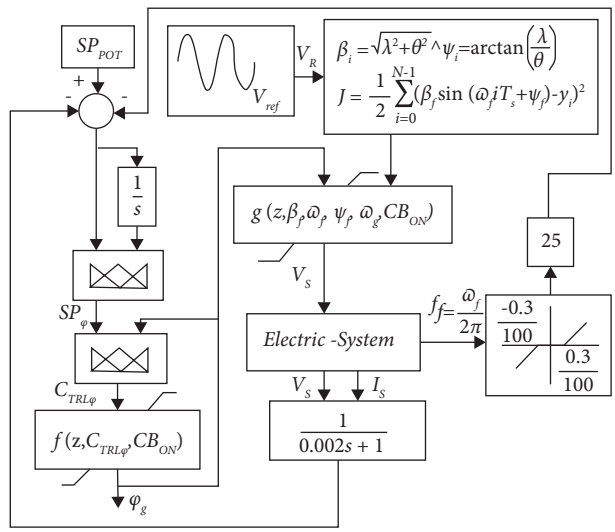

Figure 32: Simulation diagram of the frequency compensation due to power droop in regulation in power mode that affects the phase adjustment.

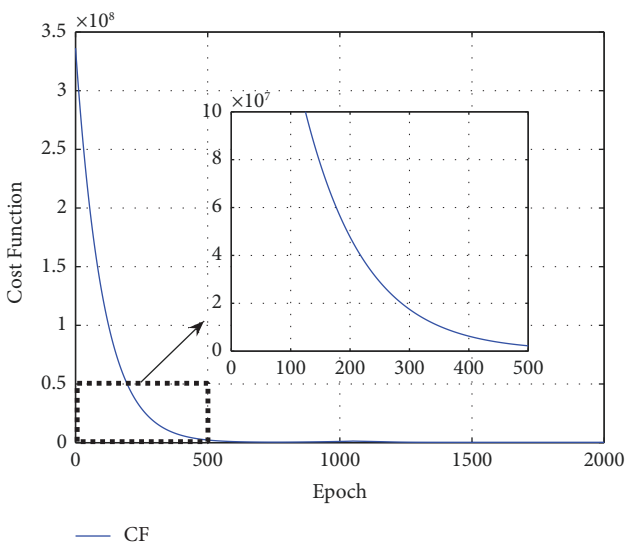

Figure 30: Evolution of the cost function in the search for parameters that best fit the experimental behavior of a MOV.

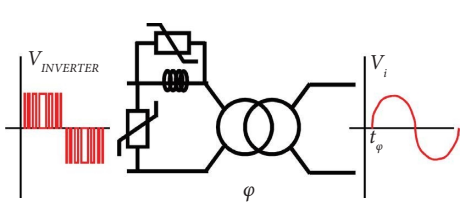

Figure 31: Physical location of MOV protection to suppress transients upon disconnection.

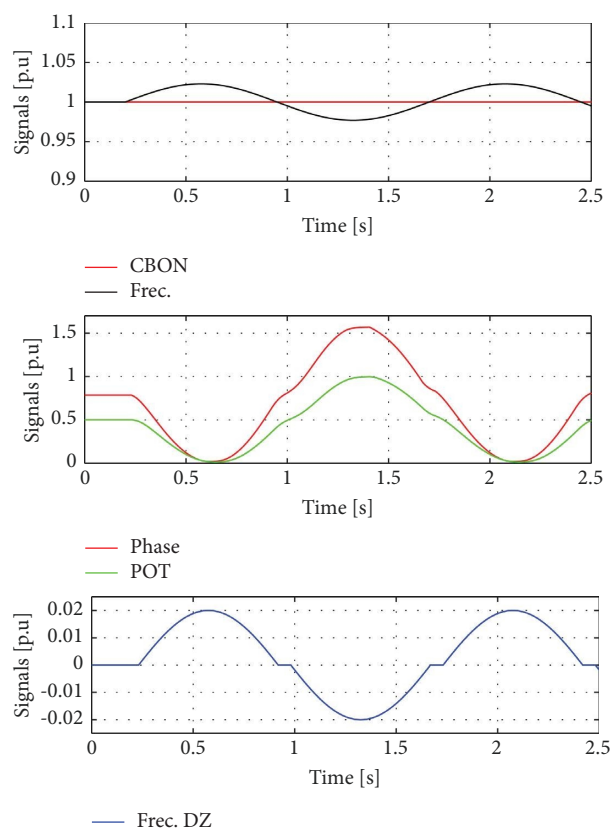

Figure 33: Behavior of the variables: frequency, frequency after the frequency compensation dead band, power, phase, and switch closed.

Due to cost and reliability facts, it is more robust than the 100 (kW) inverter system formed by 10 inverter units of 10 (kW), each one coupled through a power switch to a primary winding of a step-up transformer from 120 (V) to 13.8 (kV). Therefore, this distribution transformer contemplates 10 windings.

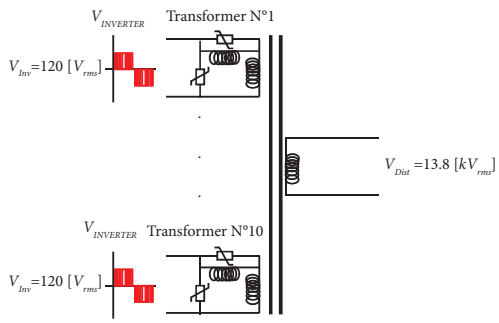

Figure 34: Step-up transformer with 10 primary windings and one secondary to inject power to the grid.

The design under this consideration presents more reliability, improvements for maintenance management, cost reduction in power management, and a better compensation effect when managing power plant criteria such as operation in power mode and operation in power mode with speed regulation.

Figure 34 shows the configuration of the step-up transformer, with the design specifications presenting 10 windings in the primary and one in the secondary. This design satisfies the power specifications and distribution voltage, considering the line inductor and the respective protections using MOV technology.

4. Conclusions

The conceptual development of an electronic inverter unit with the capacity to provide electrical energy to an interconnected system must take into account:

(1) To consider the filtering effect to achieve the THD in the synchronization process, taking into account that the grid voltage condition must be identified using correlational techniques that allow for lower computational costs because this algorithm must be running cyclically at all times.

(2) The nonlinear modeling that allows reproducing the behavior of the chirp function and the phase condition for synchronization is controlled by the time fuzzy controllers, which allow considering greater degrees of freedom for the adjustment of system performance.

(3) The implementation of the power correlation using neuro-fuzzy, reduced computational time when the rule of overlapping membership functions was implemented. Despite the direct programming of the fuzzy system, it offers better results than the application of computational tools that execute all the rules for determining the consequent aggregation.

(4) The importance of power correlation is in predicting operating conditions under fault when power should be generated under voltage and phase conditions, and the deviation concerning the measured power is determined.

(5) The consideration of dealing with power drooping is that this is the regulation modality on which these equipment operate. However, the degree of participation to try to correct grid frequency deviations must be taken into consideration.

(6) Modeling the equipment as a whole and obtaining a linear representation allow us to determine that the ability to follow the power setpoint does not require a correction and that, therefore, a gradient control is only necessary for ratio regulation power setpoint change.

(7) The consideration of the MOV as a transient overvoltage protection element minimizes the propagation of the fault that the presence of a crowbar could cause. This protection element was considered due to the inductive load represented by the transmission line and emulated when connecting the electronic inverter units to the grid.

(8) Considering the complete equipment by including ten units of 10 (kW) allows handling power elements to be subjected to less stress, increasing reliability, and improving the capacity and efficiency of the equivalent generator of 140 (kVA).

The static power flow study showed a contribution to the voltage increase in bus 2, associated with the substation that couples to the generation system by the inverter through the line emulated by the inductor. Likewise, bus 2 had a slight delay in phase (less than 1.5 degrees) concerning bus 1, associated with the connection node of the generator modeled by the Thevenin equivalent circuit.

The dynamic power flow study, taking into account that it was carried out considering linear models, showed the same response and settling time under different phase shift conditions between the voltages of buses 2 and 3 (with bus 3 being the voltage in the generator by inversion and bus 2 being the node associated with the coupling substation). The adjusted times to reach the power setpoint were 2 seconds for the five cases evaluated.

Finally, regarding fuzzy control, a Mamdani system was implemented instead of Sugeno because the models developed with Matlab are more efficient in terms of execution time. The critical aspect to remember is to demystify the fact that Sugeno is always a better inference method due to its ease of singleton adjustment. Mamdani, with the correct adjustment of its configuration, allows the application of the decreasing gradient for the positioning of the membership functions of the consequent,

taking into account the centroid method. This process is facilitated if a triangular or delta-type membership function is used (like the ones used in this paper).

Data Availability

Data required to reproduce the proposed study are already included in this manuscript.

Conflicts of Interest

The authors declare that they have no conflicts of interest.

References

[1] G. M. S. Azevedo, G. Vazquez, A. Luna, D. Aguilar, and A. Rolan, "Photovoltaic inverters with fault ride-through capability," in *Proceedings of the IEEE International Symposium on Industrial Electronics*, pp. 549–553, Seoul, Korea (South), July 2009.

[2] X. Chen, H. Liu, J. Su, and R. Qin, "The control strategy of energy storage system for primary frequency regulation and wind power ramp control," in *Proceedings of the 5th Asia Conference on Power and Electrical Engineering (ACPEE)*, pp. 652–656, Chengdu, China, June 2020.

[3] V. Vittal, J. D. McCalley, P. M. Anderson, and A. A. Fouad, *Power System Control and Stability*, Wiley-IEEE Press, Hoboken, NJ, USA, 2019.

[4] Ieee Power and Energy Society, *IEEE Guide for the Application of Turbine Governing Systems*, IEEE Power and Energy Society, New Jersey, NJ, USA, 2011.

[5] H. Chen and Y. P. Du, "A comprehensive study on the nonlinear behavior of metal oxide varistors," in *Proceedings of the 2016 33rd International Conference on Lightning Protection (ICLP)*, Estoril, Portugal, September 2016.

[6] U. J. Shenoy, P. Sandeep, and S. Srivastava, "Impact of MOV models on asymmetrical fault current calculations in fixed series compensated lines," in *Proceedings of the IEEE PES Asia-Pacific Power and Energy Engineering Conference (APPEEC)*, pp. 1–6, Bangalore, India, November 2018.

[7] R. A. Reyes, P. Rosales, and L. M. Castro, "Power system voltage profile evaluation considering renewable energy power plant reactive power droop control," in *Proceedings of the 2020 IEEE International Autumn Meeting on Power, Electronics and Computing (ROPEC)*, Ixtapa, Mexico, November 2020.

[8] S. R. Biswal, R. K. Sahu, and P. C. Pradhan, "Design and analysis of hybrid fuzzy FOPID-FOPI controller for frequency regulation of electrical power system," in *Proceedings of the International Conference on Computational Intelligence for Smart Power System and Sustainable Energy (CISPSSE)*, Keonjhar, India, July 2020.

[9] M. Rajabinezhad, A. Baayeh, and J. Guerrero, "Fuzzy-based power management and power quality improvement in microgrid using battery energy storage system," in *Proceedings of the 10th Smart Grid Conference (SGC)*, Kashan, Iran, December 2020.

[10] A. K. Verma, B. Singh, and D. T. Shahani, "Fuzzy-logic based MPPT control of grid interfaced PV generating system with improved power quality," in *Proceedings of the IEEE 5th Power India Conference*, Murthal, India, December 2012.

[11] A. Kirakosyan, E. F. El-Saadany, and M. S. El-Moursi, "Simultaneous voltage regulation and power sharing control algorithm for MTDC grids," in *Proceedings of the 2018 IEEE Electrical Power and Energy Conference (EPEC)*, pp. 1–6, Toronto, ON, Canada, October 2018.

[12] G. Tan and D. Wang, "Research on primary frequency regulation of wind turbine based on new nonlinear droop control," in *Proceedings of the 4th International Conference on HVDC (HVDC)*, pp. 170–174, Xi'an, China, November 2020.

[13] I. Koley, P. S. Bhowmik, and A. Datta, "Load frequency control in a hybrid thermal-wind-photovoltaic power generation system," in *Proceedings of the 2017 4th International Conference on Power, Control and Embedded Systems (ICPCES)*, pp. 1–5, Allahabad, India, March 2017.

[14] G. Wang and X. Li, "Approximation performance of the nonlinear hybrid fuzzy system based on variable universe," *Granular Computing*, vol. 2, pp. 73–84, 2017.

[15] G. Sharma, K. Narayanan, T. Adefarati, and S. Sharma, "Frequency regularization of a linked wind–diesel system using dual structure fuzzy with ultra-capacitor," *Protection and Control of Modern Power Systems*, vol. 7, no. 1, 2022.

[16] M. Barakat, "Optimal design of fuzzy-PID controller for automatic generation control of multi-source interconnected power system," *Neural Computing and Applications*, vol. 34, 2022.

[17] M. Fayez, F. Bendary, M. El-Hadidy, and M. Mandor, "Coordinated fuzzy operation of battery energy storage and resistive brake for mitigation of SSR oscillations," *Journal of Electrical Systems and Information Technology*, vol. 8, no. 1, 2021.

[18] M. Manas, B. J. Saikia, and D. C. Baruah, "Optimal distributed generator sizing and placement by analytical method and fuzzy expert system: a case study in Tezpur university, India," *Technology and Economics of Smart Grids and Sustainable Energy*, vol. 3, no. 1, 2018.

[19] H. Acikgoz, O. F. Kececioglu, C. Yildiz, A. Gani, and M. Sekkeli, "Performance analysis of electronic power transformer based on neuro-fuzzy controller," *SpringerPlus*, vol. 5, no. 1, 2016.

[20] S. Agarwal, A. Swetapadma, and C. Panigrahi, "Fault analysis method of integrated high voltage direct current transmission lines for onshore wind farm," *Journal of Modern Power Systems and Clean Energy*, vol. 7, pp. 621–632, 2019.

[21] P. Cross and X. Ma, "Model-based and fuzzy logic approaches to condition monitoring of operational wind turbines," *International Journal of Automation and Computing*, vol. 12, no. 1, pp. 25–34, 2015.

[22] M. Errouha, S. Motahhir, Q. Combe, and A. Derouich, "Intelligent control of induction motor for photovoltaic water pumping system," *SN Applied Sciences*, vol. 3, no. 9, 2021.

[23] A. Nasar Syed, *Theory and Problems of Electric Power Systems*, McGraw-Hill, New York, NY, USA, 1990.

[24] U. L. Csa and S. E. V. V. D. E. Cecc, "Leaded varistors standar D series," pp. 159–174, 2022, https://pdf1.alldatasheet.com/datasheet-pdf/view/182921/EPCOS/S20K50.html.

[25] Y. Ministerio de Regulación, "Recursos Naturales no renovables, Estadistica del Sector Electrico Ecuatoriano 2020," 2020, https://www.controlrecursosyenergia.gob.ec/wp-content/uploads/downloads/2021/09/Estadistica-2020-baja.pdf.

[26] Y. Ministerio de Regulación, "Recursos Naturales no renovables, Atlas del Sector Eléctrico Ecuatoriano," 2020, https://www.controlrecursosyenergia.gob.ec/wp-content/uploads/downloads/2021/06/Atlas-2020-baja.pdf.

[27] T. Wu, S. Member, Z. Liu, J. Liu, and S. Member, "A unified virtual power decoupling method for droop controlled parallel inverters in microgrids," *Transactions on Power Electronics*, vol. 8993, 2015.

Hindawi
Journal of Electrical and Computer Engineering
Volume 2022, Article ID 3074298, 12 pages
https://doi.org/10.1155/2022/3074298

Research Article

Improvement of the Resilience of a Microgrid Using Fragility Modeling and Simulation

Santhan Kumar Ch,[1] N. Karuppiah,[2] B. Praveen Kumar,[2] S. Shitharth,[3] and B. Dasu[4]

[1]*Department of EEE, Lords Institute of Engineering and Technology, Hyderabad, India*
[2]*Department of EEE, Vardhaman College of Engineering, Hyderabad, India*
[3]*Department of CSE, Kebri Dehar University, Somali, Ethiopia*
[4]*Department of EEE, Gudlavalleru Engineering College, Vijayawada, India*

Correspondence should be addressed to S. Shitharth; shitharths@kdu.edu.et

Received 4 March 2022; Revised 21 July 2022; Accepted 30 July 2022; Published 24 August 2022

Academic Editor: Ahmed A. Zaki Diab

The modern microgrid is designed to withstand various disruptive events that have a high probability of occurrence but have a low impact on the system. This improves the reliability of the system but does not take into consideration the disruptive events that have a low probability of occurrence but have a large impact on the system, such as extreme weather or natural disasters. Redesigning a microgrid to withstand low probability high impact events is very costly and is not a feasible solution to existing microgrids. This paper proposes a method to improve the resilience of an existing microgrid to quickly recover from low probability high impact events. The method used for this purpose is a combination of Monte Carlo simulation and prioritization of load of the microgrid. The efficacy of the method is examined by modeling microgrids using a fragility model. Using the proposed novel resilience index, the resilience of the IEEE 5-Bus system and IEEE 14-Bus system and the effect of load shedding on the resilience of the microgrid are analyzed and presented. The effect on smaller and larger grids and their resilience is examined. A novel resilience index is used to quantify the improvement of resilience of the proposed method when compared to other methods available in the literature.

1. Introduction

Power system resilience is defined as the capability of the power system to withstand and recover from any disturbance. With the use of modern controllers and advanced automatic control systems, the power system is able to withstand and recover from a wide variety of disturbances. This is due to the fact that the power system and control system are generally designed by taking the major disturbances into consideration and have been optimized to either automatically clear the disturbance or work around the disturbance without disrupting power supply to the consumers. This is achieved using the implementation of additional components to the power system to increase redundancy. This increases the reliability and resilience of the system. To optimize the increase in reliability, the major disturbances are selected to be modeled and analyzed based on a few criteria. A few prominent criteria are the frequency of the disturbance or probability of occurrence of the disturbance, the impact of the disturbance on the system or consumer, and the cost of implementing a solution to the disturbance. This increases the system's resilience to high-impact high-frequency events, such as lightning strikes, variation in load, etc., and low-impact high-frequency events, such as faults and fluctuations, etc. Low-impact low probability events are generally ignored at this stage and are dealt with as and when they occur on a case-by-case basis. This leaves the system vulnerable to high-impact low-frequency events, such as extreme weather conditions, natural disasters, cyberphysical attacks, geomagnetic storms, electromagnetic pulses, etc.

Microgrids are low voltage or consumer end systems with Distributed Energy Resources (DERs) together with storage devices and flexible loads. DERs include

microturbines, fuel cells, Photo Voltaic systems, etc., either singularly or a combination of them. Storage devices used may be flywheels, energy capacitors, batteries, or a combination of them. Such microgrids can be operated autonomously without connection to the power grid, i.e., in islanded mode or connected to work along with the grid connection. The operation of a microgrid in the distribution network provides immense benefits to the overall performance of the distribution system if it is efficiently controlled and coordinated. They usually cover only a small area of the overall network. In the event of an emergency or a failure of the system, the distribution network can be maintained by dividing into clusters of microgrids. The latest designs of distribution networks all include optimally placed DERs in the network for ease of division of the network into microgrids in the event of grid failure to provide uninterrupted power to the consumers. Microgrids tend to increase the complexity of the control system required to regulate the power distribution system while connected to the grid but require only simple control systems if run in islanded mode.

In [1], it is indicated that although extreme weather phenomena, such as cyclones, landslides, etc., have a low probability of occurrence, it is predicted that such events may increase in severity and probability in the future, and the power system must be made resilient to them in response. This calls for a major overhaul of the existing power system and redesigning it to be resilient against such extreme weather events using hardened infrastructure and redundant supply.

This is a very costly affair in both resources required, and research effort such as hardening the system to a great degree increases the brittleness of the system; i.e., the system will withstand a lot of disturbances, but if and when it fails, it becomes irreparably damaged and will have to be completely replaced. Extensive research will have to be done to determine the optimal hardness of the system without making it too brittle.

This affects different parts of the transmission network differently. On the high voltage side, such measures are very crucial and have already been implemented using superior transmission tower designs, wider spacing between the conductors, sturdy anchoring, and an increase in periodic maintenance. This is due to the high level of redundancy already available in high voltage networks over long distances; i.e., they are highly interconnected, and thus, they can be easily scheduled to be switched off and maintained or replaced. This mitigates the impact of extreme weather events at a high voltage level.

This is not true for the low voltage level of power distribution as the level of redundancy is not as high as that of the high voltage system. There is very limited space to increase the gap between conductors in residential areas to mitigate the effect of high wind speeds. There are also restrictions due to the proximity of existing residential complexes or apartments. This issue can be avoided by including these factors during the design of a new distribution area or residential area, but it is not feasible for existing networks as the process of implementing the recommended changes to the network is very cost-prohibitive. It is necessary to improve the resilience of the low voltage distribution systems, such as microgrids against extreme weather.

In the search for existing research on the topic of improvement of power system resilience, the resulting papers have been analyzed based on three key attributes. These attributes are not exhaustive and do not extend to all the papers researched. The attributes are as follows: problem solved, the method of the solution implemented, and test cases used. While almost all of them comment on the effect of severe weather on the power system, they approach the problem in different ways. Panteli et al. [1] used fragility curves to assess the impact of extreme weather on a simplified 29-bus Great Britain transmission network. Panteli et al. [2] used defensive islanding to improve resilience on the simplified 29-bus network. The improvement of the system function in zones 2,3 and 4 was observed due to this strategy. Najafi et al. [3] used a social welfare-based index and genetic algorithm to improve resilience on an IEEE 33 node system. The targeted improvement of the system in zone 4 in sync with the codependent water system greatly enhanced the resilience of the system in accordance with the demand. Gao et al. [4] used Linear Integer Programming (LIP) to emulate all feasible paths of restoration of the system to determine the optimal restoration of critical loads on an IEEE 123 node feeder system. The targeted improvement of the system resilience in zone 4 was highly cost-effective. Xu et al. [5] also used LIP to restore critical loads on the microgrids of the distribution system of Pullman, Washington and were focused on the improvement in zone 4 of the system resilience. Ma et al. [6] used the greedy search algorithm to minimize the cost of hardening of system and load shedding to improve resilience in a modified Electric Power Research Institute (EPRI) test circuit. The improvement to both zone 2 and zone 4 was significant. Farzin et al. [7] used Mixed Integer Linear Programming (MILP) to enable the smart distribution of resources in a three microgrid test system to improve resilience. The research was targeted toward improvement in zones 3 and 4 while minimizing the cost of the improvement. Bajpai et al. [8] used Graph theory and Choquet Integral to maintain critical load supply in IEEE 123 node distribution system. The target was to reduce the impact on zone 2 and increase the recovery in zone 4. Li et al. [9] used a combination of fragility curves and the Monte Carlo method to determine the optimal location for the integration of DERs in an IEEE 37 bus network. The target was to improve the resilience in zone 1 and reduce impact in zone 2. Huang et al. [10] used a nested column-and-constraint generation decomposition, generator redispatch, topology shifting, and load shedding to improve the resilience of a modified PJM 5 bus system, IEEE one area RTS-96 system, and IEEE three area RTS-96 system. The improvement was observed in zones 1, 2, 3, and 4. Zarre-Bahramabadi et al. [11] used MILP optimization to determine the optimal placement of switches to improve the resilience of Bus 4 of the Roy Billinton test system. Zones 1 and 2 showed improvement due to this method. Mousavizadeh et al. [12] used MILP to analyze the resilience of a modified 118 bus test system and one 20 kV distribution

network in Tehran, Iran. Gholami et al. [13] observed the working of a resilient microgrid using a two-stage stochastic programming approach and its ability to reduce the impact of electric interruption by using the microgrid capabilities of the IEEE 33-bus test system used. Eshghi et al. [14] proposed metrics for the grading or ranking of optimal operation of a smart grid using state estimation and adaptive response techniques and their advantages. Chanda and Srivastava [15] used percolation theory and a hierarchical analytical process to define and quantify the resilience of an electrical distribution system with multiple microgrids. Panteli et al. [16] used time-dependent resilience metrics to quantify and analyze the different phases that a power system may experience during an extreme event of the 29-bus Great Britain transmission network. Panteli et al. [17] gave a comprehensive understanding of the use of hardening and implementation of smart control as strategies to improve resilience on the 29-bus Great Britain transmission network. Xu et al. [18] used a look-ahead load restoration strategy to determine the optimal restoration strategy to improve the resilience in zone 4 of the modified IEEE 342-node low voltage network. Singaravelan and Kowsalya [19] used load shedding and fuzzy logic techniques to prolong the supply of power to the islanded microgrids of a modified IEEE 34-node sample system and thus improved the resilience in zones 2 and 3 of the network. Nikmehr et al. [20] used metaheuristic algorithms under the condition of uncertainties of loads and DERs to determine the optimal scheduling of generators on a microgrid-based smart grid. Chen et al. [21] used a sequential service restoration framework and MILP techniques to optimally integrate smart grids, such as a modified IEEE 123-node test feeder. Ji et al. [22] used Soft Open Point (SOP) and MILP techniques to improve load recovery and increase the resilience in zones 4 and 5 of the IEEE 33-node and IEEE 123-node test feeders. Chanda et al. [23] used and evaluated a dynamic optimization algorithm to change the operating criteria to increase the ability of the two connected CERTS microgrids to ensure quality supply to the most critical loads of the system. Chen et al. [24] used MILP, remote-operated switches, and DERs to restore critical loads of a modified IEEE distribution rest system and increase resilience in zone 4 of the system. Panteli and Mancarella [25] used a sequential Monte Carlo-based time-series simulation and fragility curves to improve the resilience of an IEEE 6-bus test system in order to reduce the impact of severe weather on the system. Gholami and Aminifar [26], MILP, and Benders' decomposition techniques were used to facilitate restoration, reduce outage duration, and reduce damage to critical system components of an IEEE 39-bus system to increase resilience in zones 1, 2, 3, and 4 of the system. Reed et al. [27] used fragility, outage restoration, and interdependency analysis techniques to understand and quantify the behavior and resilience of the system using data collected during Hurricane Katrina. Arab et al. [28] used MILP and Benders' decomposition algorithm to determine the optimal repair schedule, generator commitment, and network configuration of an IEEE 118-bus test system to increase its resilience to disasters and improve resilience in zones 1, 2, 3, and 4 of the system. Eder-Neuhauser et al. [29] used the implementation of a decentralized and self-organizing structure to qualitatively evaluate the resilience and security of a smart grid with an Information and Communication Technology (ICT) topology. Eskandarpour and Khodaei [30] used machine learning-based outage prediction to determine the potential outage of the power grid components in a hurricane. Liang et al. [31] used the control of Electric Springs implemented in a microgrid with ES Topology to enhance the resilience of microgrids using frequency and voltage control. Liu et al. [32] used a four-loop switching controller implemented in a modified IEEE 16-generator 68-bus power system to improve the transient stability of power systems with wind power integration. Liu et al.[33] used the Monte Carlo method to improve the resilience of IEEE 30-bus and 118-bus systems by determining the optimal microgrid clustering of the system and also studied [34]. An optimal active power dispatch can also be done by using deep reinforcement learning [35].

Ali et al. [36–38] discussed the optimal planning of autonomous microgrids in the presence of uncertain PV and wind generation units, PEV charging stations/parking lots, and proposed a bilevel metaheuristic and a two-level multiobjective evolutionary algorithm-based solution to address the complex planning model.

From the literature, it is made clear there is a need to develop a methodology to address and study the resilience of a microgrid subjected disrupting events having a larger impact on the microgrid. In this work, it is proposed to use a combination of Monte Carlo simulation and load shedding to improve the resilience of the power system. Monte Carlo simulation is used to simulate the effect of wind on the system using random variables with normal distribution and the effect of load shedding on the resilience of the system.

The rest of the paper is organized as follows. Section 2 presents the fragility modeling, the resilience of the power system, and possible strategies to improve resilience. Section 3 presents the overview of the simulation, test models of the power system used, a brief overview of the Monte Carlo simulation method and load shedding algorithm used, the overall simulation flowchart, and the results obtained from the simulation. Section 4 summarizes and concludes the paper.

2. Fragility Modeling and Resilience Assessment

2.1. Fragility. Fragility is the probability of failure of a structure based on a specific parameter. In a system, the probability of failure depends on the fragility of the weakest or the most vulnerable component in the system. This depends heavily on the intensity of the parameter in question. A fragility function is a mathematical relation between the failure probability of a component and the specific parameter intensity acting on or experienced by the component either directly or indirectly. For example, the fragility function of a transmission pole depends on the intensity of the shaking of the ground in an earthquake or the force experienced by the transmission pole due to the high-speed spiraling wind blowing on it in a cyclone. Figure 1 shows the

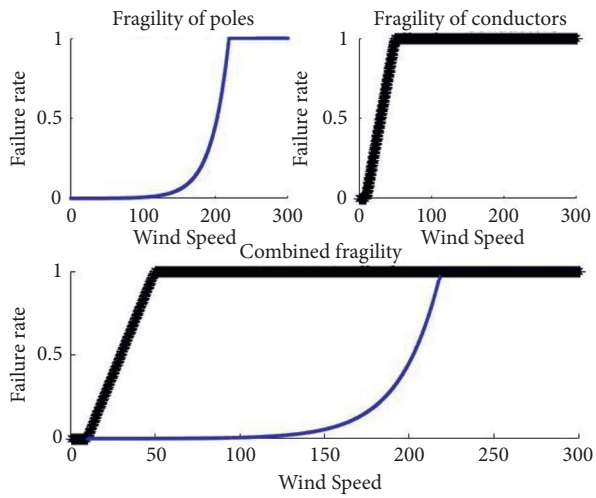

Figure 1: Fragility curves of transmission poles and conductors w.r.t wind speed.

fragility curves for transmission lines subjected fragility of poles, conductors, and combinations. From the figure, it is clear that poles are impacted at higher wind speeds, and conductors have an adverse impact even at lower wind speeds, and it is also shown the combined fragility of the system.

2.2. Resilience. The ability of the system, including generating sources, transmission, and distribution, to bounce back from high-impact low-frequency events is called resilience. This could include events that are natural, such as cyclones, earthquakes, or ice storms, etc., as well as man-made, such as cyber or physical attacks on grid infrastructure. The system is represented by a system function F(t) which indicates the state of the system at a time *t,* as illustrated in Figure 2.

2.2.1. Zone 1 (Normal State). This represents the state of the system before the disruption event. This is the designed state of the system. The system will continue to be in this state until there is a disruption to the system.

2.2.2. Zone 2 (Disruption State). This represents the state of the system after the disruption until the failure of the system. The system function falls due to either the failure of system components or due to preventive measures programmed into the system in response to specific stimuli. The degree of fall in the system function depends upon the severity of the disruption and the preventive measures taken by the implemented control system.

2.2.3. Zone 3 (Fail State). This represents the state of the system after the failure of the system until the recovery of the system is attempted. The system function stays in this state until the repair or replacement of damaged components of the system after the disruption event is over. The duration of this state depends upon the severity of the disruption event and its duration.

2.2.4. Zone 4 (Restoration State). This represents the state of the system after the attempted recovery starts until the system reaches the recovered state. In this state, the power system undergoes repair or replacement of damaged components of the system. The level of recovery of the system function and the rate of recovery depends on factors such as the measures taken by the system operator, the resilience of the system, etc.

2.2.5. Zone 5 (Recovery State). This represents the state of the system after the system reaches the recovered state. The system continues to be in this state until there is another disruption or heavy repairs or replacement of damaged components due to the disruption. This state does not change until there is a change in the structure of the power system.

2.3. Possible Solutions. There are a wide variety of strategies that can be implemented to improve the resilience of a system. These strategies can either be individually implemented or implemented together in a group. The strategy to be implemented depends upon the zone of the resilience of the system to be targeted for improvement. A few strategies categorized by their targeted zone of improvement are as follows.

2.3.1. Zone 1 Improvement. In this zone, the goal of improvement is to prevent damage to the system. This can be achieved by predicting the occurrence of the disruption by analyzing previous disruptions, determination of weak points in the system, analysis of the cause of the disruption, and forecasting the conditions in which the disruption occurs. These strategies work well with the strategies implemented in zones 2 and 5.

2.3.2. Zone 2 Improvement. In this zone, the goal of improvement is to reduce the severity of the impact of the disruption or reduction in the rate of degradation of the system, or both. This can be achieved by hardening of the most vulnerable power system components, increasing the level of redundancy in the system. These strategies work well with the strategies implemented in zones 1 and 3.

2.3.3. Zone 3 Improvement. In this zone, the goal of improvement is to reduce the duration of the failed state. This can be achieved by implementing backup reserves, optimal placement of service centers in an area, and improving identification of the location of the damaged components of the system. These strategies work well with the strategies implemented in zones 2 and 4.

2.3.4. Zone 4 Improvement. In this zone, the goal of improvement is to increase the rate of recovery of the system or improve the level of recovery, or both. This can be achieved by implementing load shedding, prioritization of load, installation of optimally placed DERs, and optimal clustering

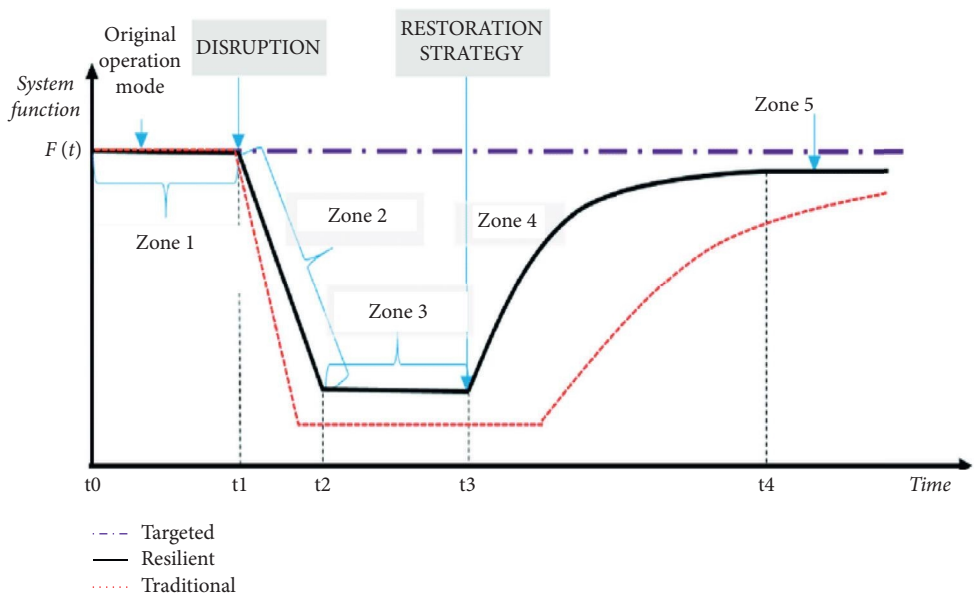

Figure 2: Representation of system resilience.

of microgrids. These strategies work well with the strategies implemented in zones 3 and 5.

2.3.5. Zone 5 Improvement. In this zone, the goal of improvement is to maintain the new stable state of the system and bring the system back to its original state. This can be achieved by a restructuring of the system, replacement of damaged components, analysis of the effect of the disruption, and archiving of the same for future use, etc. These strategies work well with the strategies implemented in zones 4 and 1.

2.4. Proposed Index. It is observed that after the Monte Carlo simulation, we can find the average power generated by a bus in all the scenarios run by the simulation. The probability of being in a specific state of the power generation in each bus is determined by counting the number of occurrences divided by the number of simulations. The Average Total Power Generated (ATPG) and the Average Total Power Consumed (ATPC) at each bus are also determined from the simulation data as follows:

$$\mathrm{ATPG} = \frac{\sum_{i=1}^{\mathrm{iter}} \mathrm{TPG}(i)}{\mathrm{iter}}, \tag{1}$$

where iter is the total no. of iterations of the Monte Carlo simulation, TPG(i) is the Total Power Generated in ith iteration of the Monte Carlo simulation as follows:

$$\mathrm{ATPG} = \frac{\sum_{i=1}^{\mathrm{iter}} \mathrm{TPC}(i)}{\mathrm{iter}}, \tag{2}$$

where iter is the total no. of iterations of the Monte Carlo simulation, TPC(i) is the total power consumed in ith iteration of the Monte Carlo simulation as follows:

$$\begin{aligned} P_G &= \frac{\mathrm{ATPG}}{\text{Total base power generated}}, \\ L_s &= \frac{(\mathrm{ATPC} - \text{Total base power consumed})}{\text{Total base power consumed}} * 100, \\ \text{resilience index}\,(RI) &= (a * P_G) + (b * L_s), \end{aligned} \tag{3}$$

where a and b are coefficients assigned to the system as follows:

$$\begin{aligned} a &= \frac{1}{\text{no of buses in the system}}, \\ b &= \frac{1}{\text{no of loads in the system}}. \end{aligned} \tag{4}$$

3. Modeling and Simulation

The probability of failure of the power system components is determined by using the fragility function with wind speed as input and the probability of failure as the output. It is determined to use the fragility curve of a power line as it is the most sensitive to wind speed. In this case, the conductors are the weakest link in the power system distribution chain and are most likely to be a point of failure due to the pressure caused by the wind [3]. Therefore, the equation for the fragility of a conductor becomes as follows:

$$\begin{aligned} \mathrm{pfc} &= 0\ \forall\, w_s \langle w_{\min}, \\ \mathrm{pfc} &= \frac{(w_s - w_{\min})}{(w_{\max} - w_s)}\ \forall\, w_{\min} \le w_s \le w_{\max}, \\ \mathrm{pfc} &= 1\ \forall\, w_s \rangle w_{\max}, \end{aligned} \tag{5}$$

where pfc is the probability of failure of a conductor, w_s is the speed of the wind in the local area, $w_{\min}$ is the minimum

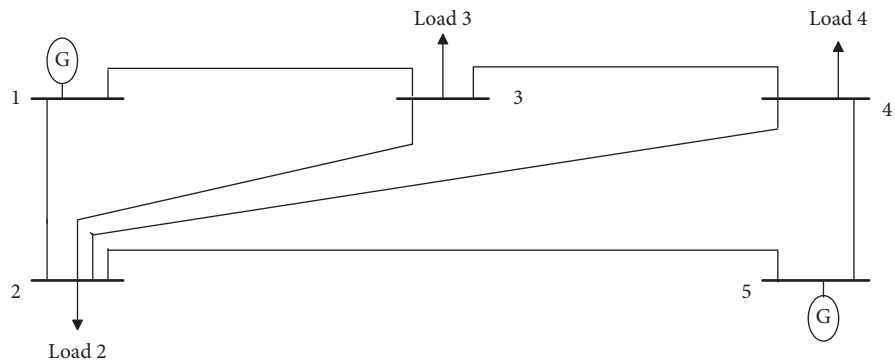

Figure 3: Single line diagram of an IEEE 5-bus System.

wind speed required for failure below which the conductor does not fail due to the wind, and $w_{\max}$ is the maximum wind speed above which the conductor is sure to fail.

3.1. Systems Studied. The models used for simulation are as follows, IEEE 5-Bus system depicted in Figure 3, is used for simulation of the power system consisting of five buses and seven lines. IEEE 5-Bus system depicted in Figure 4 is used for simulating power system configuration, which consists of 14 buses and 20 lines.

The simulation and implementation of the solution to the test cases in consideration would be meaningless without comparison with base steady-state data obtained using power flow equations. Of the wide variety of power flow equations available to determine the flow of power in the system at a steady state, a few are the Gauss-Seidel method, Newton-Raphson method (NR method), fast decoupled load flow method, DC load flow method, etc. Each method has its own advantages and disadvantages based on the assumptions made in the calculation of the power flow. Of these, we use NR load flow to determine an accurate load flow with a very small number of steps. The disadvantage of longer calculation time and larger memory requirement of NR load flow method is overcome by the speed and capability of the latest computers and also the vast boost to computing power afforded by graphical processing units (GPUs) that perform a large number of calculations simultaneously.

3.2. Monte Carlo Simulation. It is one of the deterministic approaches to the solution of a problem in which multiple random variables are used to make numerical estimations of complex situations. It is generally used to calculate the impact of a parameter on the system by running a large number of iterations of the simulation of the system in which the parameter in question is slightly different in value or completely random based on a selected random distribution. It gives us the probability of the system being in a certain state by adding up the number of times the target state is achieved during the course of the Monte Carlo simulation. The selection of the type of random distribution is decided based on the parameter in question and its behavioral tendencies. Generally, the random number is chosen to be with a uniform distribution where all possible values within

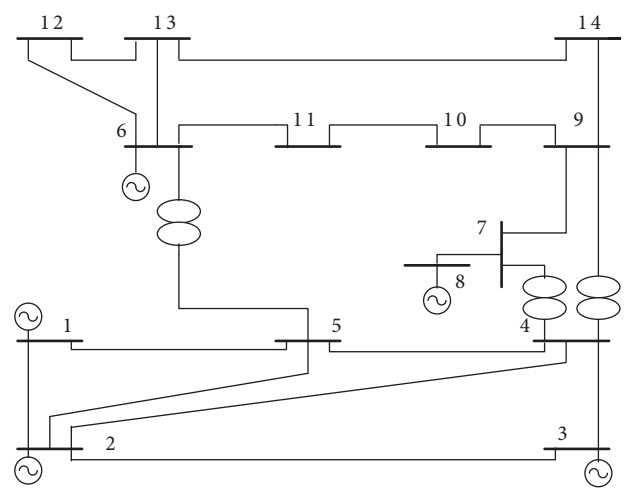

Figure 4: Single line diagram of an IEEE 14-bus System.

a range are equally probable, or it is chosen to be with normal distribution to emulate the probabilities found naturally in nature.

The Monte Carlo simulation technique is used to emulate the effect of high-speed wind on the test system by the use of a normally distributed random number to represent the wind speed and comparison with the reduced fragility function adjusted to the natural tendency of wind to determine the failure state of the transmission line in question and its effect on the system. Since the goal is to quantize the resilience of the system, the state of the system is observed using specifically designed indices. In this case, the total power generated, the total load supplied, the ratio of power generated to the power consumed, etc. The end goal is to maximize the total load supplied while minimizing the total generation shift during a failure.

3.3. Load Shedding. It is not always possible to satisfy all the loads in a system during a breakdown of one of its components. In such cases, load shedding is one of the solutions implemented to temporarily reduce the demand on the system to a more manageable state depending upon the generating capability of the system.

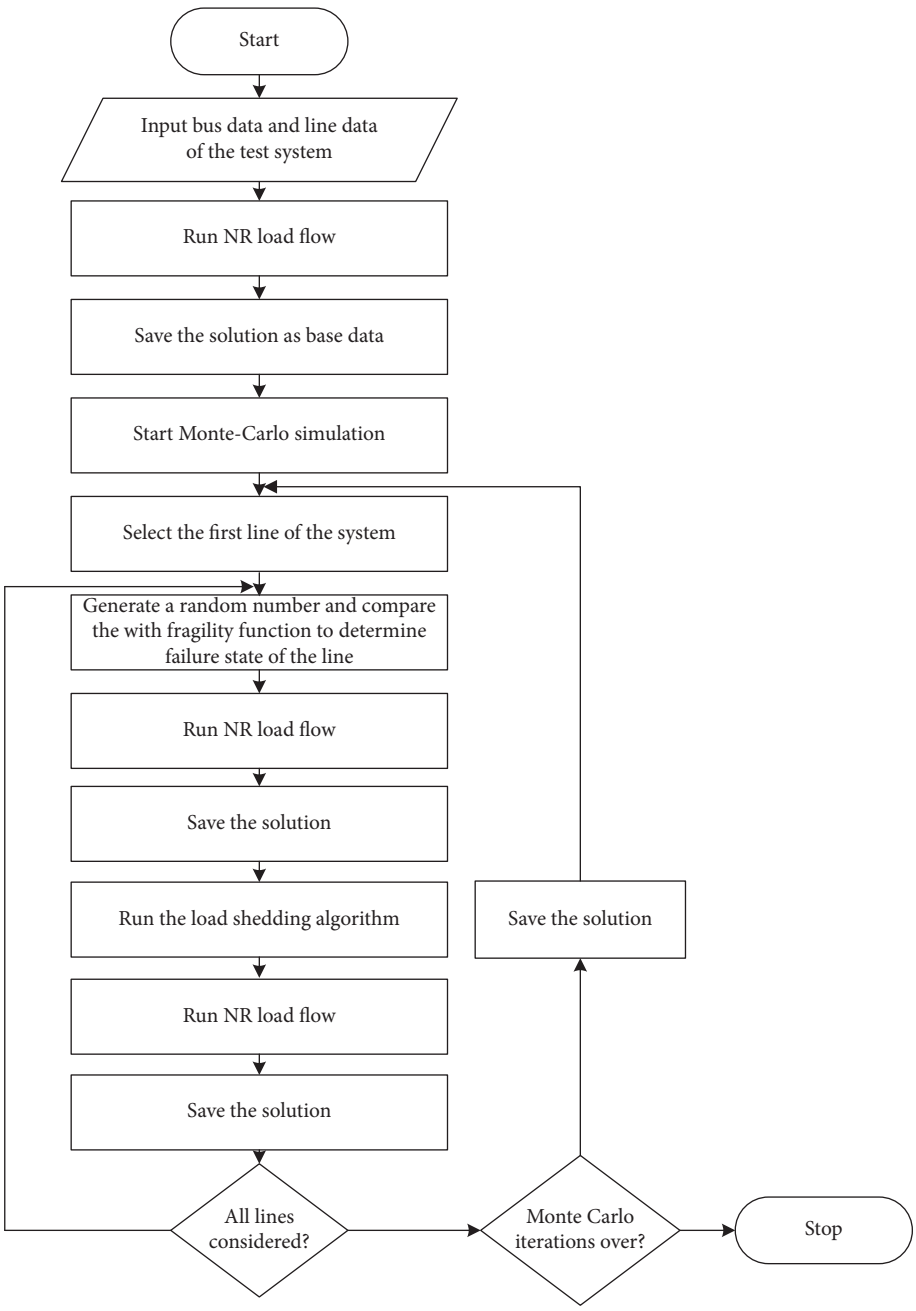

Figure 5: Flowchart representation of the simulation.

The process of load shedding is traditionally done by either completely dropping the smallest noncritical load or reducing the highest noncritical load by a nominal amount. There are large variations of this method available for use based on the demand and individual requirements. Critical loads are always a priority and are to be supplied at any cost, even if all the noncritical loads must be shed to do so. Only in the event of a risk of a hazard is a critical load to be shed. In extreme conditions where power grid supply is not available, and the installed DERs in the network do not have enough capacity to supply the demands of the islanded microgrid network, load shedding is the last hope for the continuation of supply after all other methods fail.

In the case of the current experiment, the Monte Carlo simulation is run both with and without load shedding to compare both strategies and their effect on resilience by comparison of the resilience indices.

3.4. Simulation Flowchart. The simulation flowchart is shown in Figure 5.

3.5. Result. Upon Monte Carlo simulation of the test systems, we obtain the probability distribution of the power generated at each bus of the system. The cumulative power distribution curve gives the cumulative probability of the

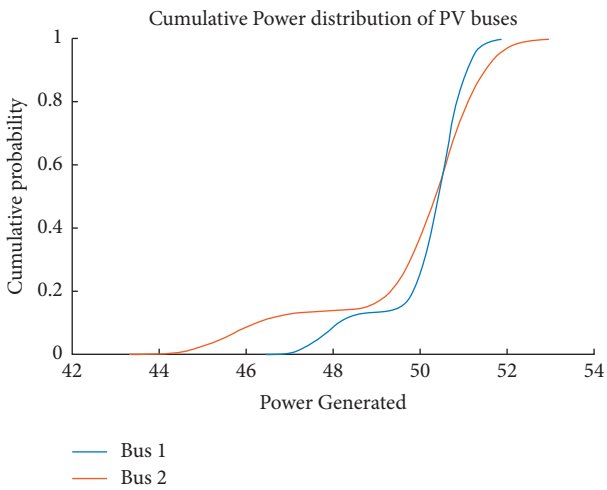

Figure 6: Cumulative power distribution at buses 1 and 2.

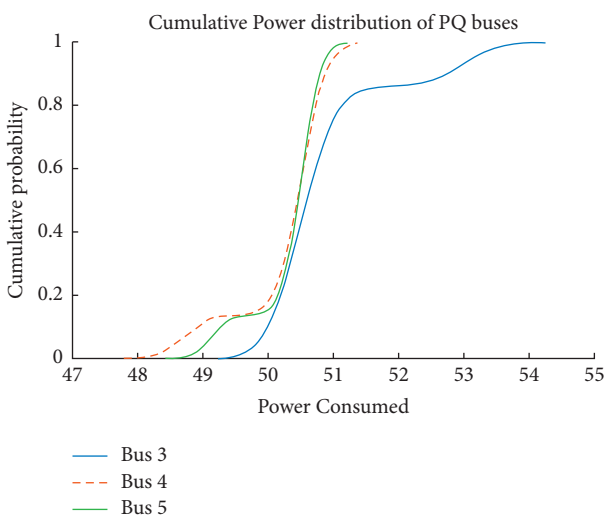

Figure 7: Cumulative power distribution at buses 3–5.

power et al. values of power. The most probable power magnitude is obtained by identifying the largest change in the cumulative probability within the neighborhood of the tolerance of the power value. The probability density curve gives the density of probability of the value of power. The probability of a specific power magnitude is the area under the curve around the neighborhood of the power value. The commutative power distribution for PV and PQ buses (buses 1–5) before load shedding for the IEEE-5 bus system is shown in Figures 6 and 7.

For the IEEE 5-Bus system without load shedding, the total power generated was found to be 234.3689 MW compared to the base power generation of 21.4769 MW. While total power consumed was found to be 1.2235 MW compared to base power consumed at 1.699 MW. The weights $a = 1/5$ and $b = 1/3$.

Therefore, $L_S = 27.98$, $P_G = 10.91$, and $\mathrm{RI} = 11.50$.

The power density distribution for buses 1,2, and buses 3,4, and 5 before load shedding for the IEEE-5 bus system are

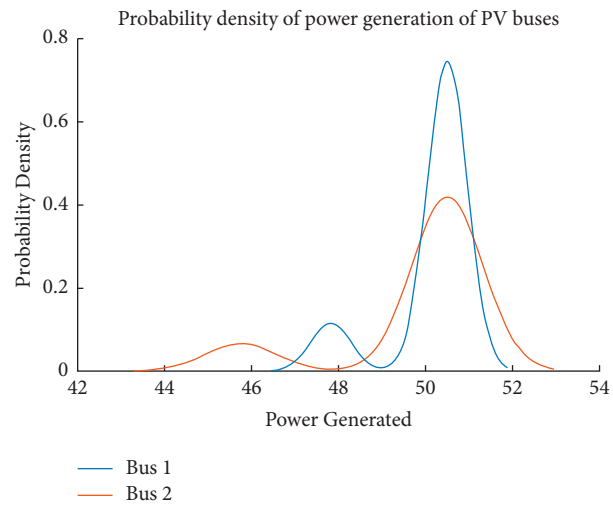

Figure 8: Power density distribution at buses 1 and 2.

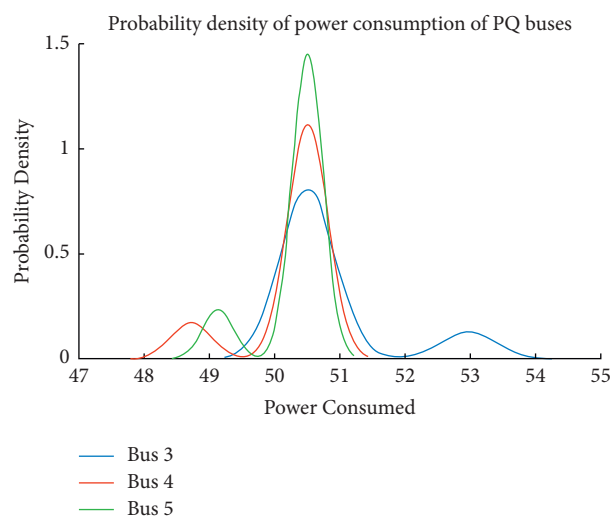

Figure 9: Power density distribution at buses 3–5.

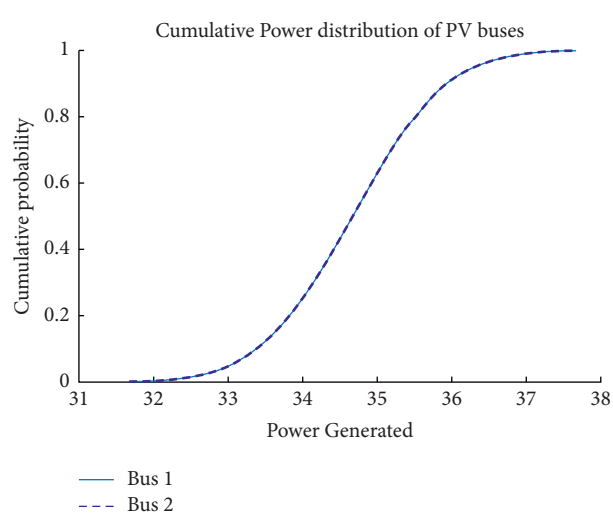

Figure 10: Cumulative power distribution at buses 1 and 2.

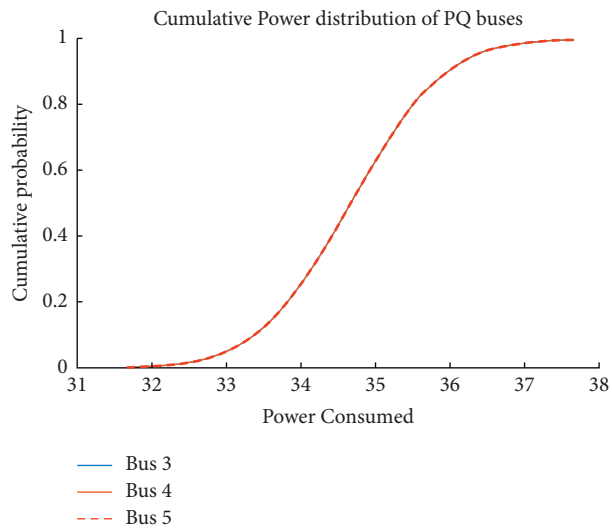

Figure 11: Cumulative power distribution at buses 3–5.

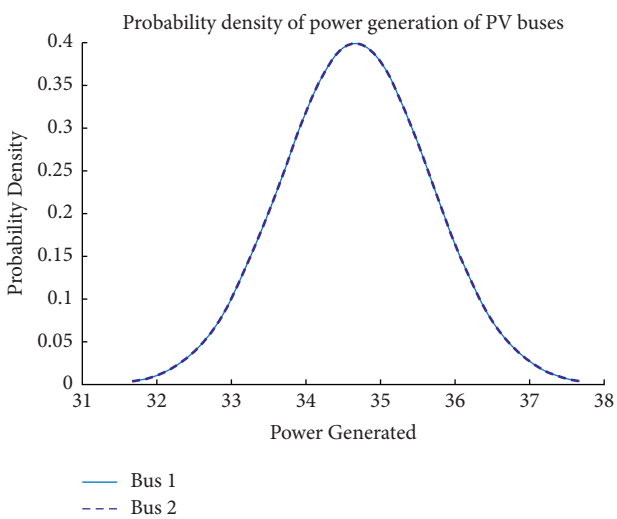

Figure 12: Power density distribution at buses 1 and 2.

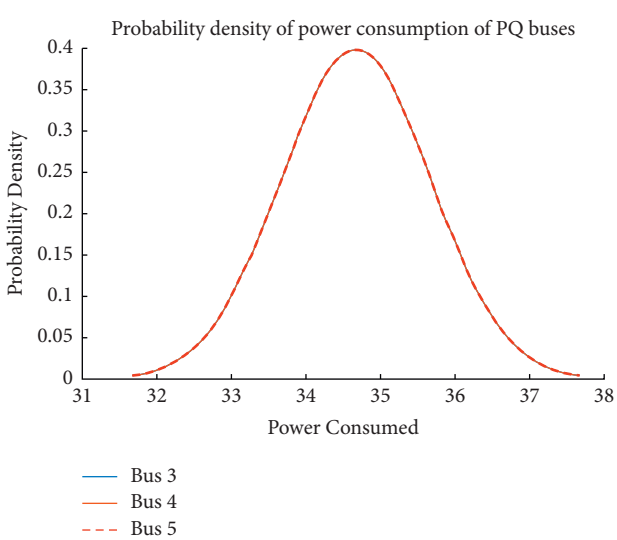

Figure 13: Power density distribution at buses 3–5.

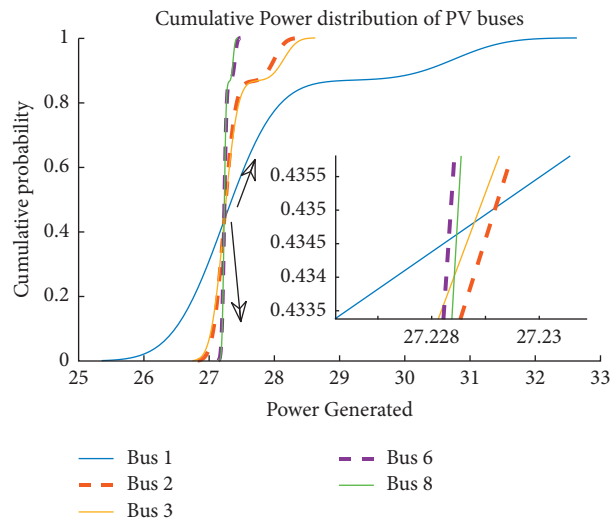

Figure 14: Cumulative power distribution at buses 1, 2, 3, 6, and 8.

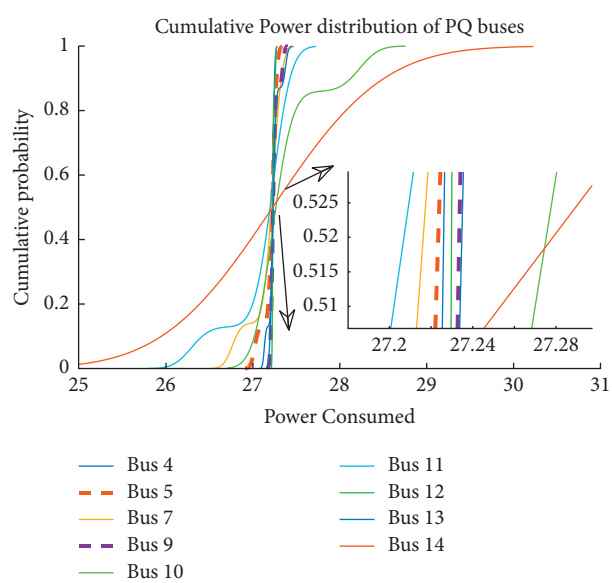

Figure 15: Cumulative power distribution at buses 4, 5, 7, and 9–14.

shown in Figures 8 and 9. Figure 8 shows the slack and generator buses, and Figure 9 shows for load buses.

The commutative power distribution for PV and PQ buses (buses 1–5) after load shedding for the IEEE-5 bus system is shown in Figures 10 and 11.

For the IEEE 5-Bus system with load shedding, the total power generated was found to be 172.8266 MW compared to the base power generation of 21.4769 MW. While total power consumed was found to be 1.2236 MW compared to base power consumed at 1.699 MW. The weights $a = 1/5$ and $b = 1/2$.

Therefore $L_S = 27.98$, $P_G = 8.04$, and $\mathrm{RI} = 15.9$.

The power density distribution of buses 1, 2, and buses 3, 4, and 5 after load shedding for the IEEE-5 bus system are

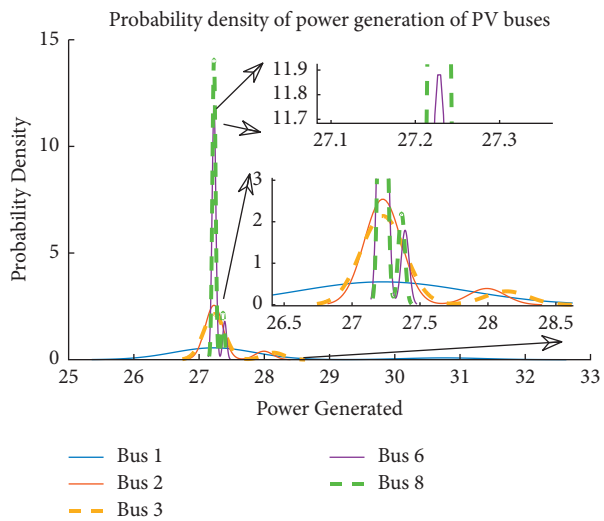

Figure 16: Power density distribution at buses 1, 2, 3, 6, and 8.

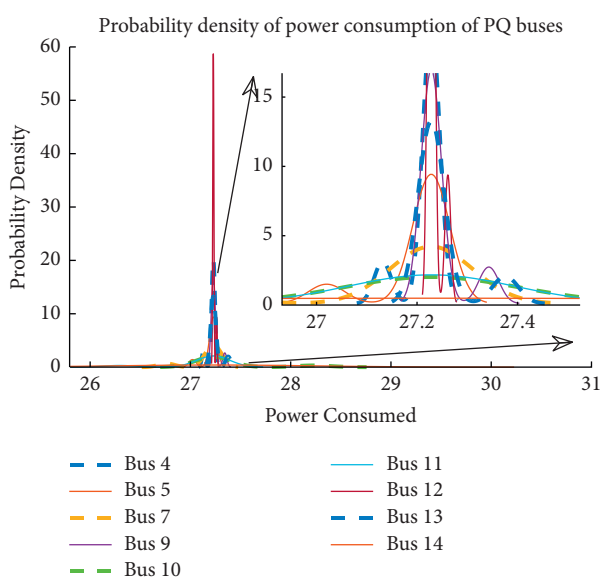

Figure 17: Power density distribution at buses 4, 5, 7, and 9–14.

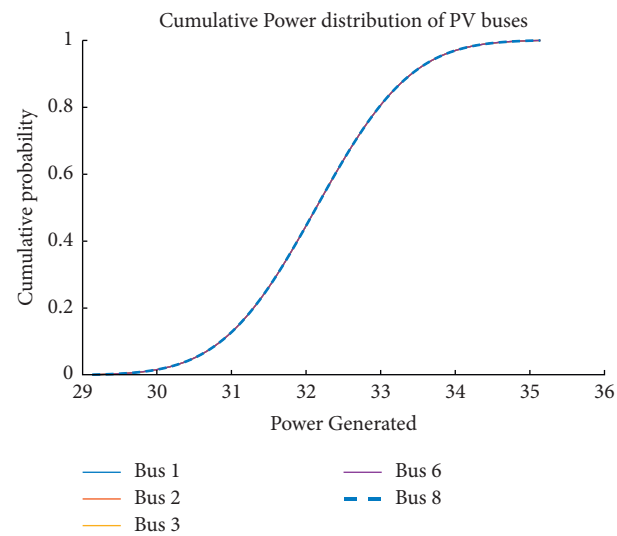

Figure 18: Cumulative power distribution at buses 1, 2, 3, 6, and 8.

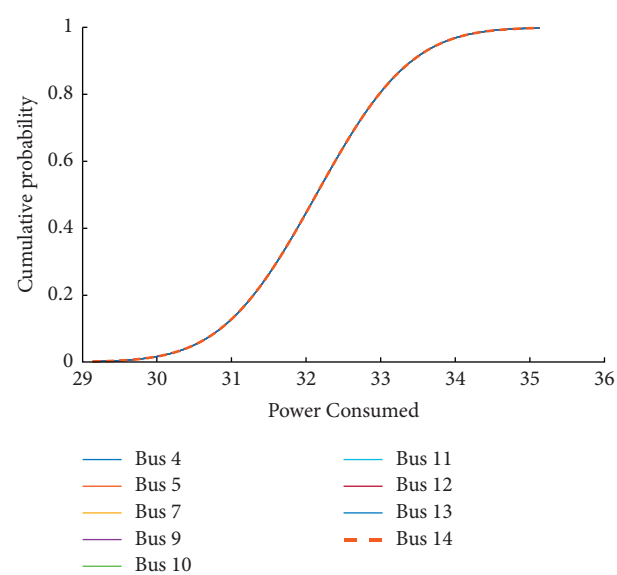

Figure 19: Cumulative power distribution at buses 4, 5, 7, and 9–14.

shown in Figures 12 and 13. Figure 12 shows the slack and generator buses, and Figure 13 shows for load buses.

The commutative power distribution for PV and PQ buses (buses 1–14) before load shedding for the IEEE-14 bus system is shown in Figures 14 and 15.

For the IEEE 14-Bus system without load shedding, the total power generated was found to be 383.0761 MW compared to the base power generation of 35.6310 MW. While total power consumed was found to be 1.9295 MW compared to base power consumed at 2.6922 MW. The weights $a = 1/14$ and $b = 1/11$.

Therefore $L_S = 28.32$, $P_G = 10.75$, and RI = 3.34.

The power density distributions at buses before load shedding for the IEEE-14 bus system are shown in Figures 16 and 17. Figure 16 shows the slack and generator buses, and Figure 17 shows for load buses.

For the IEEE 14-Bus system with load shedding, the total power generated was found to be 383.0761 MW compared to the base power generation of 35.6310 MW. While total power consumed was found to be 1.9295 MW compared to base power consumed at 2.6922 MW. The weights $a = 1/14$ and $b = 1/10$.

Therefore $L_S = 28.32$, $P_G = 10.75$, and RI = 3.59.

The commutative power distribution for PV and PQ buses (buses 1–14) after load shedding for the IEEE-14 bus system is shown in Figures 18 and 19.

The power density distributions at buses after load shedding for the IEEE-14 bus system are shown in Figures 20 and 21. Figure 20 shows the slack and generator buses, and Figure 21 shows for load buses.

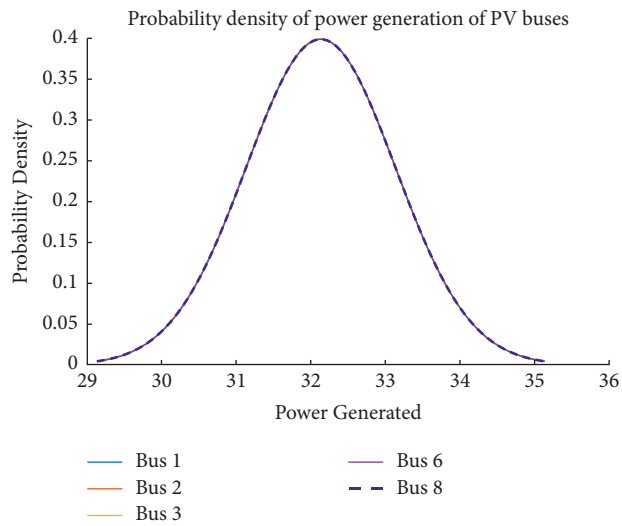

Figure 20: Power density distribution at buses 1, 2, 3, 6, and 8.

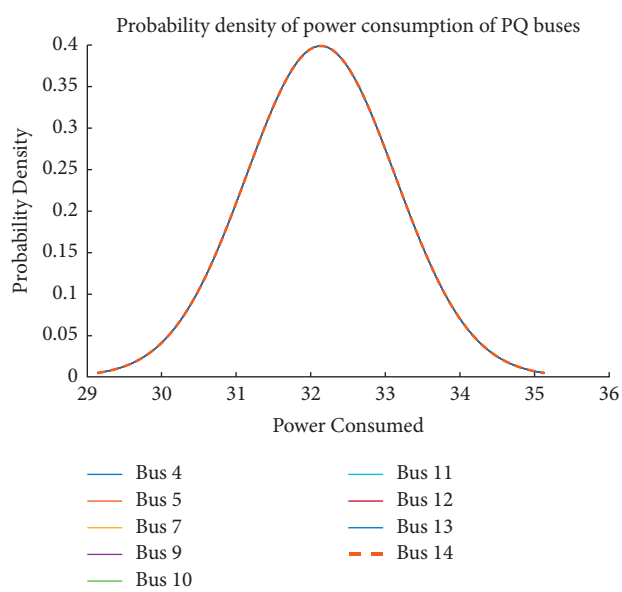

Figure 21: Power density distribution at buses 4, 5, 7, and 9–14.

The comparison between the resilience indices of the systems shows a rise in resilience due to load shedding.

4. Conclusion

The Monte Carlo simulation for the IEEE 5-Bus and IEEE 14-Bus systems, both with and without load shedding, is simulated, and the results are analyzed. The resilience index of both systems reveals that load shedding increases the resilience of the system, as evident from the rate of increase in resilience in each system due to load shedding. The increase in radial lines also causes the simulation to have a higher chance of failure to converge in an NR load flow solution introducing several Not a Number (NaNs) errors. The analysis of the results also reveals that the resilience of a smaller microgrid is larger than the resilience of a larger microgrid. It is also determined that after a certain number of iterations, an increase in the number of iterations does not influence the results of resilience analysis. The open challenge in microgrid resilience is to improve it, and one place to start is by evaluating all possible risks and potential impacts of man-made and natural hazards on the electricity system.

Abbreviations

abrATPG: Average total power generated
ATPC: Average total power consumed
PG: Power generation
LS: Load shedding
pfc: Probability of failure of conductor.

Data Availability

No data were used to support this study.

Conflicts of Interest

The authors declare that they have no conflicts of interest.

References

[1] M. Panteli, C. Pickering, S. Wilkinson, R. Dawson, and P. Mancarella, "Power system resilience to extreme weather: fragility modelling probabilistic impact assessment and adaptation measures," *IEEE Transactions on Power Systems*, vol. 32, no. 5, 2016.

[2] M. Panteli, D. N. Trakas, P. Mancarella, and N. D. Hatziargyriou, "Boosting the power grid resilience to extreme weather events using defensive islanding," *IEEE Transactions on Smart Grid*, vol. 7, p. 6, 2016.

[3] J. Najafi, A. Peiravi, and J. M. Guerrero, "Power distribution system improvement planning under hurricanes based on a new resilience index," *Sustainable Cities and Society*, vol. 39, pp. 592–604, 2018.

[4] H. Gao, Y. Chen, Y. Xu, and C. C. Liu, "Resilience-oriented critical load restoration using microgrids in distribution systems," *IEEE Transactions on Smart Grid*, vol. 7, pp. 2837–2848, 2016.

[5] Y. Xu, C. C. Liu, K. P. Schneider, F. K. Tuffner, and D. T. Ton, "Microgrids for service restoration to critical load in a resilient distribution system," *IEEE Transactions on Smart Grid*, vol. 9, pp. 426–437, 2018.

[6] S. Ma, B. Chen, and Z. Wang, "Resilience enhancement strategy for distribution systems under extreme weather events," *IEEE Transactions on Smart Grid*, vol. 9, pp. 1442–1451, 2018.

[7] H. Farzin, M. Fotuhi-Firuzabad, and M. Moeini-Aghtaie, "Enhancing power system resilience through hierarchical outage management in multi-microgrids," *IEEE Transactions on Smart Grid*, vol. 7, pp. 2869–2879, 2016.

[8] P. Bajpai, S. Chanda, and A. K. Srivastava, "A novel metric to quantify and enable resilient distribution system using Graph theory and Choquet integral," *IEEE Transactions on Smart Grid*, vol. 9, pp. 2918–2929, 2018.

[9] B. Li, R. Roche, and A. Miraoui, "A temporal-spatial natural disaster model for power system resilience improvement

using DG and lines hardening," in *IEEE Conferences IEEE Manchester PowerTech*, Manchester, UK, June 2017.

[10] G. Huang, J. Wang, C. Chen, J. Qi, and C. Guo, "Integration of preventive and emergency responses for power grid resilience enhancement," *IEEE Transactions on Power Systems*, vol. 32, pp. 4451–4463, 2017.

[11] M. Zare-Bahramabadi, A. Abbaspour, M. Fotuhi-Firuzabad, and M. Moeini-Aghtaie, "Resilience-based framework for switch placement problem in power distribution systems," *IET Generation, Transmission & Distribution*, vol. 12, pp. 1223–1230, 2018.

[12] S. Mousavizadeh, M. R. Haghifam, and M. H. Shariatkhah, "A linear two-stage method for resiliency analysis in distribution systems considering renewable energy and demand response resources," *Applied Energy*, vol. 211, pp. 443–460, 2018.

[13] A. Gholami, T. Shekari, F. Aminifar, and M. Shahidehpour, "Microgrid scheduling with uncertainty: the quest for resilience," *IEEE Transactions on Smart Grid*, vol. 7, pp. 2849–2858, 2016.

[14] K. Eshghi, B. K. Johnson, and C. G. Rieger, "Metrics required for power system resilient operations and protection," in *Proceedings of the IEEE Conference*, Eire, PA, USA, October 2016.

[15] S. Chanda and A. K. Srivastava, "Defining and enabling resiliency of electric distribution systems with multiple microgrids," *IEEE Transactions on Smart Grid*, vol. 7, pp. 2859–2868, 2016.

[16] M. Panteli, P. Mancarella, D. N. Trakas, E. Kyriakides, and N. D. Hatziargyriou, "Metrics and quantification of operational and infrastructure resilience in power systems," *IEEE Transactions on Power Systems*, vol. 32, pp. 4732–4742, 2017.

[17] M. Panteli, D. N. Trakas, P. Mancarella, and N. D. Hatziargyriou, "Power systems resilience assessment: hardening and smart operational enhancement strategies," *Proceedings of the IEEE*, vol. 105, pp. 1202–1213, 2017.

[18] Y. Xu, C. Liu, Z. Wang et al., ""DGs for service restoration to critical loads in a secondary network"," *IEEE Transactions on Smart Grid*99 pages, 2018.

[19] A. Singaravelan and M. Kowsalya, "A fuzzy-based approach for microgrids islanded operation," in *Proceedings of the IEEE Conferences 2013 International Conference on Energy Efficient Technologies for Sustainability*, Nagercoil, India, April 2013.

[20] N. Nikmehr, S. Najafi-Ravadanegh, and A. Khodaei, "Probabilistic optimal scheduling of networked microgrids considering time-based demand response programs under uncertainty," *Applied Energy*, vol. 198, pp. 267–279, 2017.

[21] B. Chen, C. Chen, J. Wang, and K. L. Butler-Purry, "Sequential service restoration for unbalanced distribution systems and microgrids," *IEEE Transactions on Power Systems*, vol. 33, pp. 1507–1520, 2018.

[22] H. Ji, C. Wang, P. Li, G. Song, and J. Wu, "SOP-based islanding partition method of active distribution networks considering the characteristics of DG, energy storage system and load," *Energy*, vol. 155, pp. 312–325, 2018.

[23] S. Chanda, A. K. Srivastava, M. U. Mohanpurkar, and R. Hovsapian, "Quantifying power distribution system resiliency using code based metric," *IEEE Transactions on Industry Applications*, vol. 54, pp. 3676–3686, 2018.

[24] C. Chen, J. Wang, F. Qiu, and D. Zhao, "Resilient distribution system by microgrids formation after natural disasters," *IEEE Transactions on Smart Grid*, vol. 7, pp. 958–966, 2016.

[25] M. Panteli and P. Mancarella, "Modeling and evaluating the resilience of critical electrical power infrastructure to extreme weather events," *IEEE Systems Journal*, vol. 11, pp. 1733–1742, 2017.

[26] A. Gholami and F. Aminifar, "A hierarchical response-based approach to the load restoration problem," *IEEE Transactions on Smart Grid*, vol. 8, pp. 1700–1709, 2017.

[27] D. A. Reed, K. C. Kapur, and R. D. Christie, "Methodology for assessing the resilience of networked infrastructure," *IEEE Systems Journal*, vol. 3, pp. 174–180, 2009.

[28] A. Arab, A. Khodaei, S. K. Khator, and Z. Han, "Electric power grid restoration considering disaster economics," *IEEE Access*, vol. 4, 2016.

[29] P. Eder-Neuhauser, T. Zseby, and J. Fabini, "Security: resilience and security: a qualitative survey of urban smart grid architectures," *IEEE Access*, vol. 4, pp. 839–848, 2016.

[30] R. Eskandarpour and A. Khodaei, "Machine learning based power grid outage prediction in response to extreme events," *IEEE Transactions on Power Systems*, vol. 32, pp. 3315-3316, 2017.

[31] L. Liang, Y. Hou, D. J. Hill, and S. Y. R. Hui, "Enhancing resilience of microgrids with electric Springs," *IEEE Transactions on Smart Grid*, vol. 9, p. 1, 2016.

[32] Y. Liu, Q. H. Wu, and X. X. Zhou, "Coordinated multiloop switching control of DFIG for resilience enhancement of wind power penetrated power systems," *IEEE Transactions on Sustainable Energy*, vol. 7, pp. 1089–1099, 2016.

[33] X. Liu, M. Shahidehpour, Z. Li et al., "Microgrids for enhancing the power grid resilience in extreme conditions," *IEEE Transactions on Smart Grid*, vol. 8, no. 2, pp. 589–597, 2016.

[34] S. Mishra, K. Anderson, B. Miller, K. Boyer, and A. Warren, "Microgrid resilience: a holistic approach for assessing threats, identifying vulnerabilities, and designing corresponding mitigation strategies," *Applied Energy*, vol. 264, Article ID 114726, 2020.

[35] J. Duan, H. Li, X. Zhang et al., "A deep reinforcement learning based approach for optimal active power dispatch," in *Proceedings of the 2019 IEEE Sustainable Power and Energy Conference (iSPEC)*, pp. 263–267, Beijing, China, November 2019.

[36] A. Ali, K. Mahmoud, and M. Lehtonen, "Optimal planning of inverter-based renewable energy sources towards autonomous microgrids accommodating electric vehicle charging stations," *IET Generation, Transmission & Distribution*, vol. 16, no. 2, pp. 219–232, 2022.

[37] A. Ali, K. Mahmoud, and M. Lehtonen, "Optimization of photovoltaic and wind generation systems for autonomous microgrids with PEV-parking lots," *IEEE Systems Journal*, vol. 16, no. 2, pp. 3260–3271, 2022.

[38] A. Ali, K. Mahmoud, and M. Lehtonen, "Multiobjective photovoltaic sizing with diverse inverter control schemes in distribution systems hosting EVs," *IEEE Transactions on Industrial Informatics*, vol. 17, no. 9, pp. 5982–5992, 2021.

Hindawi
Journal of Electrical and Computer Engineering
Volume 2022, Article ID 7001448, 12 pages
https://doi.org/10.1155/2022/7001448

Research Article

Designing of Neuro-Fuzzy Controllers for Brushless DC Motor Drives Operating with Multiswitch Three-Phase Topology

Ch. Vinay Kumar,[1] G. Madhusudhana Rao,[2] A. Raghu Ram,[3] and Y. Prasanna Kumar[4]

[1]*MGIT, Hyderabad, India*
[2]*OP Jindal Univesity, Raigarh, India*
[3]*JNTUCEH, Hyderabad, India*
[4]*Bule Hora University, Oromia, Ethiopia*

Correspondence should be addressed to G. Madhusudhana Rao; gmrgurrala@gmail.com and Y. Prasanna Kumar; prasannaky@gmail.com

Received 2 May 2022; Revised 24 May 2022; Accepted 30 May 2022; Published 20 July 2022

Academic Editor: Ton D. Do

Brushless DC motors are simple in construction, high efficiency, less noise, and high reliability, which are not replaceable motors in specific applications compared to other motor drives. It has a facility for its multivariable system, nonlinear control process, and powerful coupling system. This paper proposes to design the neuro-fuzzy controllers for its multiple converters switching to improve the power factor and minimize the BLDC motor switching losses. Compared with conventional controllers, this controller will develop the power factor and optimize the current ripples concerning time and torque. The working model of the BLDC motor may be presented here. A nonlinear load will be applied to the BLDC motor to determine the speed, current, and torque. The multiple switches designed with the proposed controllers are connected with the converter's DC link to boost the voltage. The fuzzy logic controller is implanted to adjust the speed of the neural network and is also designed for the analysis of the stability of the system. The proposed controllers compare the rate at different speeds, torque, currents, and rotor angle positions. Finally, the proposed controller for multiple converter switches performs better than the conventional controllers.

1. Introduction

In recent years, brushless DC motors have become more popular and valuable in industries due to their highly reliable power density and ease of handling. The converter circuit will be used to control the brushless DC motor in three-phase systems. The rotor position sensor will be used for the start and a suitable communication pattern to operate the bridge circuit so that the power devices are commutated for every 60°. To meet the requirement of the efficiency and performance of the BLDC motor requires properly suitable speed controllers. In conventional motors, speed control is achieved by the PI controllers due to their simple construction and implementation in an industrial application. But when the motor is connected to a nonlinear type of load, the motor parameters are altered, the disturbances will occur that cannot easily control the speed of the motor.

Furthermore, the conventional controllers need exact mathematical models to find the speed response and steady-state error, and power factor enhancement of the BLDC motor, which is not for many sufficient controllers. Due to overcoming these disadvantages of the PI controllers, artificial intelligence controllers like fuzzy logic, neural network, and adaptive neuro-fuzzy controllers may be implemented to control the speed of the BLDC motor effectively. The converter is used with the five-level switches in this proposed paper. In maintaining the speed of the BLDC motor, it is necessary to design the ANFIS controllers to achieve the best performance and efficiency [1]. Different computing

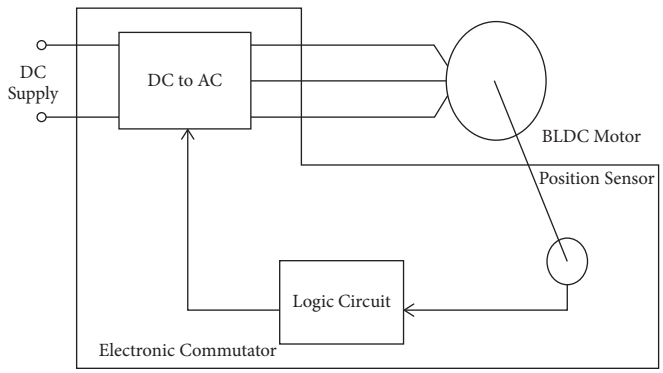

Figure 1: Constructional features of the BLDCM.

methods are available to approach the requirement to solve the current difficulties in controlling the speed of brushless DC motors. In this paper, a new novel soft computing method is applied to overcome the problems like current distortions and voltage issues of the brushless DC motor using the neuro-fuzzy logic controllers to compare the PID controllers. In neural networks, the inputs are well trained and tested, showing the helpfulness of the controller and governing the speed and steady-state errors, etc. Tuning the PID controllers with the proposed controllers has improved performance and caused higher efficiency than the PID controllers [1]. The three-phase converter circuit will be used to control the brushless DC motor. It needs the rotor position sensor for the controlling process of the converter to obtain suitable swathing conditions, which will minimize the switching losses.

In general, the Hall sensors will be used to evaluate the revolving position of the rotor by specific parameters applied to the positioning of the sensor using well-developed sensor technologies [2, 3]. These sensor positions are electrically driven every phase by 1200, divided into 60° for every step. One instant at a time, only two phases will be carried out. This phenomenon will be shown in Figure 1. From Figure 1, we can understand the brushless DC motor model and its performance with the elements of the motor. The simulation of the equivalent and operational circuit of the brushless DC Motor is shown in Figure 2. The speed sensor is coupled with the brushless DC motor with the three-phase converter to maintain the current, providing the BLDC motor to adjust the current. This sensor produces the control signal to evaluate the PWM, which activates the converter drivers. The Hall sensors will be working to converter circuit drive for the essential switching stage. These crucial stages of the switches will allow the normal condition of the three-phase converter to prevent the short circuit in any of the three legs or three lines. The brushless DC motor flux distribution and EMF waveforms are generally similar to the trapezoidal one. When the BLDC motor is operated in self-controlled mode, the EMF waveforms are similarly sinusoidal, so the BLDC motor is called the sinusoidal BLDC motor.

So the sinusoidal BLDC motor and trapezoidal BLDC motor are very similar. In these two cases, the rotor position must be synchronized then the motor currents may be controlled. Though there are constructional differences

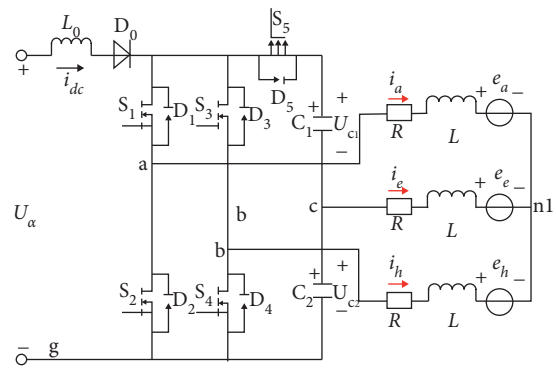

Figure 2: Equivalent and operational circuit of the BLDC motor.

between the synchronous motor and trapezoidal BLDC motor, the excitation of the current is different in both machines. The BLDC motor's current is excited by the square wave or quasi-wave currents. The Hall sensor devices detect the rotor EMF and evaluate the phase switching points of the trapezoidal BLDC motor. The sinusoidal BLDC machine needs the sequence of the exact position of the rotor, and then it will allow the correct combination of the sinusoidal waveforms. Therefore, the BLDC motor has a significant role in designing factors over the standard DC motor. The shaft position of the sensor system is modest and essential only to allocate the number of signals for imposing the transistor of the converter. The quasi-square armature currents will directly control machine torque by their maximum amplitude value. The natural dead time for every transistor is most reliable to improve the performance of the converter in the BLDC motor. The synchronization process is allowed to operate the machine, and it required the first and third characteristics which will minimize the complexity in the circuit of the machine circuit [4], but the second characteristics will allow the circuit which will design for the DC machine for controlling the trapezoidal current $I_{\max}$.

This proposed paper uses the neuro-fuzzy controllers for this BLDC motor to control its speed and minimize the current distortions. The fuzzy logic will be used for time optimization, and the neural network will be implemented to test and train the parameters. These two controllers are integrated and give the perfect result of the BLDC motor. The implementations of the fuzzy controllers will work

based on the rule base function with the IF-THEN rule, where it is easily understandable for the drive. In neural networks, the supervisory learning method will be used to overcome the drawbacks of backpropagation. This proposed controller is used for the estimation of the torque and speed of the BLDC motor drive. The operational capability of the deliberated controller is explained in detail in MATLAB/Simulink simulation results [5].

2. Modelling of the BLDC Motor

In the BLDC machine, the stator winding is concentrated. Hence, the stator waveform will be trapezoidal, whereas in PMSM, the stator winding is distributed winding. Hence, the stator waveform is sinusoidal. As far as the rotor is concerned, both are permanent magnets. It is also comparable to constructing an AC motor with the BLDC motor. The constructional features of the brushless DC motor are shown in Figure 1. Majorly, the stator windings are similar to the three-phase induction motor, and several permanent magnets are placed in the rotor. The main dissimilarity between the AC motor and the BLDC motor is that the location of the rotor of the BLDC motor produces the signal to control the switching operation of the switches. The Hall sensor is the main common element in the DC motors, but some other special DC motors use optical sensors [6].

According to the six states, the brushless DC motor will work according to the working principle. Two phases will be active in each state as per the operating principle. The generalized conceptual waveforms of the back EMF of the BLDCM are characterized in Figure 3 [3]. The developed model of the brushless DC motor comprises the back EMF and phase inductance of the rotor. e_{MAX} is the maximum error that will be evaluated based on the inclines of m_1 and m_2 at the functioning of the carrier frequency. This phenomenon is described in the following mathematical equations:

$$|m_1| = \frac{E_{pp}}{xT} = \frac{E_{pp}.f}{X}, \tag{1}$$

$$|m_2| = \frac{E_{pp}}{(1-x)T} = \frac{E_{pp}.f}{1-X}, \tag{2}$$

where

$$x = \frac{|m_2|}{|m_1| + |m_2|}, \tag{3}$$

$$E_{pp} = \frac{1}{f}\left(\frac{|m_1| * |m_2|}{|m_1| + |m_2|}\right). \tag{4}$$

In the case of incremental in current, the term "x" in the above equation (3) denotes the carrier "T" period. From equation (4), "x" describes a model production of the pulse width modulation design. So the regulating constraints must be familiar with "x." Finally, E_{PP} characterizes the maximum error signal.

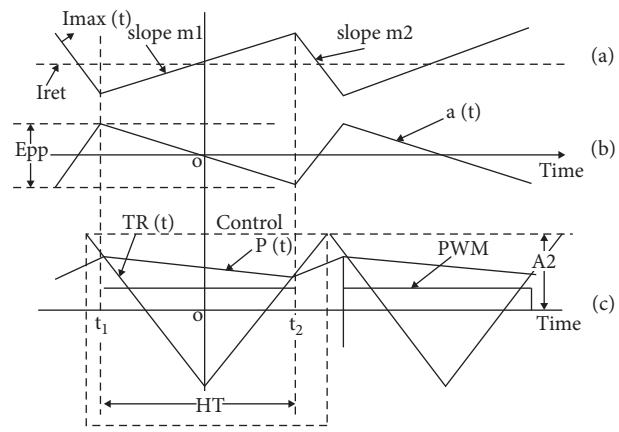

Figure 3: Generalized graphical representation of (a) feedback signal I_{MAX}, (b) error signal $e(t)$, and (c) control signals [D_1] [7].

The constructional features of the three-phase BLDC motor are as shown in Figure 3, similar to the permanent magnet synchronous motor [7]. In this construction of the BLDC motor, it is observed that the stator windings are the same as the AC motor, and the rotor is designed with permanent magnets. But the BLDC motor differs in rotor position to generate the control signal in electronic circuit switches. The Hall sensor is used to control the rotor position by using switches. The BLDC motor will be working with the six-state principle, and each state will be working with the concept of the two-phase principle [3]. Figure 3 clarifies the commutation process in the BLDC motor according to the working idea of the rotor position.

Figure 2 shows that the brushless DC motor uses the direction of the Hall sensor to make the commutation process per the rotor position. The MOSFET is designed in the converter circuit. It will conduct the conduction process and generate the EMF in three phases A, B, and C of the brushless DC motor. The commutation process will follow as per the rotor position. The three-phase currents will be commutated at every 60° electrically in BLDC motors. These commutating signals will be identified and received by the hall sensors of the rotor system. However, the signals will be divided into six modes of operation as per the switching pattern in the converter circuit, and each of the two switches will act at one time in a two-phase system, and the other one is off-mode. From Figure 2, it is analyzed that the proposed algorithm and conventional topology designed the BLDC motor drive system is presented here. The figure consists of three-phase currents i_a, i_b, i_c; back EMF of each phase e_a, e_b, e_c; resistance R (r_a, r_b, r_c), inductance L (L_a, L_b, L_c) of each phase, i_{dc} is the DC-link current, "n" is the ground point to the winding of the stator of the designed BLDC motor drive system. The DC-link is a capacitor directly connected with the ground terminal from phase C. The red-coloured arrow marks show the direction of the three-phase currents. Using the neuro-fuzzy controllers, the voltage must be enhanced between the capacitors C_1 and C_2 with the proposed new technology. It causes the consumption of the supply voltage, which must be increased in case of the low supply voltage. The inductance L_0 will store the energy and boost when the

drive system's vector system is working. The switches will be turned-on alternatively with a continuous process of the proposed topology. During this process, the storage of energy by the inductance L_0 will be given to the capacitors to increase the voltage when the switches are in the turn-off position. But the diode D_0 will block the reverse energy, then it may flow DC-link to the power supply to switch on the other switch 1. In this way, the designed BLDC motor drive system will work with the proposed new technology.

The typical mathematical equations of the BLDC motor are described due to their similarity in its phases, that is,

$$r_a = r_b = r_c = r_m, L_a = L_b = L_c = L_m. \tag{5}$$

The BLDCM designed in the following equations:

$$\begin{bmatrix} u_a \\ u_b \\ u_c \end{bmatrix} = \begin{bmatrix} \mathbf{R} & 0 & 0 \\ 0 & R & 0 \\ 0 & 0 & R \end{bmatrix} \mathbf{X} \begin{bmatrix} i_a \\ i_b \\ i_c \end{bmatrix} + \begin{bmatrix} L_m - M & 0 & 0 \\ 0 & L_m - M & 0 \\ 0 & 0 & L_m - M \end{bmatrix} \frac{d}{dt} \begin{bmatrix} i_a \\ i_b \\ i_c \end{bmatrix} + \begin{bmatrix} e_a \\ e_b \\ e_c \end{bmatrix}. \tag{6}$$

The above equation states that r_m, L_m, and M are the stator resistance, inductance, and mutual inductances, and u_x, e_x, and i_x, are the phase voltage, back EMF, and phase current of the stator [8]. Finally, the EMF torque is expressed as

$$T_e = \frac{Z_P}{2\omega_e}\left(e_a i_a + e_b i_b + e_c i_c\right). \tag{7}$$

From the above equation, ω is the speed of the rotor, and Z_p is the rotor's magnetic poles [9]. Therefore, the motor motion equation can be written as

$$T_e = T_L + J\frac{d\omega_r}{dt} + B\omega_r. \tag{8}$$

3. Neuro-Fuzzy Control Systems

There is a considerable development in the control systems by implementing artificial controllers to control the speed of the machines, which are majorly used like fuzzy logic controllers, neural network controllers, genetic algorithms, and expert systems. These controllers have a particular type of superiorities.

In designing the neuro-fuzzy controllers, the suitable controller is identified from the following explanation; the controller represents the rules at the first level of the approach. The controller's input is quantitative variables, giving the output in linguistic qualitative manner. Then it provides a detailed analysis of the plant and approximates its knowledge. This will work mainly in the following aspect [10]:

(i) Knowledge demonstration and inference are moderately straightforward.

(ii) Rugged construction and operation.

The fuzzy logic controller is the crispy set invented by Lofty Zadeth in 1965. The crisp set is also called the universal set. Takagi and Sugeno proposed the modified fuzzy membership function based on IF-THEN rules which can be applied to the linear equations. The fuzzy logic membership functions are shown in Figure 4, and the error analysis of the fuzzy logic controller is shown in Figure 5.

The fuzzy output model expression will be written as

$$\begin{aligned} Y &= \frac{\sum_{i=1}^{N} w_i y_i}{\sum_{i=1}^{N} w_i} \\ &= \frac{\sum_{i=1}^{N} w\left(C_{i1} + C_{i1}T_1 + \ldots + C_{i1}T_n\right)}{\sum_{i=1}^{N} w_i} \\ &= \frac{\sum_{i=1}^{N} w_i y_i \sum_{i=1}^{N} wC_{ik}T_k}{\sum_{i=1}^{N} w_i}, \end{aligned} \tag{9}$$

where $x_0 = 1$, ω_i is the weight of the ith IF-THEN rule for the input and is calculated as

$$w_i = \prod_{k1}^{n} A_{ik}(xk), \tag{10}$$

where $A_{ik}(x_k)$ is the membership grade.

The fuzzy logic control method can be implemented in ambiguity or uncertainty systems. In the control process of the control system, the membership functions used are generally 10 and 1 in nonlinearity, load distortions, and parameter variation [7]. The neural network evaluation and data treating method simulate the procedure that starts in biological neurons. A neuron is a fundamental element, and the connection of two neurons may work like turned on, trained off, and combining both conditions.

The fuzzy logic controller is designed with the rule-based system. The original concept of the fuzzy logic systems is that they will provide the knowledge representation about the constant parameters. Figure 6 analyses the significant parts of the fuzzy logic [11, 12].

The following rule base is given for a modified T-S fuzzy model

$$\begin{aligned} &If\ X_1\ is\ A_{i1}, \ldots, X_n\ is\ A_{in}\ then\ y_i \\ &\quad = K_i\left(c_0 + c_1 x_1 + \ldots + c_{nx_n}\right), \end{aligned} \tag{11}$$

where $i = 1, 2, 3, \ldots, X_n$ and n are the numbers of IF-THEN rubrics. Therefore, the free parameters will be optimized to the next level. This simplified T-S fuzzy high predictive property model has effectively identified the nonlinear control systems [13]. Using the fuzzy rule foundation must be effectively embedded into the systems that deal with the issues. Progress has been made to systematically improve the fuzzy systems with the creative process [14]. The need to successfully modify the parameters and construct fuzzy

e/ce	NB	NM	NS	ZO	PS	PS	PB
NB	NB	NB	NB	NB	NM	NS	ZO
NM	NB	NB	NB	NM	NS	ZO	PS
NS	NB	NB	NM	NS	ZO	PS	PM
ZO	NB	NM	NS	ZO	PS	PM	PB
PS	NM	NS	ZO	PS	PM	PB	PB
PM	NS	ZO	PS	PM	PB	PB	PB
PB	ZO	PS	PM	PB	PB	PB	PB

Figure 4: Fuzzy logic membership functions.

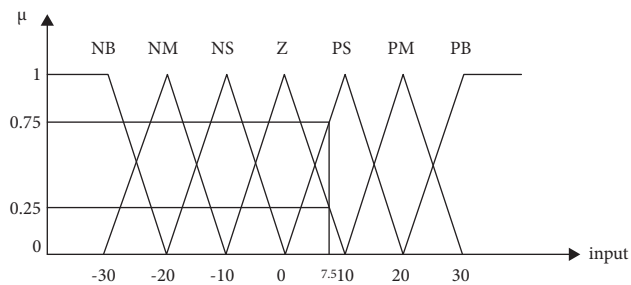

Figure 5: Fuzzy logic analysis of the error.

systems has caused these studies' growth. Many researchers use genetic algorithms, evolutionary programming, and other possible methods to identify the fuzzy logic to design the control parameters. However, the problem of dynamically separating the input space for each input and output variable, selecting the suitable fuzzy rules [15] for which resembling nonlinear systems are unknown, and atomizing the discrimination remains. T-S fuzzy modelling has been designed and developed to model the BLDCM. The speed error and current error of the motor are given to the fuzzy systems as inputs. The speed error can be determined by considering the armature current and the previous error of the armature current I_a. These two errors are fed to the fuzzy controller as per its designed sequence and converted into the linguistic set. Then the defuzzification process will be done. The error and change in "error" of functions are analyzed.

3.1. Pattern and Batch Training. To analyze the pattern mode example, get trained and then the weights are almost updated. Once each training sample is updated, the weights are updated in the epoch mode. The batch mode examples follow the error function's original vertical level, give an idea about it, and discover a set of weights corresponding to the minimum error functions. A sigmoid is used rather than a rugged preventive linear threshold unit. The sigmoid is differentiable, and there is a dissimilarity between an LTU and a sigmoid. The algorithm's calculations are accepted as single layer at one time in parallel. The following is the primary strategy for using the backpropagation algorithm: the desired activation will be [1, −1] rather than the standard [0, 1]. There is both theoretical and experimental evidence. The step size, p, is set to a little positive value. Even while a higher p number leads to faster convergence, this is only true up to a point. When the value of p is too large, the algorithm becomes unstable and fails to converge. As a result, this will be suggested that the rate of p should be kept high determined to 0.1. The starting optimized weights will be distributed casually. The consequences should be observed for a cell with z inputs between $[-2/z, 2/z]$.

(i) Forward propagation computes every cell's weighted sum, Si, and stimulation, $u_i = f(Si)$.

(ii) Backpropagation is completed from the output, and layers are one by one in form. The error correction rules adjust the synaptic weights in this development. From the above equation, the weights are updated

$$W_{ij}^{*} = W_{ij} + p\delta u_j, \tag{12}$$

AMS (approx mean square) error [16]

$$\begin{aligned} W_{ij}^{m}(\mathrm{k}+1) &= W_{ij}^{m}(k+1) - \alpha \frac{\partial \widehat{f}}{\partial w_{ij}^{m}}, \\ b_{j}^{m}(\mathrm{k}+1) &= b_{i}^{m}(k) - \alpha \frac{\partial \widehat{f}}{\partial w_{i}^{m}}. \end{aligned} \tag{13}$$

The biological neuron is the foundation of artificial neural networks science. The neuron's essential parts must grasp to comprehend the construction of artificial networks. Neurons are the basic building blocks of the central nervous system. Dendrites, cell bodies, and axons are the three primary components of a neuron. The dendrites receive signals from nearby neurons. The cell's dendrites deliver messages to the cell's body. The neuron nucleus is found in the cell body. When the neuron targets by sending an electrical signal beside the axon to the next neuron, the sum of the received signals exceeds a threshold value. The artificial neuron model is based on the human neuron's components, as shown in Figures 7 and 8. Dendrites are represented by the inputs X_0-X_3. The weights W_0-W_3 are multiplied by each input. From Figure 7, it is observed that Y is the output and F is the total summation of the inputs modelled neurons.

3.2. Design of Adaptive NFC. For designing NFC, we spot the controller from two spots explained in the following: in the first approach, the controller is depicted as a set of rules, which accepts the input in the form of qualitative variables and gives the output in the form of linguistic qualitative. The main advantages of such a system are as follows. Approximate knowledge about the plant is required, and an exact system model is not required. Knowledge representation and inference are easy. Implementation is easy. The fuzzy controller is one rule-based control system. One of the important advantages of using a fuzzy viewpoint is that the FL provides the best methods for knowledge depiction that could be devised for encoding knowledge about continuous variables. Figure 7 represents the model of a fuzzy system, which is composed of four major parts.

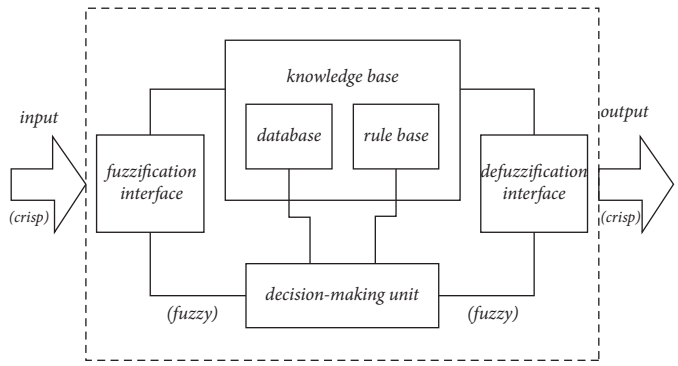

Figure 6: The general model of a fuzzy system.

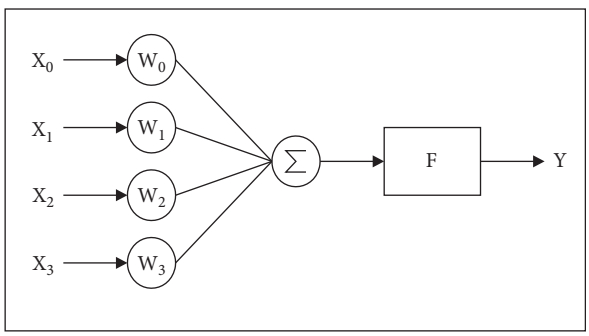

Figure 7: Neuro-fuzzy network structure [13].

Figure 5 shows the membership function of error and derivative of error between the output and reference of the controller used in this paper. "a" for this application is 0.5. The fuzzy inference table is shown in Figure 4. The second approach depicts the controller as a nonlinear map among the inputs and outputs. Depending on a specific plant, the map (in the form of a network) can be trained to implement any control plan. NNs, with their massive parallelism and ability to learn any nonlinearity, are used to address some of the practical control problems. An NN-based control system performs a particular form of adaptive control, with the controller taking the form of a multilayer network. The adjustable parameters are defined as the adaptable weights.

4. Learning in Adaptive NFC

The controller has to design as per the human's mimic actions in a few specific conditions. This design is based on the learning algorithm called the supervised learning algorithm for a system to be controlled. An artificial neural network is the best controller to control the system with the help of a supervised learning algorithm. The suitable learning algorithm will be used from the neural networks forward model. Nevertheless, in this case, the network input information is obtained from the human through the senor working principle. Then the output will be controlled by the human's input. The artificial-based supervisory learning algorithm that has been developed for the BLDC motor is shown in Figure 9. Figure 10 clarifies the block diagram of the supervisory algorithm of artificial neural networks to the BLDC motor. The error backpropagation (EBP) algorithm is a simple and easily understandable algorithm for neural network training [15]. Therefore, the controller will accept the output error in the system by using the EBP algorithm. Nevertheless, this method suffers from noise sensitivity and harmonics distortion, which will have a minimum effect on the system [12].

At least one supervisor should be connected to the EBP algorithm to improve the learning algorithm capacity and repeat its accurate, high-performance operation near the exact value. System performance may improve in this process, and the network weights are updated based on the input value. Figure 11 gives information about the supervised algorithm using the NFC controller, which will find the error between the supervisor input and plant output designed and developed in MATLAB/Simulink [12].

The development of the control strategy for speed control of the BLDC motor with the proposed ANFIS controller is presented in Figure 2. It consists of two loops: an inner loop and an outer loop. The inner loop synchronizes the inverting gate signal with the motor's back electromotive force or rotor position. The outer loop controls the speed of the BLDC motor by controlling the DC bus voltage through the PWM inverter. Based on the error and the rate of change of error, the BLDC motor drive system is designed and developed in the MATLAB; as shown in Figure 12, and the ANFIS controller provides the control signal to the switching logic circuit. The switching logic circuit provides the PWM signal for the inverter gate concerning the rotor position of the motor and the control signal output obtained from the ANFIS controller [18].

When the converter circuit is connected among the motor drive and load, the capacitor DC-link gets discharged within a short period. The execution of neuro-fuzzy controllers with the adapted torque control is shown in Figure 13. As a result, the currents are in peak value, which causes accruing spikes from the supply to the load side. These spikes will weaken the performance of the power factor and the overall system performance. However, the converters will maintain a good power factor using the VSI-designed converters. Figure 14(a) shows the phase voltage waveforms based on the rotor position at 900 rpm. The phase difference between a, V_b, and V_c is approximately 120°, and

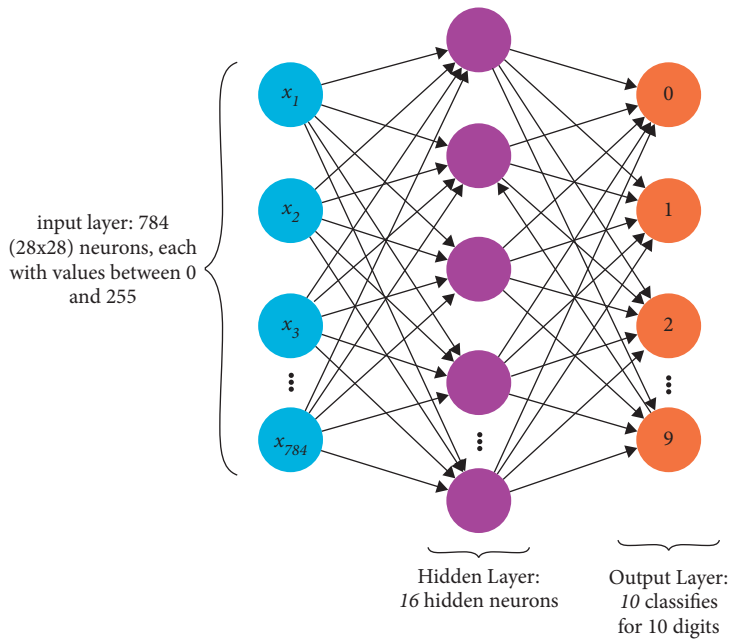

Figure 8: Multilayered artificial neural networks [13].

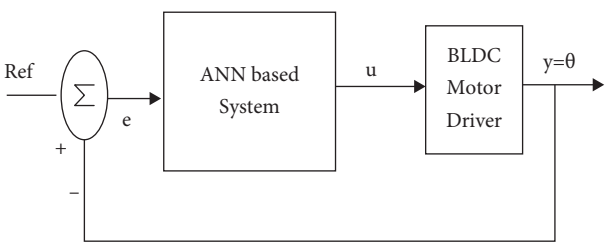

Figure 9: Supervisory control algorithm for the system.

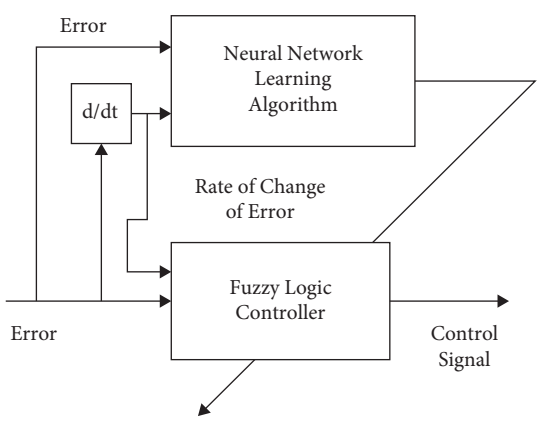

Figure 10: Block diagram of the supervisory controller of the system.

this result is designed with the artificial neural networks, and is also compared with Figure 14(b) which is designed with ANFIS controllers. The DC voltage of the BLDC motor is same in both cases of ANN and ANFIS, but the difference is in the power factor where it is lagging in ANFIS compared to ANN.

Furthermore, the above figure shows that the system has better source efficiency and minimized peak current levels, which causes the overall approach's cost to be minimized [16]. As the results show, the electromagnetic field of the BLDC motor for each phase is shown in Figure 15. It is observed the electromagnetic field is almost stable after 5 sec. The rotor of the BLDC motor and the permanent-magnet rotor follow the stator rotating magnetic field up to its equality, as shown in Figure 16. When the EMF is equal between rotor EMF and stator EMF, the motor produces the negligible harmonics shown in Figure 17.

As most applications demand, the drive must perform under varying load conditions. Therefore, to ascertain the superior performance of the proposed ANFIS controller, simulation results have also been obtained for varying load conditions. When the BLDC motor is running with load, the torque characteristics are shown in Figure 18. From Table 1 the minimum of load torque will be considered 0.7 Nm for the motor which is running at 700–900 rpm shown in Table 2, and it is observed that the reference torques and BLDC motor torque is uniform upper and lower limits from 1.3 Nm to 3.2 Nm. First, the load torque decreases from 3.2 Nm to 1.3 Nm and increases from 3.2 Nm to 3.5 Nm. The BLDC motor drive suffers from electromagnetic torque distortions due to the armature currents. The armature currents are generated during the armature windings' six-step switching conditions, which produces the harmonics. Here the electromagnetic toque decreases the harmonics with the proposed controllers by 1.0 to 1.3% using the mutual compensation of the magnetic winding sets within the switching angle of 60° electrical. In the air gap of

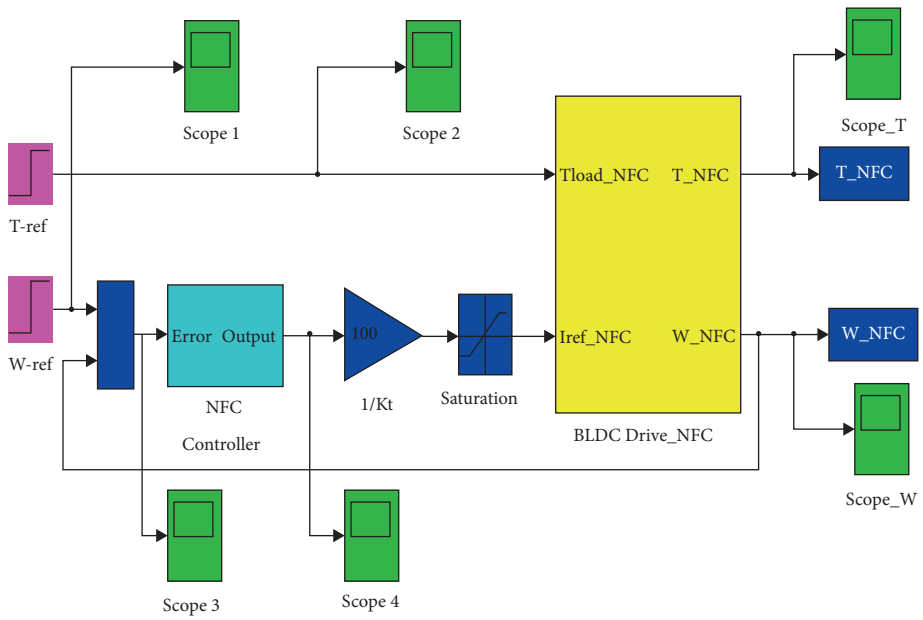

Figure 11: Block diagram of the system in Simulink [17].

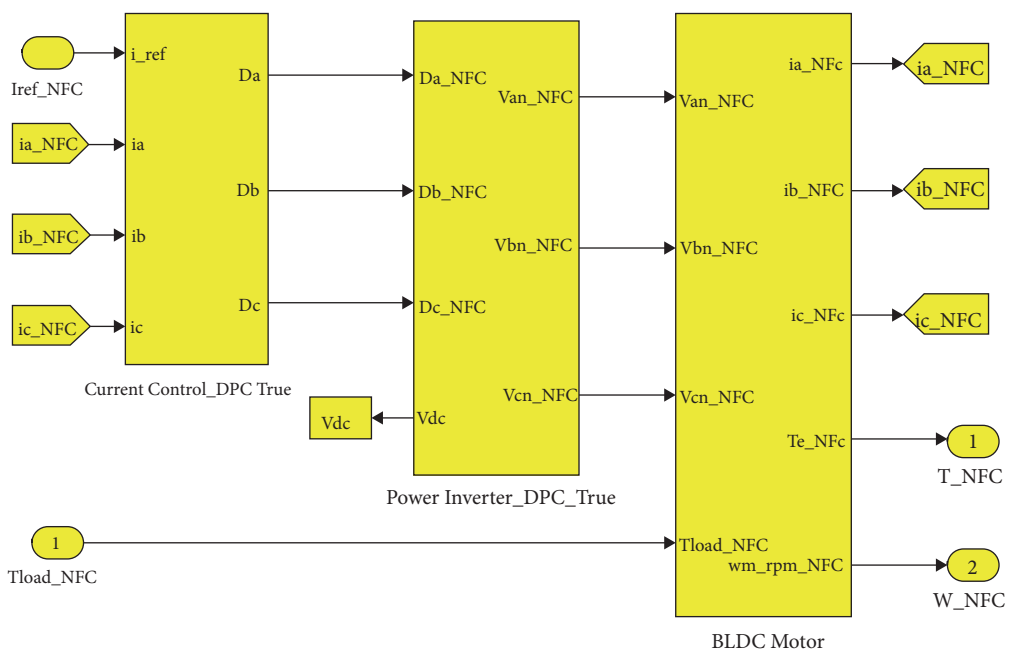

Figure 12: BLDC motor drive in Simulink [17].

the BLDC motor, the stator of will produces the stationary magnetic flux in the motor air gap. Figures 17(a) and 17(b) give information about the rotation of the rotor in this field that induces ac currents in its windings. The frequency of these currents decreases with rotor speed to set up a stationary magnetic field concerning the stator. The interaction of the two fields creates a braking torque whose magnitude depends on the dc field generated by the stator, the rotor resistance, and the speed of the rotor.

Figure 19 shows the active power and speed of the BLDC motor. Furthermore, the reference and BLDC motor speeds are compared with their desired values and implemented with the artificial neural networks. Finally, the torque of the BLDC motor is reached with its reference toque in Figure 19(c).

Figure 20 clarifies the improvement of the BLDC motor speed and torque, which is designed with the ANFIS controllers compared to the ANN controller. In optimizing the

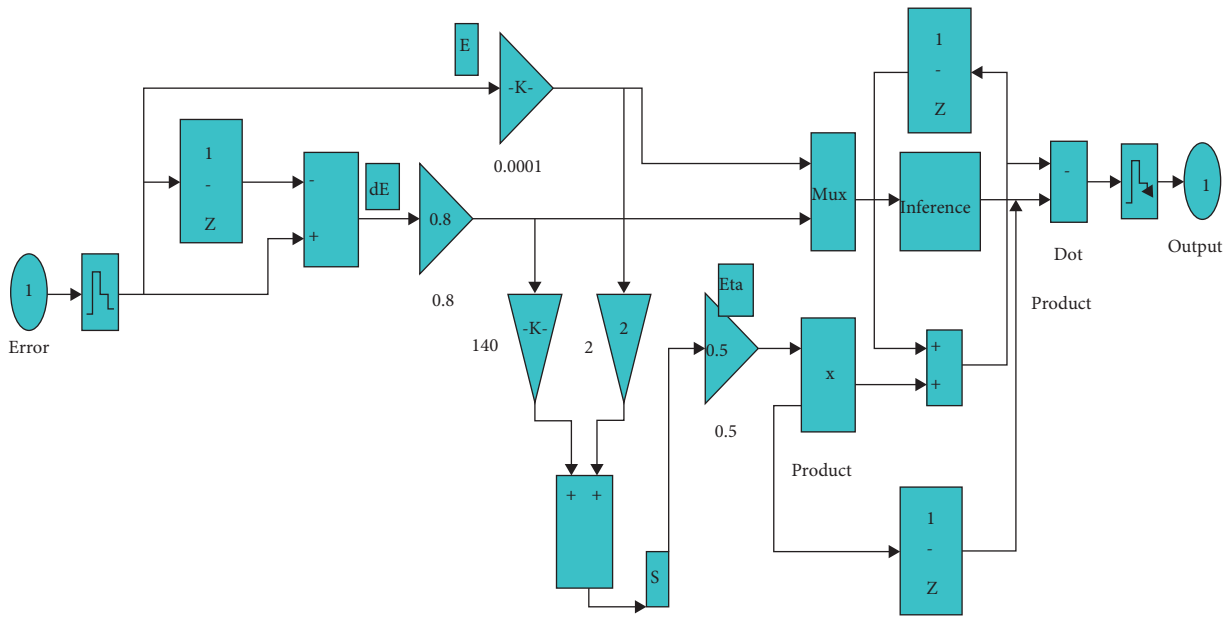

Figure 13: Execution of neuro-fuzzy controllers with the adapted torque control [17].

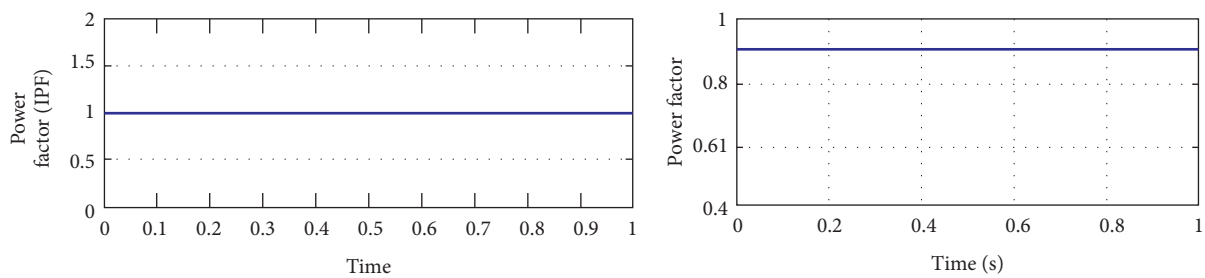

(a) (b)

Figure 14: (a) ANN designed power factor. (b) ANFIS designed power factor.

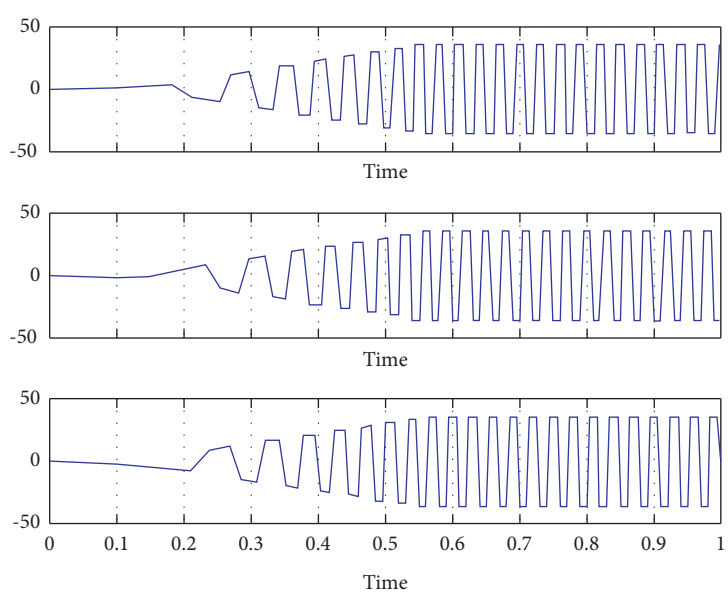

Figure 15: Stator back EMF e_a, e_b, and e_c of the BLDC motor.

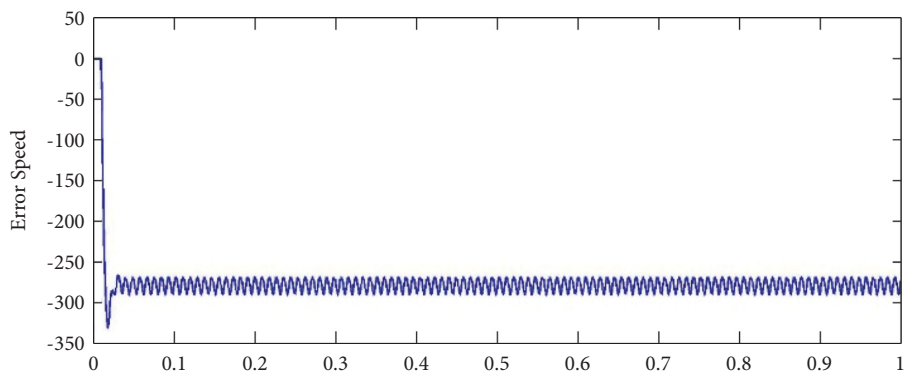

Figure 16: Rotor speed of BLDC motor.

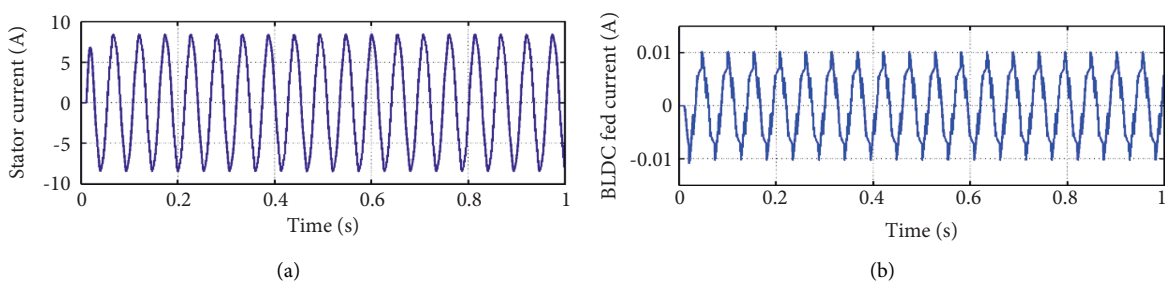

Figure 17: (a, b) Stator currents of BLDC motor.

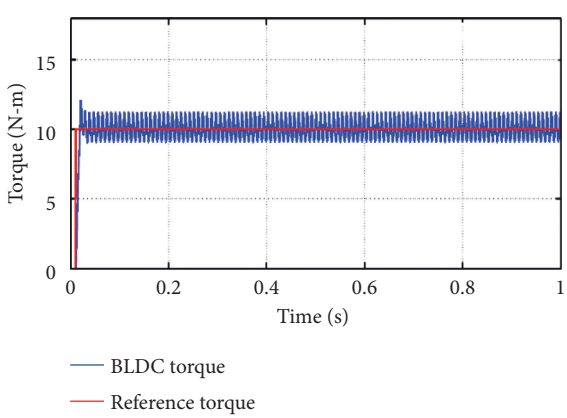

Figure 18: Electromagnetic torque T_E of the BLDC motor.

Table 1: Parameters of the BLDCM.

Parameter	Value
VDC	210 V
Flux linkages constant	0.107 [wb]
Self-inductance	2.72 mH
Mutual inductance	1.5 mH
Moment of inertia	0.000310 kg-m/sec^2
Resistance/Ph	0.72 [Ohm]
HP	3
K_t	0.21 [N.m/A]
Rated speed	3000 [rpm]
Rated power	1000 [Watts]
T_L	0.7 [N.m]

Table 2: Parameters of the BLDCM.

Parameters		ANN
Rise time	0–700 RPM	0.003
	700–900 RPM	0.003
Settling time	0–700 RPM	0.020
	700–900 RPM	0.003
Steady-state error	0–700 RPM	0.7%
	700–900 RPM	0.9%
Startup torque	0–700 RPM	3.2 N.N
	700–900 RPM	1.3 N.M
Startup current	0–700 RPM	3A
	700–900 RPM	1A
Speed variation	0.7%	0.6%
Power factor	0.7	0.8

current distortion and torque reduction in the BLDC motor, a suitable ANFIS controller is designed and implemented as a universal optimizer to find the optimized harmonics. Therefore, this proposed concept is designed and developed in three stages to minimize the distortion, where AI controllers have implemented optimized TPBLDCM. It is also considered to evaluate and improve the effectiveness and performance issues of the BLDC motor with this proposed algorithm. Finally, this concept will be implemented in Simulink/MATLAB with a comparative analysis of the BLDC motor and its modelling. The results encourage better performance than the conventional controllers. Figure 17 shows the simulation result of the phase current waveforms based on the rotor position at 700–900 rpm which is shown in Table 2. The peak current value is about 3 A for all I_a, I_b,

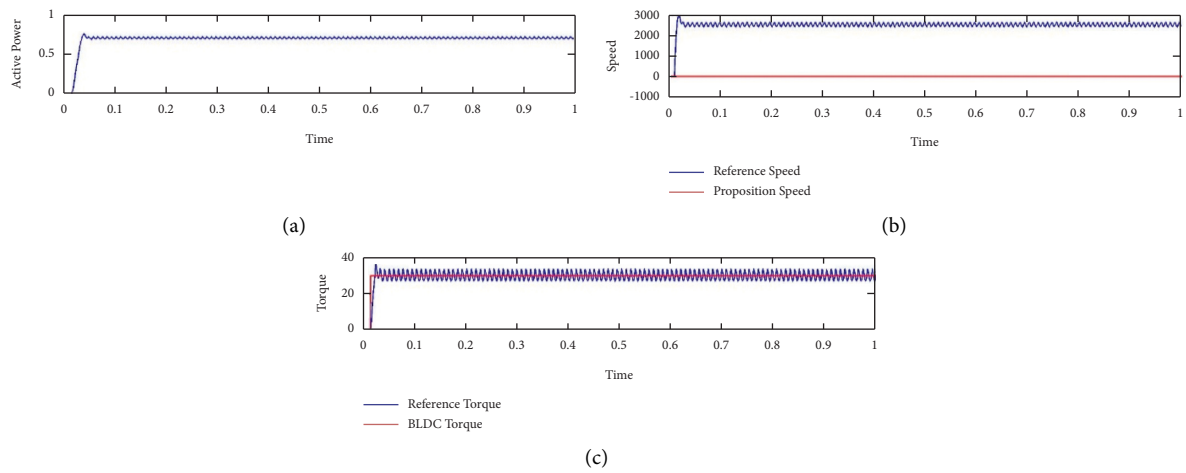

Figure 19: ANN designed. (a) Active power. (b) Reference speed and propulsion speed. (c) Reference torque and BLDCM torque of the BLDC motor.

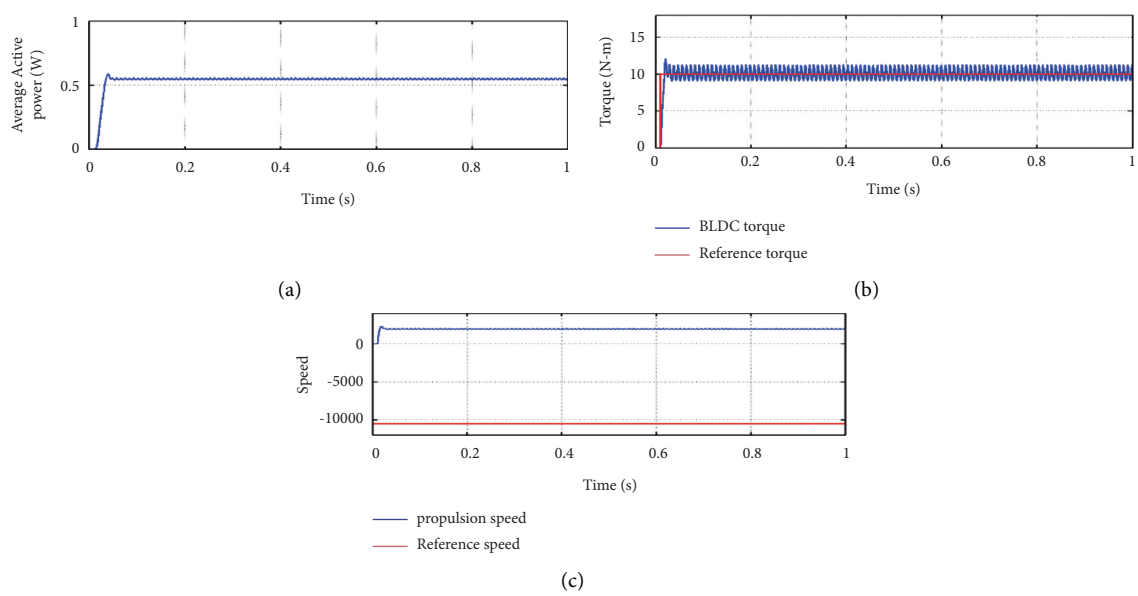

Figure 20: ANFIS designed. (a) Active power. (b) Reference speed and propulsion speed. (c) Reference torque and BLDCM torque.

and I_c, and steady state current varies from 0.7% to 0.9% with respect to the rise time shown in Table 2.

5. Conclusion

This paper concludes that the design of the neuro-fuzzy controllers is an effective controller for optimizing the disturbances and increasing the speed of the motor drive. The proposed controllers are the ANFIS controllers which will be designed with the suitable supervisory learning algorithm. Fuzzy logic control is designed with the 25 membership functions and connected to the four layers of artificial neural networks with two inputs and the derivative error. The gradient descent method of the supervisory learning algorithm for the ANFIS improves its operation because of its simple designed structure, learning capability, and high robustness against distortions, high-speed torque disturbances, uncertain hidden layers, and precise accuracy. This controller will act as an independent controller to the entire system's plant and will be applied to any nonlinear and uncertain approach. These ANFIS controllers also perform better than the PID controllers in tracking the reference speed, lower overshoot, optimized settling time, and low ripples with high-tracking efficiency.

Data Availability

The data are available upon request.

Conflicts of Interest

The authors declare that they have no conflicts of interest.

References

[1] S. Sivakotiah and J. Rekha, "Speed control of brushless DC motor on resonant pole inverter using a fuzzy logic controller," *International Journal of Engineering Science and Technology*, vol. 3, no. 10, pp. 7360–7357, 2011.

[2] S. A. Niapour, G. H. Garjan, M. Shafiei, M. R. Feyzi, S. Danyali, and M. Bahrami Kouhshahi, "Review of permanent-magnet brushless DC motor basic drives based on analysis and simulation study," *International Review of Economics Education*, vol. 9, no. 5, pp. 930–957, 2014.

[3] M. H. Rashid, "Power electronics: circuits, devices, and applications," *Pearson Education India*, vol. 76, pp. 778–789, 2009.

[4] A. Rubaai, R. Ricketts, and M. Kankam, "Development and implementation of an adaptive fuzzy-neural-network controller for brushless drives," *IEEE Transactions on Industry Applications*, vol. 38, no. 2, pp. 441–447, 2002.

[5] K. Sujatha, K. Naga, V. Vaisakh, and G. Anand, "Artificial intelligence-based speed control of brushless DC motor," *IEEE PES General Meeting. IEEE*, vol. 776, 2010.

[6] F. Mosavi and R. Mohammad, "Design of efficient adaptive neuro-fuzzy controller based on supervisory learning capable for speed and torque control of BLDC motor," *Przeglad Elektrotechniczny*, vol. 88, pp. 238–246, 2012.

[7] J. S. R. Jang, "ANFIS: adaptive-network-based fuzzy inference system," in *Proceedings of the IEEE Transactions on Systems, Man, and Cybernetics*, vol. 23, no. 3, pp. 665–685, June 1993.

[8] A. H. Niasar, H. Moghbelli, and A. Vahedi, "Modeling, simulation and implementation of four-switch, Brushless DC motor drive based on switching functions," *IEEE EUROCON 2009*, vol. 667, 2009.

[9] A. Abraham, "Neuro-fuzzy systems: state-of-the-art modelling techniques," in *Proceedings of the International Work-Conference on Artificial Neural Networks*, p. 444, Springer, Berlin, Heidelberg, June 2021.

[10] G. MadhusudhanaRao, Ch. Vinay Kumar, and A. RaghuRam, "Fuzzy based vector control method for BLDC motor drive with five-switch three-phase topology," *PalArch's Journal of Archaeology of Egypt/Egyptology*, vol. 17, no. 12, pp. 147–160, 2020.

[11] N. A. Halvai, M. A. S. Masoum, and H. Moghbeli, "Adaptive neuro-fuzzy intelligent controller via emotional learning for indirect vector control (IVC) of induction motor drives," in *Proceedings of the 12th Iranian Conference on Electrical Engineering*, p. 226, IEEE, May 2004.

[12] J. Žilkova, J. Timko, and P. Girovský, "Nonlinear system control using neural networks," *Acta Polytechnica Hungarica*, vol. 3, no. 4, pp. 85–94, 2006.

[13] Ch. Vinay Kumar, G. MadhusudhanaRao, and A. Raghu Ram, "AI based vector control method for BLDC motor with multi switch three-phase topology," *PSYCHOLOGY AND EDUCATION*, vol. 58, no. 1, pp. 3132–3141, 2021.

[14] B. Allaoua, A. Abdessalam, G. Brahim, and N. Abdelfatah, "Efficiency of particle swarm optimization applied on fuzzy logic DC motor speed control," *Serbian Journal of Electrical Engineering*, vol. 5, no. 2, pp. 247–262, 2008.

[15] C.-T. Lin and Y. C. Lu, "A neural fuzzy system with fuzzy supervised learning," *IEEE Transactions on Systems, Man, and Cybernetics-Part B: Cybernetics: A Publication of the IEEE Systems, Man, and Cybernetics Society*, vol. 26, no. 5, pp. 744–763, 1996.

[16] S. Singh and B. Singh, "Power factor correction in permanent magnet brushless DC motor drive using single-phase Cuk converter," *Journal of Engineering Science & Technology*, vol. 5, no. 4, pp. 412–425, 2010.

[17] J. Cao, "Torque ripple control of position-sensorless brushless DC motor based on neural network identification," in *Proceedings of the 2008 3rd IEEE Conference on Industrial Electronics and Applications*, IEEE, June 2008.

[18] K. Premkumar and B. V. Manikandan, "Adaptive neuro-fuzzy inference system based speed controller for brushless DC motor," *Neurocomputing*, vol. 138, pp. 260–270, 2014.

Hindawi
Journal of Electrical and Computer Engineering
Volume 2022, Article ID 7306548, 10 pages
https://doi.org/10.1155/2022/7306548

Research Article

Design and Implementation of Intelligent Control Garbage Bin

Li-Fen Tu, Qi Peng, and Rongpan Deng

School of Physics and Electronic Information Engineering, Hubei Engineering University, Xiaogan 432000, China

Correspondence should be addressed to Qi Peng; petersky0316@163.com

Received 31 March 2022; Revised 6 June 2022; Accepted 15 June 2022; Published 6 July 2022

Academic Editor: Ahmed A. Zaki Diab

Aiming at the problem that it was difficult to popularize accurate garbage sorting and delivery, a kind of intelligent garbage bin that is more intelligent, efficient, and functional than the traditional garbage bin was designed and manufactured. The design was based on the STM32 minimum system implementation. The speech recognition module was used to receive the key words and identify which type of garbage the item belongs to. At the same time, a speech reminder was given, and the steering gear was driven to automatically open the corresponding type of garbage bin lid, and the sorting collection was realized. In addition, the ultrasonic distance measuring module was used to detect the residual capacity of the garbage bin in real time. When it was about to be full, the data would be sent to the background management system through the WIFI module to remind the staff to clean it up. The experimental results show that the intelligent garbage bin can effectively help people sort and put domestic garbage and prevent garbage overflow from affecting the living environment, so as to realize the service of science and technology for human beings.

1. Introduction

With the rapid growth of urban population, the pressure on waste disposal has increased significantly. If this waste is not disposed of effectively, it can lead to serious health and environmental problems [1]. Therefore, in recent years, the concept of garbage sorting has been recognized all over the world. Its purpose is to improve the resource value and economic value of waste, reduce the amount of waste treatment and the use of treatment equipment, reduce treatment costs, and reduce the consumption of land resources, with social, economic, ecological, and other benefits [2].

At present, garbage sorting is mainly divided into two methods: central sorting and local sorting [3]. Central sorting has a low requirement for the public's knowledge reserve. Traditional trash bins are used to recycle all kinds of garbage. After all garbage enters the recycling station, centralized sorting is performed according to the type of garbage. At present, central sorting is mainly realized by manual or robots, among which robot sorting mainly relies on methods based on deep learning to perform target detection, classification, and recycling of garbage image information [4]. Local sorting needs to use the classified garbage bins instead of traditional garbage bins, that is, to achieve classified delivery at the front end [5]. The advantage of this method is that it can effectively avoid the problem of secondary pollution caused by the mixing of garbage in the central sorting method during the transfer of garbage. The disadvantage is that the user needs to put different garbage separately, which will increase the time cost of users but save the time cost of postprocessing. On the whole, the social time cost has not increased significantly. Therefore, more and more classified garbage bins are distributed in various locations of the city, and there have even been a large number of household classified garbage bins [6].

To achieve effective local garbage sorting, users need to have the knowledge of garbage separation so that garbage can be put into the right bins. However, there are many kinds of garbage. Even if people have the awareness of garbage sorting, they often cause wrong disposal due to the lack of knowledge of garbage sorting. In recent years, in order to avoid the problem of wrong disposal, a variety of automatic sorting garbage bins have been produced, which are mainly divided into methods based on image recognition [7, 8] and speech recognition [9, 10]. The method based on image recognition relies on the camera to capture the image of garbage and compare it with the database to determine the type of garbage. This method mainly relies on target

detection algorithm based on deep learning. Its classification accuracy depends on the accuracy of target detection algorithm, and the effect is good. However, image recognition has high requirements on hardware and recognition environment, so the popularization cost is high. The method based on speech recognition recognizes the garbage name spoken by the user through speech recognition chip and compares it with the corpus to determine the type of garbage. The classification accuracy of this method depends on the accuracy of speech recognition, which is higher than that of image recognition, with lower cost and stronger environmental adaptability. But it is not friendly to people with certain speech and hearing difficulties. In addition, since the intelligent local sorting garbage bins are distributed outdoors, the problem of power supply needs to be considered.

To sum up, combined with the actual needs and based on the method of speech recognition, this paper designs an intelligent control garbage bin that automatically reminds and helps people to classify garbage scientifically and accurately. Compared with the traditional classification garbage bin, the intelligent garbage bin designed in this paper can automatically and accurately classify garbage items according to the name of garbage items informed by the user's speech and automatically open the corresponding bin lid, which is convenient for the user to put in. In addition, ultrasonic ranging and wireless data transmission are added in the box. When a certain type of garbage is almost full, the data will be automatically sent to the garbage management department to facilitate the timely cleaning of garbage, ensure environmental hygiene, and improve work efficiency, avoiding unnecessary garbage removal and transportation work. Compared with the automatic sorting garbage bin based on speech recognition designed in the literature [9, 10], manual mode has added to the garbage bin designed in this paper, which combines the traditional sorting garbage bin with the automatic sorting garbage bin. The advantage is that there is no need for secondary sorting for some common garbage that is easy to classify, or for the garbage that users have already sorted at home, saving the delivery efficiency. More importantly, it is more friendly to users with certain speech and hearing difficulties, ensuring the harmonious development of society. In terms of electricity, since the power consumption of the garbage bin is not high, it can be powered by small solar cells outdoors [11].

The rest of the paper is organized as follows: in Section 2, we describe our system, including the overall design and the design of each functional module; the system implementation is in Section 3; the system testing and result analysis are discussed in Section 4, followed by the conclusion in Section 5.

2. The System Design

2.1. The Overall Design. The STM32F103 is taken as the main control data transmission part, which also includes the part of garbage type recognition by speech, the part of ultrasonic detection whether garbage is full, the part of steering gear for opening the garbage bin lid, and the part of WiFi module for storing and sending data. The system block diagram of intelligent garbage bin is shown in Figure 1.

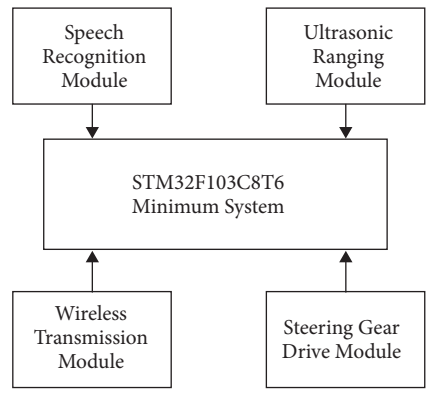

Figure 1: The system block diagram of intelligent garbage bin.

When the user is not sure which type of garbage belongs to, just say the name of the garbage, the speech recognition module will automatically recognize the input voice (garbage name), the system will automatically search for the garbage that belongs to that category and make a voice reminding and, at the same time, drive the steering gear to open the lid of the corresponding type of garbage bin for people to put this type of garbage. The ultrasonic ranging module will detect the garbage loading in each bin in real time. If the garbage reaches a certain level, the wireless transmission module will send the data of which bin needs to be cleaned and replaced to the background staff, reminding them to clean up the garbage in time.

2.2. Functional Module Design

2.2.1. Speech Recognition Module. Speech recognition [12, 13] is to convert the content of human speech vocabulary into the input that can be read by the computer. It is divided into two stages: training and recognition. Both of these two stages must preprocess the input speech and extract the characteristics. During the training period, a large amount of speech corpus was collected, and the feature parameters were obtained by preprocessing and feature extraction. Finally, the training speech reference library was established through modeling. The recognition stage is to compare the features in the input speech with those in the reference model and then take the most similar input as the output of the recognition result, so as to achieve speech recognition.

The system designed in this paper needs to analyze the input voice content and give four results of "recyclable garbage," "harmful garbage," "food garbage," and "other garbage" to drive different garbage bin lids. In this paper, the LD3320 developed by ICRoute Company in the United States [14] is used to achieve the realization. The core chip contains a speech recognition signal processor and some other external integrated circuits, which can be directly integrated with the company's existing hardware products to easily achieve automatic speech recognition, automatic voice control, human-computer interaction dialogue, and other functions. The internal host computer has developed a configuration software, which can be opened to access and

configure the internal resources of the speech module, and to add or delete human-computer interaction entries. The configuration of the speech module software entry is shown in Figure 2.

When the speech recognition program is powered on and initialized, it enters the state of waiting to be woken up. The microphone monitors whether there is voice command input from the outside in real time. After receiving the voice input with instruction, the input instruction is compared with the list of keywords to determine whether the input instruction is correct or not. After judging the correct operation instruction, the analysis results are determined whether it belongs to "recyclable garbage," "harmful garbage," "food garbage," or "other garbage." After the judgment is completed, the data will be stored and sent to the STM32 master control module to end the program running [15, 16]. The program flowchart of the speech recognition module is shown in Figure 3.

2.2.2. Steering Gear Drive Module. The steering gear [17] is mainly composed of shell, circuit board, driving motor, reducer, and steering gear position motion sensor. Its working principle is that the receiver sends a power signal to a steering gear swing arm and drives it through an IC, and the motor swing arm begins to rotate at high speed. The axial power is transmitted to the front end of the steering gear's swing arm through the gear of the reducer, and the power signal is transmitted through the detector at a fixed position to determine whether the designated position has been reached. The signal of the controller is connected to the signal receiving chip of the modulator through the channel on the receiver to obtain the DC bias voltage regulator.

When the steering gear is powered on, the signal will be detected to determine whether the driving signal [18] is received. When the signal is received, the motor rotates to drive the torque shaft. At the same time, the stop signal will be detected and judged, and the rotation will end when the signal is received. In this paper, the MG90S model simulation steering gear is selected, which has a large pulling force and is suitable for various experimental scenes. The operation is fast, the service life is long, and the torque is large. The program flowchart of the steering gear drive module is shown in Figure 4.

2.2.3. Ultrasonic Ranging Module. Ultrasonic ranging [19] is to calculate the distance by measuring the time difference between the ultrasonic transmitter transmitting and receiving ultrasonic waves. The transmitter of the ultrasonic ranging module will transmit a certain frequency signal and then be reflected back by the object. It will be converted into a voltage of mV energy by the receiver, and then the module will process and calculate it internally. Use formula (1) to get the distance between the module and the target object:

$$L = \frac{C \bullet t}{2}, \tag{1}$$

where t is the time from ultrasonic transmission to reception, the unit is s; C is the propagation speed of ultrasonic in the air, which is a constant 340 m/s; and L is the distance between the sensor and the target to be measured, the unit is m.

In this paper, the HC-SR04 module is used to realize ultrasonic ranging, and the capacity of the garbage in the garbage bin is obtained in real time. When the capacity reaches the preset value, an output signal is given to remind the staff to clean up. The HC-SR04 ultrasonic ranging mode (except the power cord) is a two-wire system. When starting, the module will send out a certain number of pulse signals with a certain frequency. The IO terminal of the master IC will detect the echo. When a signal returns, the IO terminal will output a high level. This time difference is calculated by the duration of the high level. In these programs, the measurement time of ultrasonic wave is calculated by the STM32 timer [20], and then the program calculates the average value and judges whether it is in the normal range to decide whether to run the next step. The program flowchart of the ultrasonic ranging module is shown in Figure 5.

2.2.4. Wireless Transmission Module. The WIFI module uses a specific channel to quickly connect to the Internet. The wireless signals received from the antenna [21] are filtered and transmitted to the power amplifier circuit to achieve power increase. After being processed by the WiFi chip, the information is transmitted to the CPU through the SDIO interface and then sent to the software or application program, which is converted into data signals suitable for transmission and sent to the antenna.

In this design, the ESP8266 series WIFI module is selected to realize the transmission function of garbage-filled signal. After the system is powered on, it will automatically connect to WiFi, automatically connect to the server, synchronize data with the server, and wait for the user to input instructions. After receiving the operation instruction, the ESP8266 will store and send data in real time. The program flowchart of the wireless transmission module is shown in Figure 6.

3. The System Implementation

In order to test the function of the designed garbage bin, the hardware system is designed, and its hardware system module connection diagram is shown in Figure 7(a). It contains wireless transmission module, transceiver, garbage bin, speech recognition module, ultrasonic ranging module, and control system. Among them, the wireless transmission module is used to receive the digital control signal from the control system and forward it to the transceiver in the garbage bin, to receive the garbage height feedback signal from the transceiver and forward it to the control system, and to receive the digital speech information keywords from the speech recognition module and forward it to the control system. The transceiver is used to receive the digital control signal from the wireless transmission module and transmit it to the signal modulation chip, to receive the garbage height signal from the ultrasonic ranging module and package it into the feedback signal, and to send the feedback signal to

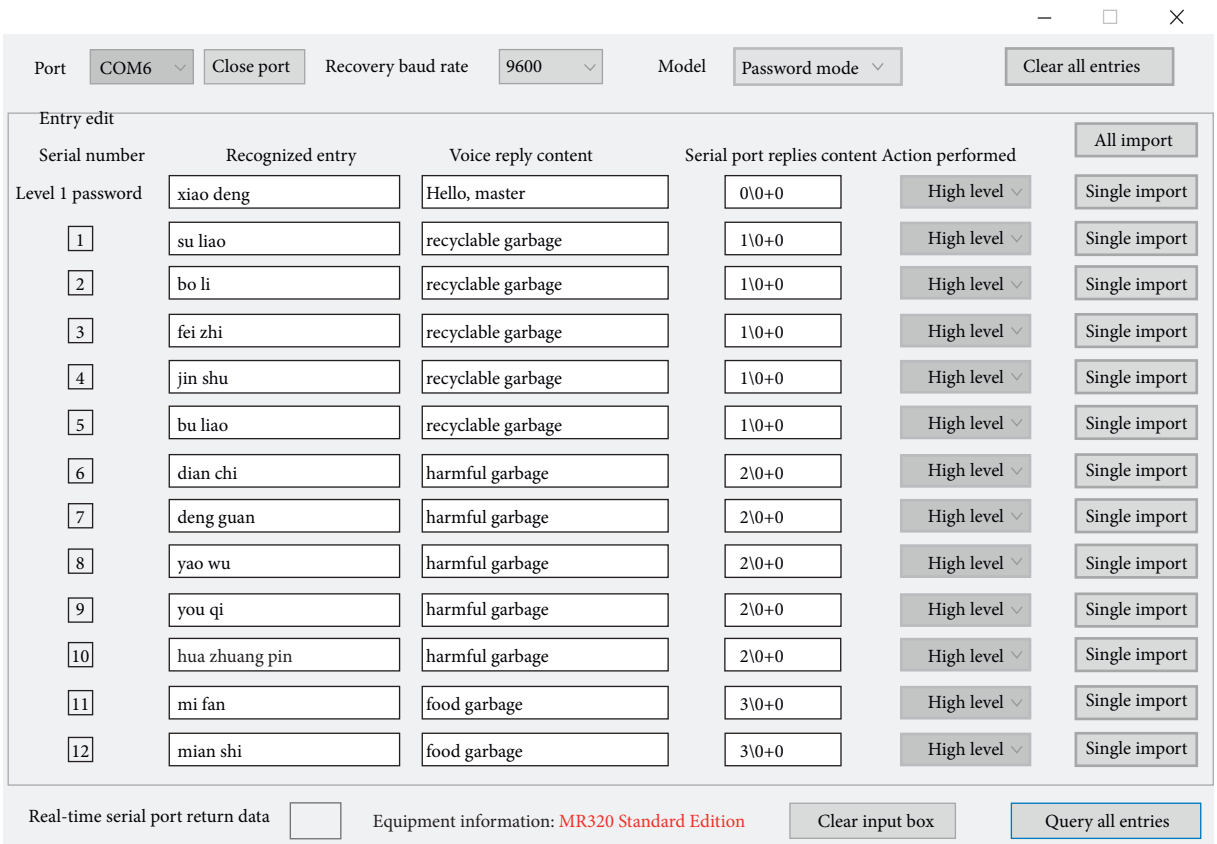

Figure 2: Add or delete entries in the speech module.

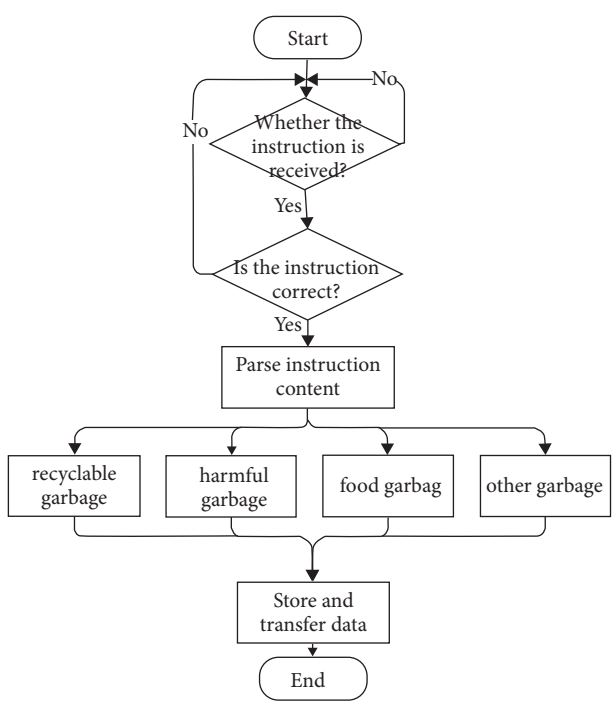

Figure 3: Speech recognition module flowchart.

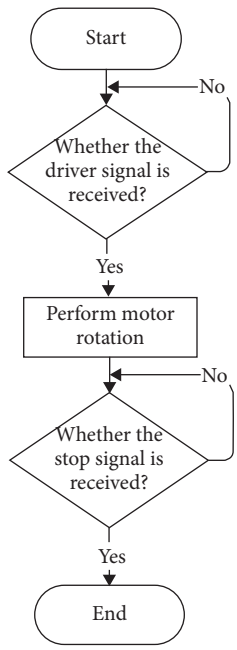

Figure 4: Steering gear drive module flowchart.

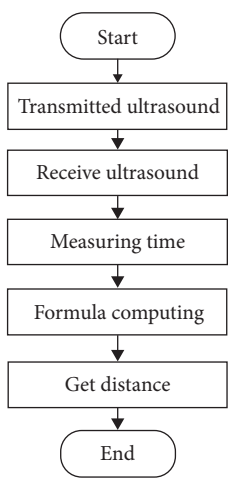

Figure 5: Ultrasonic ranging module flowchart.

the wireless transmission module. The garbage bin is used for sorting and storing rubbish. The speech recognition module is used to receive the analog speech message from the user, then to convert the analog speech message into the digital speech message, then to recognize the keywords in the digital speech information, and finally to send the keywords to the control system. The ultrasonic ranging module is used to detect the height of the garbage stored inside the garbage bin in real time. The control system is used to receive the feedback signals and keywords from the wireless transmission module, then to process the digital control signals according to the feedback signals and keywords, and finally to send them to the wireless transmission module. The assembly diagram of hardware system is shown in Figure 7(b).

The software flowchart of the system is shown in Figure 8. First, the system is initialized, and the speech recognition module judges whether the command is received. If it receives a voice command, it judges whether the command belongs to a correct detection command and then judges the content of the command and analyzes which type of garbage belongs to. If no voice command is received, it determines whether there is a manual operation, and if there is manual operation, it directly locates a certain type of garbage according to the manual operation button. The system drives the steering gear to open the corresponding garbage bin according to the speech recognition result or the garbage type selected manually. The ultrasonic ranging module detects the garbage loading height in the garbage bins. If it is full, it will be reported to the back-end control system by the WIFI module.

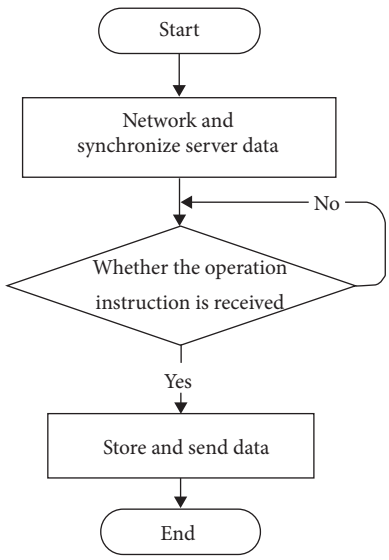

Figure 6: Wireless transmission module flowchart.

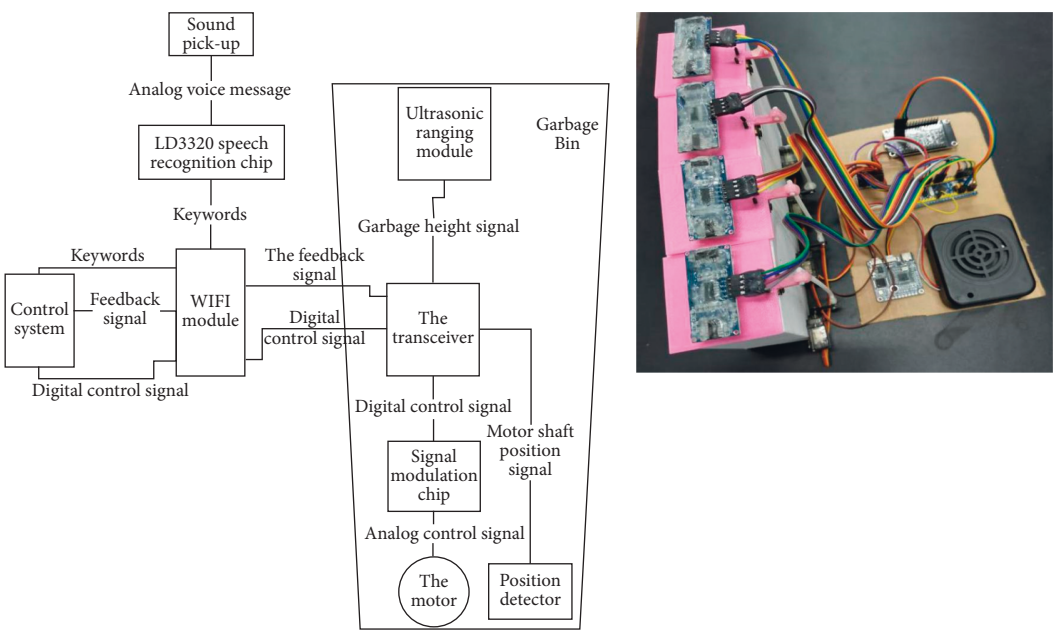

(a) (b)

Figure 7: (a) The hardware system module connection diagram of the intelligent garbage bin. (b) The assembly diagram of hardware system.

4. System Test and Result Analysis

The software is written by Keil μVision5 software. The program includes speech recognition part, ultrasonic ranging detection part, steering gear driving part, and WiFi module used to store and send data. After the program is compiled, a .hex file is generated, and then the program is downloaded and recorded into the STM32 minimum system for functional testing.

4.1. Function Test and Realization of Speech Recognition and Steering Gear Modules. First, adjust the appropriate distance to the microphone of the speech recognition module, and say the wake-up word "Xiao Deng" to wake up the speech recognition module. Before the speech recognition module is woken up, the working indicator light is off, and at this time, any key words shouted into the microphone will not be recognized by the system. When the speech recognition module is successfully woken up, the working indicator light on the speech recognition module will light up and enter the state of waiting for command input. The state before and after the speech recognition module is successfully awakened and is shown in Figure 9.

After the speech recognition module is successfully awakened, it shouts "Open all the garbage bins" to the speech recognition module, and the module replies "05" through

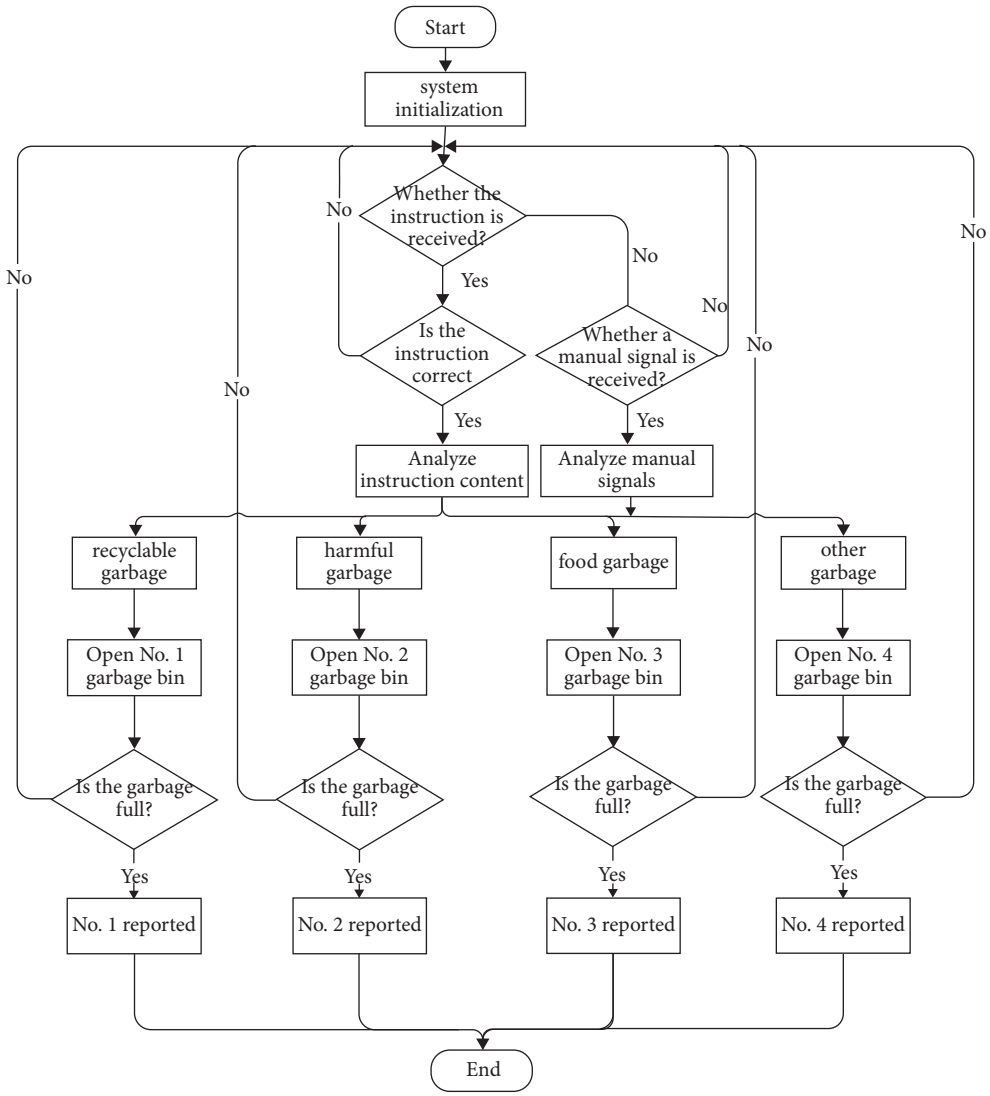

Figure 8: The software flowchart.

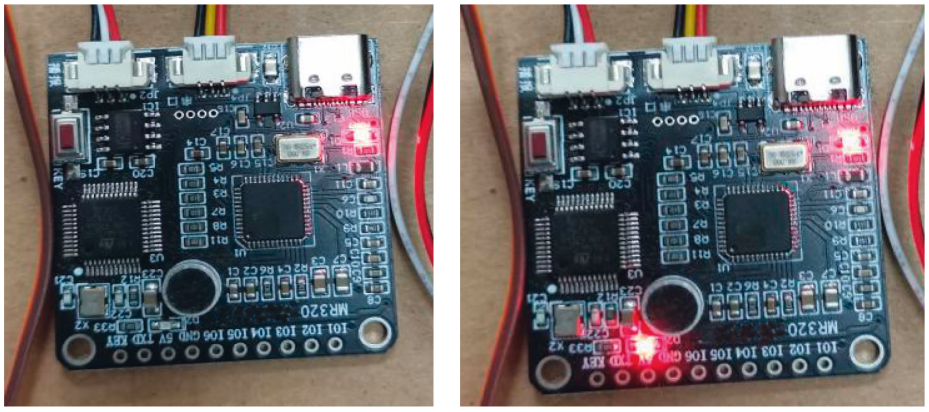

(a) (b)

Figure 9: Different states of speech recognition module. (a) Speech recognition is not awakened, and the recognition indicator is off. (b) Speech recognition is awakened, and the recognition indicator is on.

the serial port and sends the corresponding data to the STM32 master control module. According to the internal program, the steering gear is controlled to drive the motor to rotate, open the lids of all the garbage bins, and wait for people to put garbage in or replace the garbage bins and other operations. During the waiting process, the waiting delay is automatically closed, and the lid will not be closed automatically before the voice input "close all the garbage bins" command. After inputting the "close all the garbage bins" command, the ultrasonic ranging module detects the loading status of the garbage bins and sends the data to the back-end management APP in real time, which is convenient for management staff to observe the garbage loading level in the garbage bins and replace some bins in time.

Select the appropriate distance to the microphone of the speech recognition module, and say the preset keywords corresponding to the classification, and the speech recognition module will automatically recognize and compare the keywords. The voice broadcast provides the garbage category that people throw and feeds back the data to the STM32 master control module. The internal program controls the corresponding steering gear to drive the motor to rotate and open the corresponding garbage bin lid for people to throw. Say the internally set keywords of "recyclable garbage," "harmful garbage," "food garbage," and "other garbage," respectively, the speech recognition module can identify and broadcast the garbage to which category it belongs to quickly, effectively, and accurately, and drive the steering motor to rotate, open the corresponding garbage bin lid, and wait for people to put the garbage in, the waiting time is 3–5 s. After the waiting time is over, the lid of the garbage bin is closed automatically. If it is necessary to continue throwing, you can say the garbage keywords again. After the lid of the garbage bin is opened, the garbage can be put into the garbage. This design can recognize and operate the next keyword again after responding to one instruction. The six states of the garbage bin are shown in Figure 10.

The classification accuracy of the system mainly depends on the accuracy of speech recognition. The recognition accuracy of the speech recognition chip used by the system is 95% [22]. The recognition results are affected by excessive speed, low voice, surrounding noise, and dialect problems. After all kinds of common garbage, people in the natural environment, using normal speed and volume to test the system, the garbage bin can open the correct lid. However, human factors can lead to the problem of misplacement of garbage. For example, there are various types of paper. "Book paper" belongs to "recyclable garbage," but "toilet paper" belongs to "other garbage." Therefore, if the user speaks the garbage name incorrectly, it will lead to misclassification and reduce the reliability of the system to some extent.

4.2. Function Test and Realization of Ultrasonic Ranging and Wireless Transmission Modules. When the lid of the garbage bin is closed, the ultrasonic ranging module starts to detect the garbage loading condition and sends the detected data to the STM32 master control module, and then the WiFi module sends the data to the back-end management APP. It is convenient for back-end management staff to grasp the loading status of garbage in the garbage bin in real time, realize the intelligent service. The data display of the back-end APP is shown in Figure 11. At this time, it shows that the garbage loading in the four garbage bins have not reached the state of early warning and replacement.

After adjusting the distance from the microphone of the speech recognition module, say the keywords of the food garbage set internally, and the speech recognition module successfully identifies the food garbage and gives a voice notification. The STM32 master control module drives the motor of the steering gear to rotate, opens the corresponding bin lid, and waits for the garbage to be placed. In this experiment, a plastic cylinder with a height of about 9–10 cm is used to replace the garbage and put it into the garbage bin. After waiting for the lid of the garbage bin shut down automatically, the ultrasonic ranging module starts to detect the garbage loading condition and sends the detected data to the STM32 master control module. The STM32 master control module synchronizes the data to the internal ESP8266 of the WiFi module. After the data synchronization is completed, the data is sent to the produced back-end management APP, and the garbage loading height in the garbage bin is fed back in real time. The internal control program sets the ultrasonic ranging module to reach the state of early warning replacement if the detected distance is less than 5 cm. The height of the test cylinder is 9–10 cm, and the height of the garbage bin is about 13 cm. Therefore, the system judges that the loading height of No. 3 garbage bin (food garbage) has reached the state of early warning. The data fed back by the WiFi module to the back-end management APP shows that the food garbage is in an early warning and replacement state, as shown in Figure 12. The judgment process for other types of garbage is similar.

If the user puts in a large amount of garbage at one time after the garbage can is opened, it may cause the lid of the garbage cannot be closed properly and even affect the environment because of garbage overflow. Therefore, we have designed the software accordingly. When the lid of the garbage bin is opened for more than the set time (1 minute set in the experiment, adjustable), and the closing signal of the lid is still not received, the status of the garbage bin will be judged as "full" directly, and the WiFi module will be triggered to feed back to the back-end management module to prompt the garbage removal and transportation in time.

5. Discussion

This design uses speech recognition technology to achieve local sorting of garbage. Before people put garbage in, say the corresponding garbage name, the system automatically compares the keywords, prompts people which category of garbage they want to put in, and automatically drives the steering gear to open the lid of the corresponding type of garbage bin, which is fast, convenient, and effective to help people intelligent garbage classification. For common easy-to-sort garbage or garbage that has already been classified, people can also choose to manually open the corresponding category of garbage bins for delivery. Manual mode saves

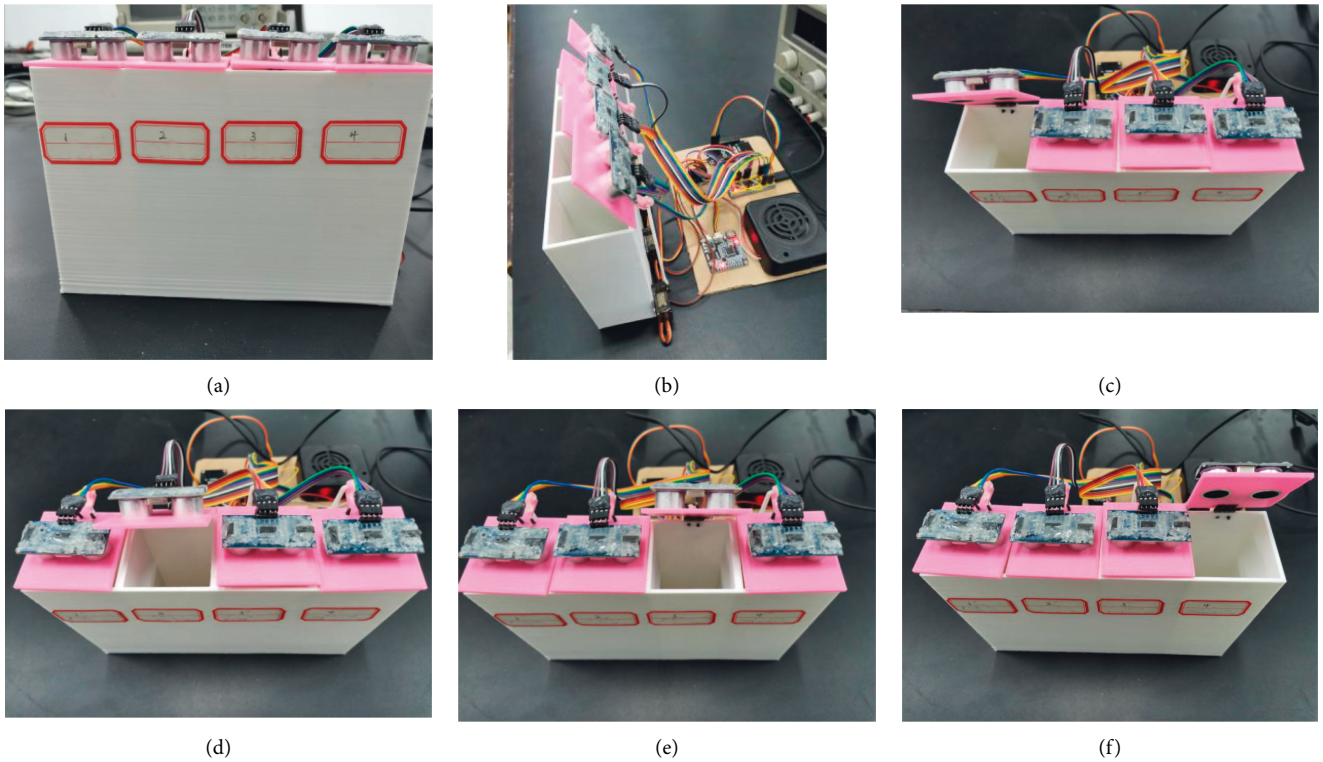

Figure 10: The six states of the garbage bin. (a) All closed state. (b) All open state. (c) The recyclable garbage bin is open. (d) The harmful garbage bin is open. (e) The food garbage bin is open. (f) The other garbage bin is open.

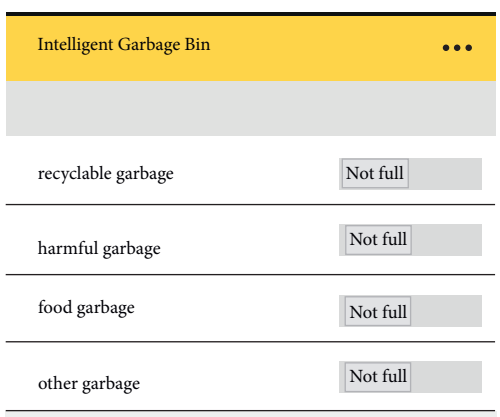

Figure 11: All garbage bins have not reached the status of early warning replacement.

time in garbage disposal and is friendly to people with certain speech and hearing difficulties. When a certain type of garbage is about to be filled, it can also automatically send a full-load signal to the data center, prompting the management department to deal with the garbage in time. The test results show that the intelligent garbage bin is simple and effective and provides a feasible solution for garbage classification and public environmental protection.

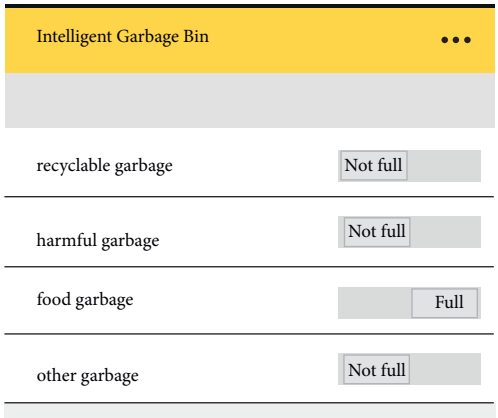

Figure 12: The food garbage has reached the status of early warning replacement.

Data Availability

The data used to support the findings of this study are included within the article.

Conflicts of Interest

The authors declare that they have no conflicts of interest.

Acknowledgments

The authors gratefully acknowledge the financial support provided by the Natural Science Foundation of Xiaogan (XGKJ2021010005).

References

[1] Y. Ding, J. Zhao, J. W. Liu et al., "A review of China's municipal solid waste (MSW) and comparison with international regions: management and technologies in treatment and resource utilization," *Journal of Cleaner Production*, vol. 293, Article ID 126144, 2021.

[2] H. Wilts, B. R. Garcia, R. G. Garlito, L. S. Gómez, and E. G. Prieto, "Artificial intelligence in the sorting of municipal waste as an enabler of the circular economy," *Resources*, vol. 10, no. 4, p. 28, 2021.

[3] S. R. J. Ramson, S. Vishnu, A. A. Kirubaraj et al., "A LoRaWAN IoT-Enabled trash bin level monitoring system[J]," *IEEE Transactions on Industrial Informatics*, vol. 18, no. 2, pp. 786–795, 2021.

[4] R. Sultana, R. D. Adams, Y. Yan et al., "Trash and Recycled Material Identification Using Convolutional Neural Networks (CNN)," in *Proceedings of the 2020 SoutheastCon*, pp. 1–8, IEEE, Raleigh, NC, USA, March 2020.

[5] C. D. Yu and N. Du, "Research on resident garbage sorting and recycling system based on green environmental protection technology," *IOP Conference Series: Earth and Environmental Science*, vol. 558, no. 4, Article ID 042032, 2020.

[6] R. P. Setiawan, "Factors determining the public receptivity regarding waste sorting: a case study in Surabaya city, Indonesia," *Sustainable Environment Research*, vol. 30, no. 1, pp. 1–8, 2020.

[7] R. E. Liu, J. Xiong, J. Wei et al., "Design of intelligent classification trash bin based on database and image recognition," in *Proceedings of the 2021 3rd International Academic Exchange Conference on Science and Technology Innovation (IAECST)*, pp. 872–875, Guangzhou, China, December 2021.

[8] J. Gu, J. Zhang, H. Sui, and B. Zou, "Research on intelligent trash bin design based on visual recognition of machine," *IOP Conference Series: Earth and Environmental Science*, vol. 687, no. 1, Article ID 012170, 2021.

[9] F. Fang and L. Ling, "The design of the intelligent household trash classification based on speech recognition," in *Proceedings of the 2021 2nd International Conference on Artificial Intelligence and Information Systems*, pp. 1–4, Chongqing China, May 2021.

[10] C. Xiong, "Design of intelligent garbage classification bin based on LD3320," in *Proceedings of the 2021 international conference on signal processing and machine learning (CONF-spml)*, pp. 7–10, Stanford, CA, USA, November 2021.

[11] A. Hojjati, W. Nasar, D. Mishra et al., "Cloud-based smart iot sustainable solution for waste sorting and management," in *Proceedings of the 2022 IEEE/SICE International Symposium on System Integration (SII)*, pp. 218–224, Narvik, Norway, January 2022.

[12] M. H. Yu, H. Gong, Z. Y. Wu, and S. J. Li, "Design of voice carpooling system based on the LD3320," *Applied Mechanics and Materials*, vol. 602-605, pp. 2913–2916, 2014.

[13] L. Yan and H. Jiexian, "Design of the smart home system based onwireless voice control," *Computer & Telecommunication*, vol. 1, no. 7, pp. 68–70, 2017.

[14] L. I. Hai, X. Wang, and Y. Tian, "Design and realization of intelligent sorting robot based on STM32F4," *Experimental Technology and Management*, vol. 13, 2019.

[15] B. Yang, "Design and implementation of intelligent home wireless gateway based on STM32," in *Proceedings of the 2017 4th International Conference on Information Science and Control Engineering (ICISCE)*, pp. 258–260, IEEE, Changsha, China, July 2017.

[16] W. C. Han, L. S. Huang, and N. H. Pan, "Design of intelligent drip irrigation system based on STM32," *Journal of Anhui Agricultural Sciences*, vol. 45, no. 18, pp. 167-168, 2017.

[17] T. Xiaoyu, Y. Zengchun, Z. Hao et al., "The design research of the indigenous steering gear," in *Proceedings of the 2016 Chinese Control and Decision Conference (CCDC)*, pp. 6947–6952, IEEE, Yinchuan, China, May 2016.

[18] Y. M. Huang and W. T. Co, "Design of integrated controller for steering gear and stepper motor," *Value Engineering*, vol. 39, no. 4, pp. 225-226, 2020.

[19] J. Q. Zhang, J. Zhang, and H. Y. Zhao, "Design of high-precision ultrasonic ranging system," *Applied Mechanics and Materials*, vol. 563, pp. 199–202, 2014.

[20] S. U. Rui, G. U. O. Huan, F. A. N. Yisong et al., "Design of pulse laser intelligent control system based on STM32," *Chinese Journal of Quantum Electronics*, vol. 36, no. 2, p. 161, 2019.

[21] C. Castro, R. Elschner, T. Merkle, C. Schubert, and R. Freund, "Experimental demonstrations of high-capacity THz-wireless transmission systems for beyond 5G," *IEEE Communications Magazine*, vol. 58, no. 11, pp. 41–47, 2020.

[22] X. Zhao, B. Zhou, and Z. Fan, "Research on image acquisition and wireless transmission based on STM32," in *Proceedings of the 2015 5th International Conference on Information Science and Technology (ICIST)*, pp. 334–338, Changsha, China, April 2015.

Hindawi
Journal of Electrical and Computer Engineering
Volume 2022, Article ID 5284185, 10 pages
https://doi.org/10.1155/2022/5284185

Research Article

Automatic Lane Line Detection System Based on Artificial Intelligence

Gaoqing Ji and Yunchang Zheng

College of Electrical Engineering, Hebei University of Architecture, Zhangjiakou 075000, Hebei, China

Correspondence should be addressed to Yunchang Zheng; zyc2023@hebiace.edu.cn

Received 14 February 2022; Revised 27 April 2022; Accepted 23 May 2022; Published 9 June 2022

Academic Editor: Ahmed A. Zaki Diab

As the need for an intelligent transport system is growing rapidly, lane line detection has gained a lot of attention recently. Aiming at the problem that the YOLOv3 algorithm has low accuracy and high probability of missed detection when detecting lane lines in complex environments, a lane line detection method for improving YOLOv3 network structure is proposed. The improvement is focused on detection speed and accuracy. Firstly, according to the characteristics of inconsistent vertical and horizontal distribution density of lane line pictures, the lane line pictures are divided into $s * 2S$ grids. Secondly, the detection scale is adjusted to four detection scales, which is more suitable for small target detection such as lane line. Thirdly, the YOLOv3's backbone is changed by adopting Darknet-49 architecture. Finally, parameters of anchor and loss function are optimized so that they focus on detecting lane line. The experimental results show that on the KITTI (Karlsruhe Institute of Technology and Toyoko Technological Institute) dataset, the mean average precision value is 92.03% and the processing speed is 48 fps. Compared with other algorithms, it is significantly improved in detection accuracy and real-time performance. It is promising to employ the proposed approach in lane line detection system.

1. Introduction

Lane line detection is an important part of intelligent transport systems, such as in traffic monitoring and autonomous cars [1]. Therefore, the need for the lane line detection system is increasing in the industry [2].

There have been various approaches to lane line detection. These approaches are generally divided into two categories: traditional methods and deep-learning-based methods. Traditional methods use statistical approach in extracting image features, such as color, gray, and edge [3]. On the other hand, deep learning-based approaches use convolutional neural networks as their feature extractor [4].

Although the accuracy of traditional approach is still acceptable, the traditional approach must go through a complex process and requires high human involvement in the development and deployment process [5]. Furthermore, traditional approaches also cannot propagate its training feedback to its feature extractor section [6]. Therefore, this approach is considered not good for industry's production. The use of deep learning is one solution to answer the problem faced by the traditional approach.

One of the main issues in developing a deep learning model is the tradeoff between the level of accuracy with the speed of detection of the model. Models with high accuracy generally require quite complex feature extraction, which results in low detection speed. Therefore, building a deep learning model architecture needs to pay attention to both aspects.

One deep learning architecture that is highly considered to be used for object detection model is YOLO (You Only Look Once) [7]. The architecture uses a regression-based single step model. YOLO is considered to be one of the best architectures because it has a high detection speed without much sacrificing its detection accuracy [8].

For this paper, a lane line detection model will be built using the improved YOLOv3 architecture. The main contributions are as follows: firstly, according to the

characteristics of inconsistent vertical and horizontal distribution density of lane line pictures, the lane line pictures are divided into s ∗ 2S grids; secondly, the detection scale is adjusted to four detection scales, which is more suitable for small target detection such as lane line; thirdly, the backbone is changed by adopting Darknet-49 architecture; and finally, parameters of anchor and loss function are optimized so that they focus on detecting lane line.

2. Related Work

At present, the main methods of lane line detection include the method of extracting road features by machine vision, the method of establishing road model for detection, and the method of multi-sensor fusion detection [9].

The method of extracting road features by machine vision mainly uses machine vision technology to classify the gray value features and color features of lane lines. After learning, the lane lines on the road can be detected. Because the gray value, color and other features in the image are often affected by external conditions such as light intensity and shadow; the lane line detection using this method is easy to be disturbed by environmental changes [10].

The method of establishing the road model for detection is to establish a two-dimensional or three-dimensional image model of the road image and then compare it with the lane line in the photo which is to be detected. The application scope of this detection method is relatively small, and it is only suitable for roads with the characteristics of known templates. In addition, the algorithm has a large amount of computation and poor real-time performance.

The method of multisensor fusion detection is to detect the lane line by means of high-definition camera, UAV aerial photography, GPS, radar, and other fusion methods [11]. The cost of this method is high, and it is difficult to be applied in the large-scale practical lane line detection system [12, 13].

In this work, lane line detection process is done by using improved YOLOv3 model architecture. The model architecture is customized in such a way so that it can perform faster without much sacrificing its detection accuracy. The detected lane lines are then passed to the post-processing steps to validate each of them [14].

2.1. YOLOv3 Algorithm. YOLO is a real-time target detection algorithm proposed by Redmon et al. in 2016. It considers detection as a regression problem. Firstly, YOLO adjusts the size of the input image to a 448 ∗ 448 pixels, then convolutes the image, and finally detects the target by the full connection layer [15].

The algorithm divides the input image into s ∗ s grids. If the center point of the detected target falls into a grid, the grid is responsible for detecting the target. The numbers of parameters to be predicted for each grid are as shown in the following formula:

$$\text{Num} = s * s(5 * B + C). \tag{1}$$

In formula (1), B refers to the number of boundary boxes and C refers to the number of class probabilities [16]. Each bounding box includes five predicted values: X, Y, W, H, and Conf which refers to the confidence of each bounding box. (X, Y), respectively, represent the abscissa and ordinate values of the central point coordinates of the bounding box, and W and H are the width and height values of the bounding box.

The confidence of each bounding box refers to whether the goal is included in the bounding box and the accuracy of its prediction. The definition of confidence is shown in the following formula:

$$\text{Conf} = \Pr(\text{Object}) \times \text{IoU}(\text{Pred}, \text{Truth}). \tag{2}$$

In formula (2), Pr(Object) refers to the probability that the bounding box contains the target. When the target is included, Pr (Object) = 1; otherwise, Pr (Object) = 0. In formula (2), IoU (Pred, Truth) refers to the matching degree between the prediction box and the real boundary box [17]. Its definition is shown in formula (3), where area (Boxt ∪ Boxp) represents the area where the prediction box and the real bounding box intersect, and area (Boxt ∪ Boxp) represents the area where the prediction box and the real bounding box are combined. When the prediction box completely coincides with the real bounding box, IoU(Pred, Truth) = 1. When the two do not coincide et al. l, IoU (Pred, Truth) = 0.

$$\text{IoU}(\text{Pred}, \text{Truth}) = \frac{\text{area}(\text{Boxt} \cap \text{Boxp})}{\text{area}(\text{Box} \cup \text{Boxp})}. \tag{3}$$

In formula (4), Pr (Class I | Object) refers to the probability of conditional category which is based on the condition that the grid contains detection targets and each grid only predicts the probability of a specific category of targets [18]. Pr (Class i) is the probability that the detection target is a specific class target [19].

$$\Pr(\text{Class } i \mid \text{Object}) = \frac{\Pr(\text{Class } i)}{\Pr(\text{Object})}. \tag{4}$$

YOLOv3 is a single-stage target detection algorithm proposed in 2018. It not only maintains the operation speed of the algorithm but also improves the prediction accuracy. It is a popular real-time target detection algorithm [20]. The network structure model of YOLOv3 is shown in Figure 1.

Compared with the previous versions of YOLO, the main differences of the YOLOv3 algorithm are as follows: using darknet-53 (106 layers in total, including 53 convolution layers) basic network model; using independent logical classifier instead of the softmax function; and using a method similar to FPN for multiscale feature prediction. The previous version of YOLOv2 can only use 1 ∗ 1 convolution kernel to detect on a single feature map. The most prominent feature of YOLOv3 is that it can detect targets in three sizes. When the feature size is 13 ∗ 13, it is used to detect larger targets; when the feature size is 26 ∗ 26, it is used to detect medium-sized targets; and when the feature size is 52 ∗ 52, it is used to detect smaller targets. Therefore, it solves the problem of adjusting the detection network according to the size of the target [21].

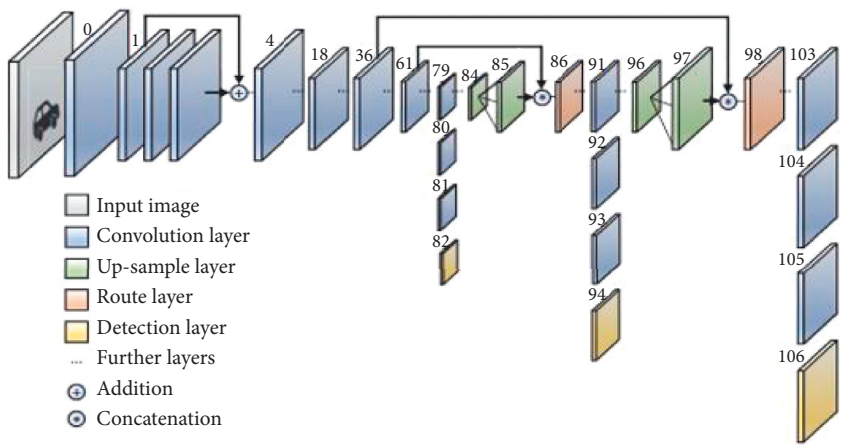

Figure 1: Network structure model of YOLOv3.

The detection steps of the three feature maps with different sizes in YOLOv3 are 32, 16, and 8. For the pictures with 416 ∗ 416 pixels, the first detection layer is located in the layer 82 of darknet-53 network. Because its detection step is 32, the feature map of this layer is a picture with a resolution of 13 ∗ 13. The second detection layer is located in the layer 94 of darknet-53 network. Because its detection step is 16, the feature map of this layer is a picture with a resolution of 26 ∗ 26. The third detection layer is located at layer 106 of darknet-53 network. Because its detection step is 8, the feature map of this layer is a picture with a resolution of 52 ∗ 52 [22].

2.2. Parameters of YOLOv3 Algorithm. Loss function is used to indicate the inconsistency between the predicted value and the real value in the model. The training model in the algorithm aims to reduce the value of loss function. The smaller its value is, the higher the robustness the model has. Loss function which is frequently used includes mean square difference loss function and cross entropy loss function [23].

The definition of loss function in the YOLOv3 algorithm is shown in formula (5), which is composed of three parts: L_{coord} refers to prediction error of bounding box coordinate, L_{conf} refers to confidence error of bounding box, and L_{class} refers to prediction error of target classification.

$$L = L_{\text{coord}} + L_{\text{conf}} + L_{\text{class}}. \tag{5}$$

The definition of L_{coord} is shown in formula (6). In the formula, λ_{coord} refers to the weight coefficient of coordinate error, S^2 indicates that there are S^2 numbers of grids in the picture, and B refers to the number of prediction bounding boxes of each grid. refers to the possibility that the j-th prediction box of the I-th grid contains targets. If targets are included, =1; otherwise =0. (x_i, y_i, w_i, and h_i), respectively, represents the abscissa, ordinate, width, and height values of the center point of the real bounding box in the i-th grid [24].

$$L_{\text{coord}} = \lambda_{\text{coord}} \sum_{i=0}^{S^2} \sum_{j=0}^{B} I_{ij}^{\text{obj}} \left[(x_i - \hat{x}_i)^2 + (y_i - \hat{y}_i)^2 + w_i - \hat{w}_i + \left(h_i - \hat{h}_i\right)^2 \right]. \tag{6}$$

The definition of L_{conf} is shown in formula (7). λ_{noobj} refers to the weight coefficient when the box does not contain targets target, and, respectively represent the real and predicted confidence. refers to the possibility that the j-th prediction box of the I-th grid does not contain targets. Other parameters in the formula have the same meaning as formula (6).

$$L_{\text{Conf}} = \sum_{i=0}^{S^2} \sum_{j=0}^{B} I_{ij}^{\text{obj}} \left[\left(C_i - \hat{C}_i\right)^2 \right] + \lambda_{\text{noobj}} \sum_{i=0}^{S^2} \sum_{j=0}^{B} L_{ij}^{\text{noobj}} \left[\left(C_i - \hat{C}_i\right)^2 \right]. \tag{7}$$

The definition of L_{class} is shown in formula (8). There are C types of targets to be detected ($c = 1, 2, 3, \ldots, C$), and, respectively represent the real and prediction probabilities of targets of c-th class in the i-th grid. The other parameters in the formula have the same meaning as formula (6).

$$L_{\text{class}} = \sum_{i=0}^{S^2} I_{ij}^{\text{obj}} \sum_{c \in \text{class}}^{S^2} \left[\left(P_i(C) - \widehat{P}_i(C)\right)\right]^2. \quad (8)$$

3. Proposed Method

Although the YOLOv3 algorithm is widely used in the field of real-time target detection, it is easy to be affected by external factors such as illumination, ground humidity, and so on. In order to improve the detection accuracy and speed, this paper improves the YOLOv3 algorithm, and the improved algorithm is more suitable for the lane line detection system.

3.1. Improvement of the Backbone. Firstly, in the conventional YOLOv3 algorithm, the backbone is Darknet-53, and the input image is divided into $s * s$ grids. When using the YOLOv3 algorithm for lane line detection, the shape feature of lane line image is that the transverse length is short and the longitudinal length is long. Therefore, in order to increase the grid detection density of image in the longitudinal direction, the algorithm is improved to divide the image into $s * 2S$ grids. This network structure is more suitable for the lane line detection system.

Secondly, under different road conditions, the size of lane line targets is different, which will result the poor effect of the detection algorithm. In order to solve this problem, the YOLOv3 algorithm is adjusted to four detection scales: $13 * 13$, $26 * 26$, $52 * 52$, and $104 * 104$. After the improvement, each detection scale not only obtains the detailed information of the bottom layer of the network but also can be predicted separately. The improved algorithm is more suitable for lane detection than the original lane detection system.

Finally, the YOLOv3 algorithm is implemented using Darknet-53 as the backbone for feature extraction. The down sampling operation is realized by convolution kernel, with the step size of 2 and the size of $3 * 3$. The receptive field of the network is large, but the spatial resolution of the network is insufficient. After extracting features through deep convolution, the information of small targets may be lost. As the detection of small targets such as lane line is more dependent on the shallow layer, Darknet-49 is used as the backbone of the algorithm.

There are 49 convolution layers and 5 residuals in Darknet-49. The activation function of ReLU may cause losses of low-dimensional feature information. So, linear activation function is used in the first convolution layer of Darknet-49 to reduce the loss of low dimensional information. Darknet-49 network performs 4 down sampling operations on the input image to obtain the characteristic images of 4 scales. The improved detection network expands the original three detection scales to 4 detection scales. Multiscale feature fusion can improve the detection performance. The improved detection network structure is shown in Figure 2.

3.2. Parameters of Anchor. In the process of target detection, the size of prediction boxes directly affects the accuracy and speed of the algorithm, which is a very important parameter in the algorithm. In the original YOLOv3 algorithm, the K-means clustering algorithm is used to obtain anchor parameters. In this method, different feature attributes in the distance center distance formula are treated with equal weight, without considering the differences of different feature attributes. Furthermore, the algorithm needs to estimate the K value which is the number of clusters by man-made. It has a certain subjectivity. In addition, if there are some noise points or isolated points in the sample, these points will have a great impact on the calculation results and cause serious deviation.

In the lane line detection system, in order to solve the problem of clustering center distance parameters, a method is proposed to replace the K-means clustering algorithm in the original algorithm with the intersection and union ratio of sample boxes and prediction boxes. The formula for calculating the parameters of anchor by this method is shown in formula (9). In the formula, parameter box is referred to the prediction box of the sample, parameter cen is referred to the clustering center, and IoU is referred to the area where the prediction box and the real box are combined.

$$D = \min \sum_{\text{box}=0}^{n} \sum_{\text{cen}=0}^{k} [1 - \text{IoU}]. \quad (9)$$

The detection results comparison between the improved method and the original YOLOv3 algorithm is shown in Table 1. Its average accuracy and speed are higher than those of the original YOLOv3 algorithm. It shows that the improved method of obtaining anchor parameters is more suitable for the detection of small targets such as lane lines.

3.3. Loss Function. The loss function is used to estimate the inconsistency between the predicted value and the real value in the model which is the basis for the evaluation of the false detection rate by the neural network and reflects the convergence performance of the network model. The loss function in the YOLOv3 algorithm consists of three parts, as shown in formula (5).

When calculating the loss function in the YOLOv3 algorithm, the boundary box coordinate prediction error, boundary box confidence error, and target classification prediction error are activated by logistic function. The function expression is shown in formula (10), and the derivative formula of the function is shown in formula (11).

$$f(x) = \frac{1}{1 + e^x}, \quad (10)$$

$$f'(x) = \frac{e^x}{2e^x + e^{2x} + e^{2x}\left(1/e^x\right)^2}. \quad (11)$$

The characteristic of logistic function is that it is single and continuous, and the function value is limited. So, the

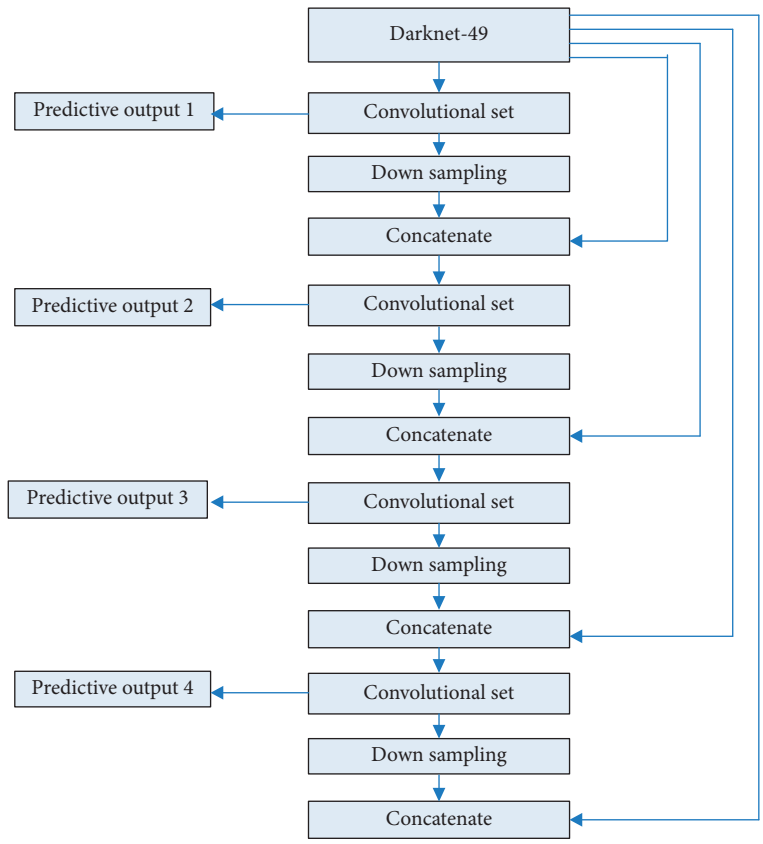

Figure 2: Improved network structure.

Table 1: Comparison of obtaining anchor parameters by different methods.

Methods	Anchor	Average accuracy (%)	Average speed (frame/s)
YOLOv3	(2, 8), (4, 10), (5, 14), (10, 24), (14, 33), (40, 89), (100, 283), (162, 320)	989.32	420.78
Improved algorithm	(3, 9), (6, 12), (8, 15), (12, 28), (20, 46), (49, 102), (113, 290), (185, 348)	991.56	443.21

data will not diverge during network transmission. The characteristic of the derivative of this function is that its value is less than 1. When the input value of the network is large, the derivative value will be very small, so the error of the calculated loss function will become large, and the convergence performance of the network model will become worse.

In order to solve the above problems, the focal loss function is proposed to replace the logistic function in the original algorithm. The expression of the focal loss function is shown in formula (12). In formula (12), p is the output value of the logistic function, $(1-p)^{\gamma}$ is the adjustment factor of the network system, α is the weight coefficient of the target category $(0 \le \alpha \le 1)$, γ is the focusing coefficient$(\gamma \ge 0)$, and y is the predicted probability value of the tag.

$$\mathrm{FL}(p, y) = -\alpha y (1-p)^{\gamma} \lg p - (1-\alpha)(1-y) p^{\gamma} \lg(1-p), \tag{12}$$

$$L_{\mathrm{coord}} = \lambda_{\mathrm{coord}} \sum_{i=0}^{S^2} \sum_{j=0}^{B} I_{ij}^{\mathrm{obj}} \left[\mathrm{FL}\left(x_i, \hat{x}_j\right) + \mathrm{FL}\left(y_i, \hat{y}_j\right)\right] + \lambda_{\mathrm{coord}} \sum_{i=0}^{S^2} \sum_{j=0}^{B} I_{ij}^{\mathrm{obj}} \left[\mathrm{FL}\left(w_i, \hat{w}_j\right) + \mathrm{FL}\left(h_i, \hat{h}_j\right)\right], \tag{13}$$

$$L_{\text{conf}} = \sum_{i=0}^{S^2} \sum_{j=o}^{B} I_{ij}^{\text{obj}} \left[\text{FL}\left(C_i, \widehat{C}_j\right)\right] + \lambda_{\text{noobj}} \sum_{i=0}^{S^2} \sum_{j=o}^{B} I_{ij}^{\text{noobj}} \left[\text{FL}\left(C_i, \widehat{C}_j\right)\right], \tag{14}$$

$$L_{\text{class}} = \sum_{i=0}^{S^2} I_{ij}^{\text{obj}} \sum_{c=\text{class}}^{S^2} \left[\text{FL}\left(P_i(C), \widehat{P}_i(C)\right)\right]. \tag{15}$$

The boundary boxes coordinate prediction error, boundary boxes confidence error, and target classification prediction error of the improved loss function are shown in formulas (13)–(15), respectively. After adopting the improved adjustment factor, the reception range of small targets such as lane line is effectively increased and the detection accuracy is improved.

3.4. Automatic Lane Line Detection System. Based on the improved YOLOv3 algorithm network structure, the lane line detection system is mainly composed of data preparation module, learning and training module, and lane line detection module. The implementation process is shown in Figure 3.

The main work of data preparation module includes the collection, marking, screening, and preprocessing of lane line samples. The sample collection method is to install a high-definition camera on the car and take lane line photos on the way. Data marking refers to marking lane lines in the picture, including white solid line, white dotted line, yellow solid line, yellow dotted line, and other lane lines. The main work in the screening and preprocessing stage is to select high-quality pictures from the marked pictures and preprocess them into the format required by YOLOv3. The nearest neighbor down sampling method is used as the main method of picture preprocessing.

The flow chart of the nearest neighbor down sampling algorithm is shown in Figure 4. Firstly, the coordinates of each pixel in the final picture should be traversed. Then, we use the nearest neighbor interpolation method to convert it into the corresponding coordinates in the final image. It is converted according to formula (16). In formula (16), is the RGB value at the coordinate (x, y) in the final image, $s(x, y)$ is the RGB value at the coordinate (x, y) in the original image, and int refers to the rounding operation.

$$t\left(x', y'\right) = s\left(\text{int}\left(x + 0.5\right), \text{int}\left(y + 0.5\right)\right). \tag{16}$$

The processed images are sent to the improved YOLOv3 algorithm network for lane line feature extraction. The four features of lane line are extracted at layers 67, 75, 89, and 97 of the network, and the features are sent to the YOLO layer for training. When the specified number of training times is reached, the iterative process is stopped. Then, the final detection model is generated, and the learning and training are completed. Finally, the lane line images are sent into the trained detection model, and the system can output the lane line detection results.

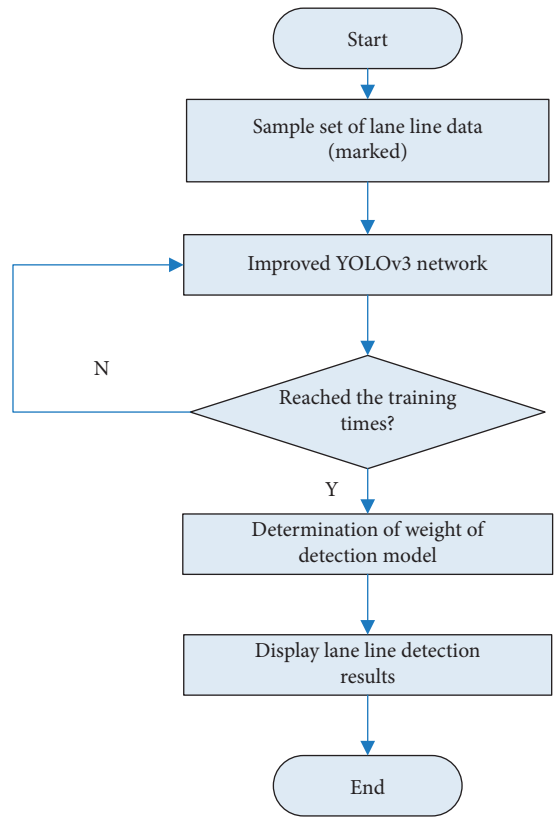

Figure 3: Process of the lane line detection system.

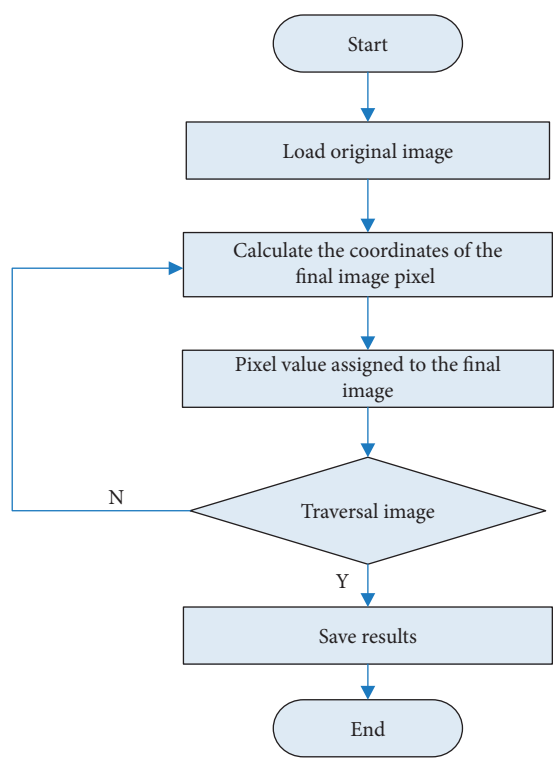

Figure 4: Flow chart of the nearest neighbor down sampling algorithm.

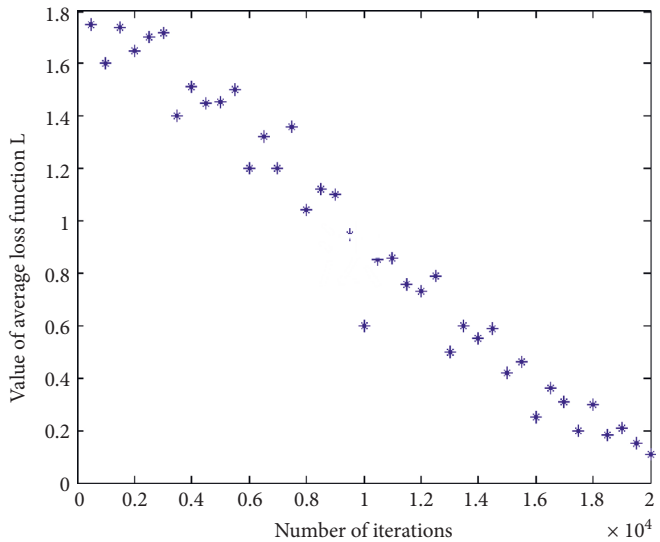

Figure 5: Variation trend of average loss function value.

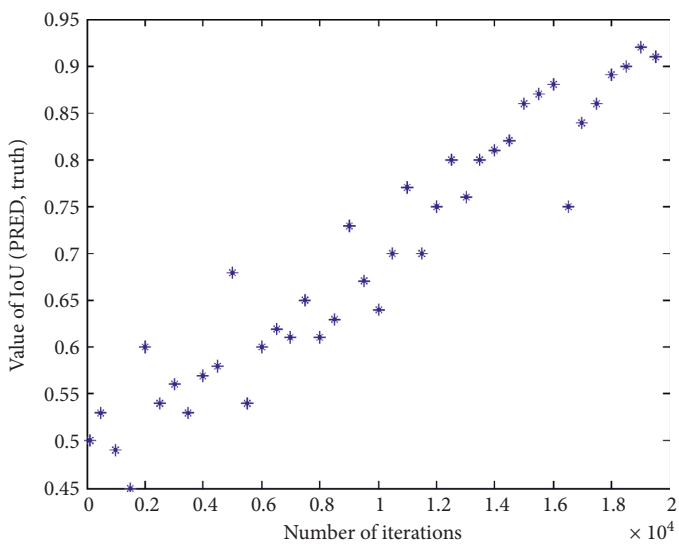

Figure 6: Change trend of matching degree value.

4. Results and Discussion

4.1. Experimental Environment. In the experiment, the hardware environment used is Intel® Core™-i7 4720HQ 2.6 GHz CPU and Nvidia TITAN *X* 12 GB VRAM GPU. The corresponding hardware environment is running under Ubuntu OS.

4.2. Experimental Dataset. Karlsruhe Institute of Technology and Toyoko Technological Institute (KITTI) is a commonly used traffic dataset and includes scenes, such as sunny, cloudy, highway, and urban roads. The scenes are increased under complicated working conditions, such as rain, tunnel, and night, to ensure coverage. In this experiment, KITTI is used as the dataset. A total of 500 photos of urban routes were selected, including 400 learning samples and 100 test samples.

4.3. Experimental Results and Analysis. The marked lane line pictures are sent to the improved YOLOv3 algorithm network for training. In the training stage, the size of the pictures used is 416 ∗ 416 pixels. During the training process, several important index parameters in the algorithm are dynamically recorded.

The change process of the average loss function L value is shown in Figure 5. It can be seen from Figure 5 that at the beginning of training, the loss function value is about 1.8. When the number of training increases, the convergence of the loss function value decreases. When the number of iterations is about 20000, the loss value is about 0.1. The loss function L has achieved the expected effect.

The change process of IoU (Pred, Truth) is shown in Figure 6. It can be seen from Figure 6 that at the beginning of training, value of IoU (Pred, Truth) is 0.5. When the number of training increases, it also increases gradually. When the

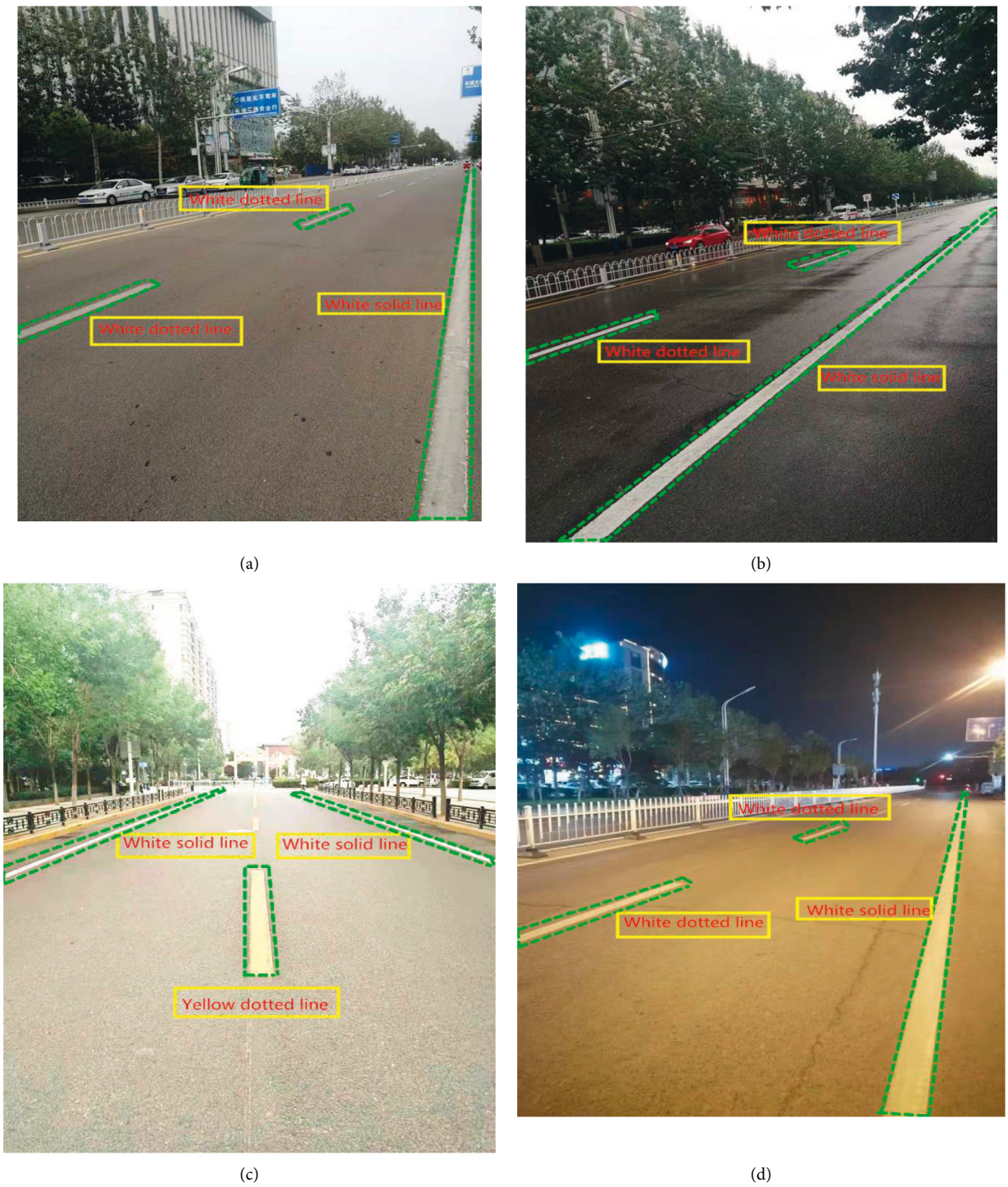

(a) (b) (c) (d)

Figure 7: Results in different scenes: (a) normal illumination; (b) rainy days; (c) bright light; (d) dark light at night.

number of iterations reaches 20000, value of IoU (Pred, Truth) is about 0.93. The detection accuracy has achieved the expected effect.

According to the value of average loss function L, value of IoU (Pred, Truth), and other parameters, the training times of the model are set to 20000. After the sample learning and training, 100 lane line photos are tested, and the system can automatically identify the lane lines in the pictures. The test results of the system in different scenes are shown in Figure 7.

4.4. Comparison of Different Algorithms. The automatic lane line detection system based on improved YOLOv3 has good performance in detection accuracy, detection time, missed detection rate, and so on. The performance parameters of

Table 2: Comparison of test performance of different algorithms.

Algorithm	FPS	mAP (%)	Times of iterations when $L = 0.1$	Average missed detection rate (%)
YOLO v3	8	84.87	20922	2.4
R-CNN	6	87.35	22178	4.2
Fast R-CNN	10	86.27	21896	8.1
Faster R-CNN	11	80.73	19989	9.3
YOLOP	11	81.04	20012	4.9
Improved YOLOv3	12	91.03	19985	1.1

different algorithms are shown in Table 2. It can be seen that the performance of the lane line detection system of the improved YOLOv3 model is better than that of the other algorithms in all aspects.

5. Conclusion

Aiming at the problem that the traditional lane detection algorithms cannot balance detection accuracy and detection speed, a detection system based on the improved YOLOv3 algorithm is proposed in this paper.

The main improvements include

(1) According to the characteristics of inconsistent vertical and horizontal distribution density of lane line images, it is proposed to divide the images into $s * 2S$ grids to improve the vertical detection density

(2) The detection scale is adjusted to four detection scales: $13 * 13$, $26 * 26$, $52 * 52$, and $104 * 104$, which is more suitable for the detection of small targets such as lane lines

(3) The YOLOv3's backbone is changed by adopting Darknet-49 architecture, which simplifies the network and improves the system performance

(4) The parameters such as cluster center distance and loss function are improved, which are more suitable for lane line detection system

The experimental results show that the improved algorithm has good detection performance when detecting flat roads, but when the roads have large slopes, the detection is easy to be affected. Therefore, solving the problem of lane line detection in large slope scenes will be the focus of the further study.

Data Availability

No data were used to support this study.

Conflicts of Interest

The authors declare that there are no conflicts of interest.

Acknowledgments

This work was supported by Basic Scientific Research Project in Hebei Province (Nos. 2021QNJS13 and 2021QNJS06) and by Project of Zhangjiakou science and Technology Bureau (No. 1911002B).

References

[1] H. G. Zhu, "An efficient lane line detection method based on computer vision," *Journal of Physics: Conference Series*, vol. 1802, Article ID 032006, 2020.

[2] R Xia, Y. Chen, and B. Ren, "Improved anti-occlusion object tracking algorithm using unscented rauch-tung-striebel smoother and kernel correlation filter," *Journal of King Saud University - Computer and Information Sciences*, vol. 18, no. 3, pp. 22–30, 2022.

[3] C. Y. Fu, W. Liu, and A. Ranga, "Deconvolutional single shot detector," 2021, https://arxiv.org/abs/1701.06659.

[4] T. Lin, P. Dollár, R. B. Girshick, K. He, B. Hariharan, and S. J. Belongie, "Feature pyramid networks for object detection," in *Proceedings of the 2017 IEEE Conference on Computer Vision and Pattern Recognition (CVPR)*, pp. 936–944, Honolulu, HI, USA, July 2021.

[5] S. Lee, J. Kim, and I. S. Kweon, "VPGNet: vanishing point guide network for lane and road marking detection and recognition," in *Proceedings of the International Conference on Computer Vision*, pp. 2380–7504, Venice, Italy, March 2021.

[6] A. Gupta and A. Choudhary, "A framework for camera-based real-time lane and road surface marking detection and recognition," *IEEE Transactions on Intelligent Vehicles*, vol. 3, no. 4, pp. 476–485, 2018.

[7] T. Lin, M. Maire, S. J. Belongie et al., *Microsoft Coco: Common Objects In Context" (Eccv)*, Springer, Berlin, Germany, 2019.

[8] R. B. Girshick, "Fast RCNN," in *Proceedings of the 2015 IEEE International Conference on Computer Vision (ICCV)*, pp. 1440–1448, Washington, DC, USA, December 2020.

[9] N. Dalal and B. Triggs, "Histograms of oriented gradients for human detection, computer vision and pattern recognition,"vol. 1, pp. 886–893, in *Proceedings of the IEEE Computer Society Conference on 2021 CVPR*, vol. 1, pp. 886–893, IEEE, Seattle, WA, USA, June 2021.

[10] X. Zhang, W. Yang, X. L. Tang, and J. Liu, "A fast learning method for accurate and robust lane detection using two-stage feature extraction with YOLO v3," *Sensors*, vol. 18, no. 12, p. 4308, 2018.

[11] J. Redmon and A. Farhadi, "YOLO9000:better,faster,-stronger," in *Proceedings of the 2017 IEEE Conference on Computer Vision and Pattern Recognition, CVPR*, pp. 7263–7271, IEEE, Honolulu, HI, USA, July 2017.

[12] J. Redmon and A. Farhadi, "YOLOv3: an incremental improvement," 2018, https://arxiv.org/abs/1804.02767.

[13] F. C. Soon, H. Y. Khaw, J. H. Chuah, and J. Kanesan, "Vehicle logo recognition using whitening transformation and deep learning," *Signal, Image and Video Processing*, vol. 13, no. 1, pp. 111–119, 2019.

[14] M. Tan, R. Pang, and Q. V. Le, "Efficientdet: scalable and efficient object detection," in *Proceedings of the IEEE/CVF Conference On Computer Vision And Pattern*

Recognition(CVPR), pp. 202010781–202010790, Seattle, WA, USA, June 2020.

[15] C. F. Olson, "Constrained hough transforms for curve detection," *Computer Vision and Image Understanding*, vol. 73, no. 3, pp. 329–345, 2021.

[16] Q. Zou, H. Jiang, Q. Dai, Y. Yue, L. Chen, and Q. Wang, "Robust lane detection from continuous driving scenes using deep neural networks," *IEEE Transactions on Vehicular Technology*, vol. 69, no. 1, pp. 41–54, 2020.

[17] W. Y. Ming, Q. J. Cheng, and H. Yang, "Aerial image location of unmanned aerial vehicle based on Yolo v2," *Laser and Optoelectronics Progress*, vol. 54, no. 11, pp. 101–110, 2019.

[18] W. Ming, J. Quan, and Y. Q. Hou, "Research on unmanned aerial image location based on Yolo v2," *Progress in laser and optoelectronics*, vol. 54, no. 11, 2017.

[19] S. Ren, K. He, R. Girshick, and J. Sun, "Faster R-CNN: towards real-time object detection with region proposal networks," *IEEE Transactions on Pattern Analysis and Machine Intelligence*, vol. 39, no. 6, pp. 1137–1149, 2017.

[20] J. Redmon and A. Farhadi, "YOLOv3: an incremental improvement," in *Proceedings of the Conference on Computer Vision and Pattern Recognition(PCCV)*, pp. 1–4, Salt Lake City, UT, USA, July 2018.

[21] A. Karpathy and J. Johnson, "Neural networks part 3: learning and evaluation," *Cs231n Convolutional Neural Network For Visual Recognition*, vol. 25, no. 4, pp. 986–998, 2019, http://cs231n.github.io/neuralnetworks-3.

[22] J. Walsh, "Deep learning vs. traditional computer vision," in *Proceedings of the Computer Vision Conference (CVC)*, Las Vegas, NA, USA, April 2019.

[23] C. Li, D. Song, R. Tong, and R. Min, "Illumination-aware faster RCNN for robust multispectral pedestrian detection," *Pattern Recognition*, vol. 85, pp. 161–171, 2019.

[24] X. Wang, M. Seyf, and M. Chen, "Face detection using small-scale convolutional neural network (CNN) modules for embedded systems," U.S. Patent 10,268-947, 2019.

Hindawi
Journal of Electrical and Computer Engineering
Volume 2022, Article ID 5984969, 15 pages
https://doi.org/10.1155/2022/5984969

Research Article

Bidirectional Quadratic Converter-Based PMBLDC Motor Drive for LEV Application

Mukesh Kumar,[1] **Kalpana Chaudhary**,[1] **R. K. Saket**,[1] **and Baseem Khan**[2]

[1]*Department of Electrical Engineering, Indian Institute of Technology (BHU), Varanasi, India*
[2]*Department of Electrical and Computer Engineering, Hawassa University, Hawassa, Ethiopia*

Correspondence should be addressed to Baseem Khan; baseem.khan04@gmail.com

Received 4 November 2021; Revised 20 December 2021; Accepted 30 December 2021; Published 17 January 2022

Academic Editor: Hamdy Soltan

In this study, a bidirectional DC-to-DC quadratic converter (BDQC) is designed and developed for the motoring and regenerative braking (RB) of a permanent magnet brushless DC (PMBLDC) motor for a light electric vehicle (LEV) application. A PMBLDC motor is deemed more suitable for an electric vehicle (EV) due to its high efficiency and torque density. In the present work, a BDQC of 1 kW is designed to drive a 1.1 HP PMBLDC motor through a conventional voltage source inverter (VSI). An EV's load cycle is emulated using a highly inertial load driven by a PMBLDC motor during the converter's boost mode operation. RB is a crucial factor in extending the driving range of EVs by efficiently utilizing battery power. The converter operates in buck mode during RB, and simultaneously, the back electromotive force (EMF) of the PMBLDC machine is boosted by the self-inductance of the PMBLDC motor and the VSI. The braking technique used in this work eliminates the traditional drawback of RB in buck mode, as the power is extracted even when the motor's back EMF is lower than the battery's voltage. The control strategy has been implemented using the TMS320F28335 DSP controller for a developed converter prototype of the converter and driving the PMBLDC motor. The experimental results are compared to the simulation results, and a good alignment has been found.

1. Introduction

In recent years, electric vehicles (EVs) have drawn more attention as a substitute for conventional internal combustion engine (ICE) vehicles. With the advancement of batteries and motors, EVs have become an optimistic substitute for ICE vehicles. Due to its high efficiency and controllability, the PMBLDC motor is the most popular option in the drive train of low-to-medium power EVs. In the past decade, to improve the drivetrain's efficiency, research on bidirectional DC-to-DC converters (BDCs) for EV applications has been extensively done [1–5]. The problem with these BDCs is that they have a large number of component requirements and high voltage stress on the switches. The leakage inductance of the transformer also causes high voltage stress on the switches. Different types of nonisolated and isolated bidirectional DC-DC converters have been introduced. A half-bridge type converter with more components, high voltage stress on switches, and a high-frequency transformer is used [6]. A full-bridge type converter with low voltage gain, a large number of power switches, and a transformer are required for isolation [7, 8]. The leakage inductance of the transformer causes high voltage stress on switches. Another isolated converter of full-bridge with flyback snubber has high voltage gain, but two transformers are used, which have leakage inductance. Leakage inductance causes high voltage stress on switches [9]. A clapping circuit is used to reduce the voltage and current stress. The converter becomes more complex and difficult to control. Recently, a different type of nonisolated double boost-flyback converter has been proposed in [10, 11]. The voltage gain is high in a double boost converter, but it requires two coupled inductors, and there is no common ground between input and output.

The various nonisolated bidirectional DC-to-DC converters have been compared based on their performance

[12, 13]. The voltage gain of the converter is two times that of a conventional buck-boost converter. A modified non-isolated BDC for improved performance and efficiency is presented in [14, 15]. In this case, the efficiency is improved, but the voltage gain is the same as with the conventional buck-boost converter. The study on the bidirectional power flow using the VSI was done in [16–18]. The converter requires a large number of power switches and imposes high voltage stress on the switches. A three-port DC-DC converter based on quadratic boost operation for stand-alone PV/battery systems is presented [19]. Recent research focuses on the modified converters because they are non-isolated (transformerless) topologies. Therefore, the converter's size, weight, and cost are reduced as presented in [20, 21]. The quadratic converters have high voltage gain, thereby having more efficiency than conventional ones [22–24]. Regenerative braking can be achieved by reversing power flow from the battery to the PMBLDC motor. It can be done even at low back EMF by boosting it using the self-inductance of the PMBLDC motor by controlling the switches of VSI described in [25, 26]. The back EMF boost is controlled by switches using a hall sensor. The signal from the hall sensor will give the information for the switches to be ON or OFF.

The electrical system of a powertrain configuration for an EV is shown in Figure 1. The magnitude and direction of the power are controlled by the BDQC. Controlled electrical power flows between the battery and the PMBLDC motor. The BDQC operates in two modes: motoring (boost) and regenerative braking (buck) mode. In the motoring mode, electrical power flows from the battery to the PMBLDC motor through VSI. Simultaneously, the kinetic energy of the PMBLDC motor is converted into electrical energy and fed back to the battery through the bidirectional VSI during regenerative braking. In turn, a converter with fewer components has lower losses and is needed to fulfill the requirements of high efficiency and significant voltage gain in EVs. A comparison of different bidirectional converters with different parameters is given in Table 1.

The presented nonisolated BDQC has a simple topology, control strategy, and a large voltage gain, which ensures wide voltage range operation when compared to conventional bidirectional buck or boost converters. The topology of the BDQ buck-boost converter is shown in Figure 2. Four switches with antiparallel diodes have been implemented in this BDC. The number of components can be reduced by using the back diodes of the MOSFETs [27]. A battery with a voltage of V_i is connected on the low voltage side, and the DC link, or the motor side voltage, is V_o. The inductor in series with the battery is L_1, and the inductor in the middle is L_2. The capacitor in the center is C_1, while the DC link capacitor is C_2.

In this work,

(i) An efficient regenerative technique with the help of the self-inductance of the PMBLDC motor is presented

(ii) An optimum switching technique is employed for operating the converter at reduced switching losses

(iii) A back EMF boosting technique is used to extract power even at low motor speed

(iv) The developed system's designing, simulation, and hardware validation are performed

This study describes the BDQC operation in motoring and regenerative braking modes. The motoring mode of operation is discussed in Section 2, and the regenerative braking mode of operation is given in Section 3. The design parameters of the converter are presented in Section 4. Simulation results and validation results through a developed prototype are explained in Sections 5 and 6, respectively. The conclusion is made in Section 7.

2. Motoring Mode of Operation

The converter is designed to operate in the continuous inductor current mode (CICM) in steady-state as well as in low load conditions. The capacitors C_1 and C_2 are sufficient to maintain a steady voltage during one period of switching (T_s). In motoring mode operation, the switches S_1 and S_4 are OFF, switch S_3 is always turned ON to avoid switching losses, and switching of switch S_2 is controlled with PWM to execute the boosting operation. The following two modes can explain the converter's motoring (boost) mode operation.

2.1. Mode 1 (0, T_{on}). The switches S_2 and S_3 are ON for time intervals 0 to DT_S, and S_1 and S_4 are OFF. In this mode, the energy stored in the capacitor C_1 is transferred to the inductor L_2, and the battery voltage V_i charges the inductor L_1, as shown in Figure 3.

2.2. Mode 2 (T_{on}, T_s). In this mode, S_3 is ON, and the rest three switches are OFF for time interval (1-D)T_s. During this mode, the inductor L_2 transfers its stored energy to the DC link capacitor C_2, and capacitor C_1 is being charged by inductor L_1, as shown in Figure 4. The converter's boost mode operating principle in steady-state is shown in Figure 5.

For these two modes of boost operation, the volt-sec balance principle across inductors L_1 and L_2 with C_1 at voltage V_{c1} yields the following equations:

$$DT_sV_i + (1-D)T_s(V_i - V_{c1}) = 0, \quad (1)$$

$$DT_sV_{c1} + (1-D)T_s(V_{c1} - V_o) = 0. \quad (2)$$

By eliminating V_{c1} from (1) and (2), the voltage gain in boost mode is obtained as

$$\frac{V_o}{V_i} = \frac{1}{(1-D)^2}, \quad (3)$$

where $D = T_{on}/T_s$ is the duty ratio, and the quadratic nature of the converter can be inferred from (3).

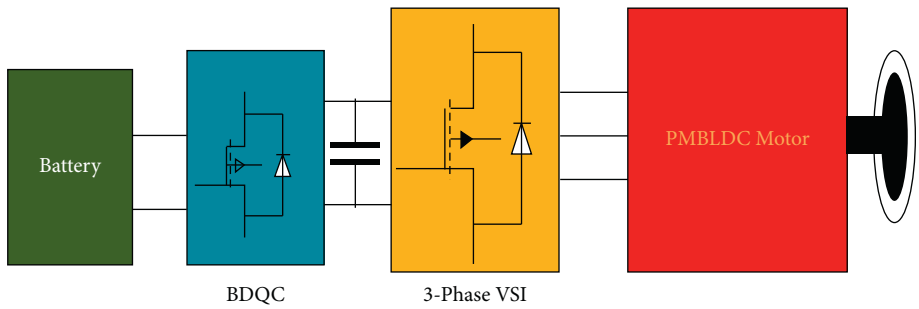

Figure 1: Schematic of the electrical system of the powertrain in EVs.

Table 1: Comparison of different bidirectional converters.

Converter	Component count	Voltage ratio step-up	Voltage ratio step-down	Voltage stress on power switches	Efficiency (%)
Converter in 1	3 inductors, 5 capacitors, 5 power switches	$2 + D/1 - D$	$D/3 - D$	$(1 + M)V_H/3M$ $2(1 + M)V_H/3M$, where $M = V_H/V_L$	96.67
Converter in 3	1 inductor, 1 transformer, 3 capacitors, 6 power switches	$N/(1 - D)^2$ $N = N1/N2$	$(1 - D)^2/N$	$(-D)V/N$ V/N $(NV)/(1 - D)^2$	95.4
Converter in 5	2 inductors, 1 transformer, 2 capacitors, 9 power switches	$nV_L/(1 - 2D_{ST})$		$V_L/(1 - 2D_{ST})$	97
Converter in 15	1 inductor, 3 capacitors, 4 power switches	$2/1 - D$	$D/2$	-----	92.5
BDQC	2 inductors, 2 capacitors, 4 power switches, 2 power diodes	$1/(1 - D)^2$	D^2	$V_i/1 - D$ $V_i/(1 - D)^2$	95.4

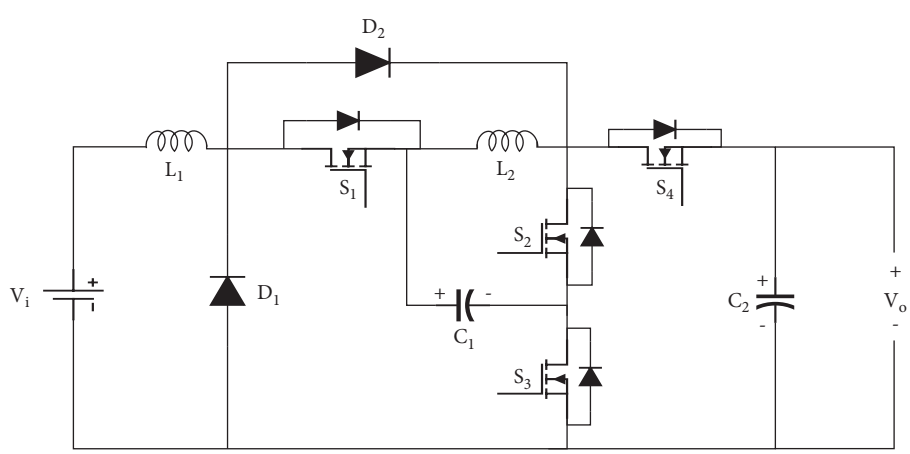

Figure 2: Bidirectional DC-DC quadratic converter.

3. Regenerative Braking Mode of Operation

The converter's braking (buck) mode is employed to perform RB, and this allows the mechanical energy stored in the inertial load and the rotor of the PMBLDC motor to be transferred back to the source. In the braking (buck) mode operation, the switches S_1 and S_4 are controlled with PWM simultaneously. The switches S_2 and S_3 are OFF throughout this mode of operation. The braking (buck) mode can be described in two stages of operation. These operations have been explained briefly in subsequent subsections.

3.1. Mode 1 (0, T_{on}). S_1 and S_4 are ON for the time interval 0 to DT_s in mode 1 of the buck operation. During this time interval, current in L_1 and L_2 increases, as inductors are being charged by capacitors C_1 and C_2, respectively, as shown in Figure 6.

3.2. Mode 2 (T_{on}, T_S). All the switches S_1, S_2, S_3, and S_4 are OFF for the time interval (1-D)Ts. The stored energy of inductor L_1 is transferred to the battery at voltage V_i and energy of inductor L_2 to capacitor C_1. The load at voltage V_o

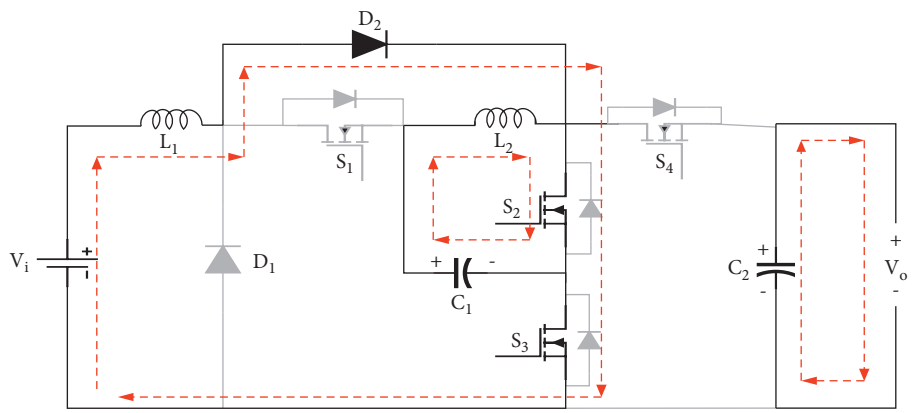

Figure 3: Converters' boost mode operation in mode 1.

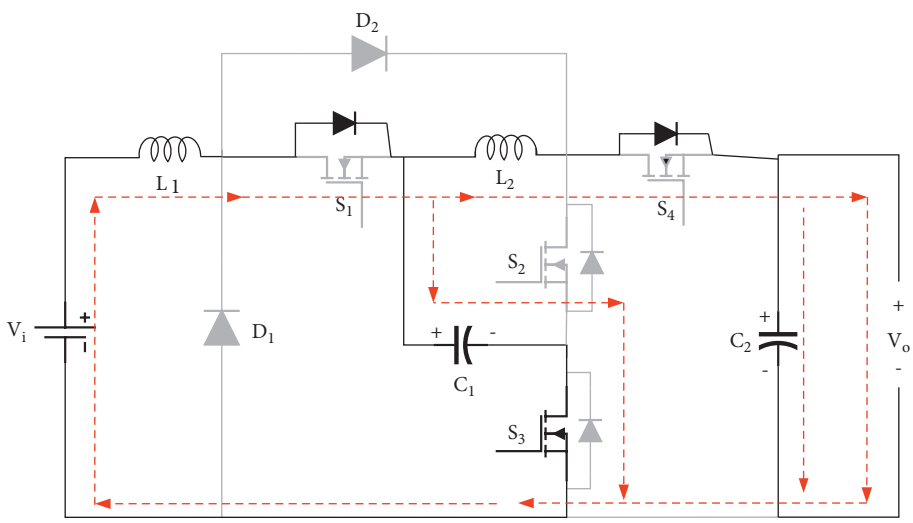

Figure 4: Converters' boost mode operation in mode 2.

is feeding the regenerated energy to capacitor C_2, as shown in Figure 7.

The waveforms of inductor currents and voltages are shown in Figure 8. For these two modes of operation, the voltage across the capacitor C_1 is assumed as V_{c1}.

The volt-sec balance principle across the inductors L_1 and L_2 gives the following equations:

$$DT_s(V_{c1} - V_i) + (1 - D)T_s V_i = 0, \tag{4}$$

$$DT_s(V_{c1} - V_o) + (1 - D)T_s V_{c1} = 0. \tag{5}$$

By eliminating V_{c1} from (4) and (5), the converter gain is obtained as a function of D as follows:

$$\frac{V_i}{V_o} = D^2. \tag{6}$$

(6) shows that the converter buck mode voltage gain is quadratic in nature.

3.3. Working of VSI during Regenerative Braking. In the RB (buck) mode, energy flow from the PMBLDC motor to the battery is required. Only by controlling the converter, the mechanical energy cannot be transferred from the PMBLDC motor, and the motor needs to be operated in the second quadrant. Instead of direct rectification, a back EMF boosting technique is applied in this work during regenerative braking.

The self-inductances of the PMBLDC motor are charged by shorting all the three phases together. The stored energy in these inductances is transferred to the converter's output capacitor (C_2) by turning OFF all switches of VSI. A flow diagram showing the converter operation based on the driver's on-road decision is shown in Figure 9. The equivalent circuit of the two active phases of the VSI during regenerative braking is shown in Figure 10. The back EMF, armature current of the PMBLDC motor, and switching signal of VSI are shown in Figure 11.

4. Converter Design

The converter design is done as per the boost and buck operations, as shown in Figure 5 and Figure 8. The designed converter is thus operated in the CICM, and the output

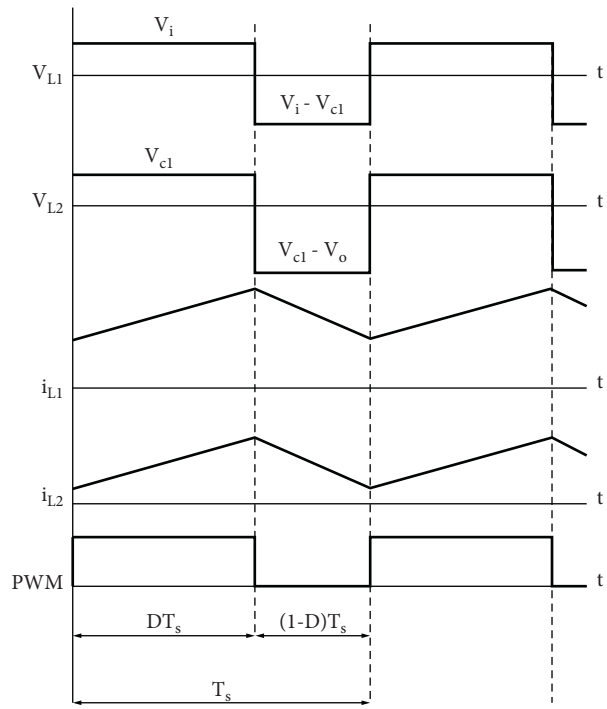

Figure 5: Converter's buck mode operation, mode 2.

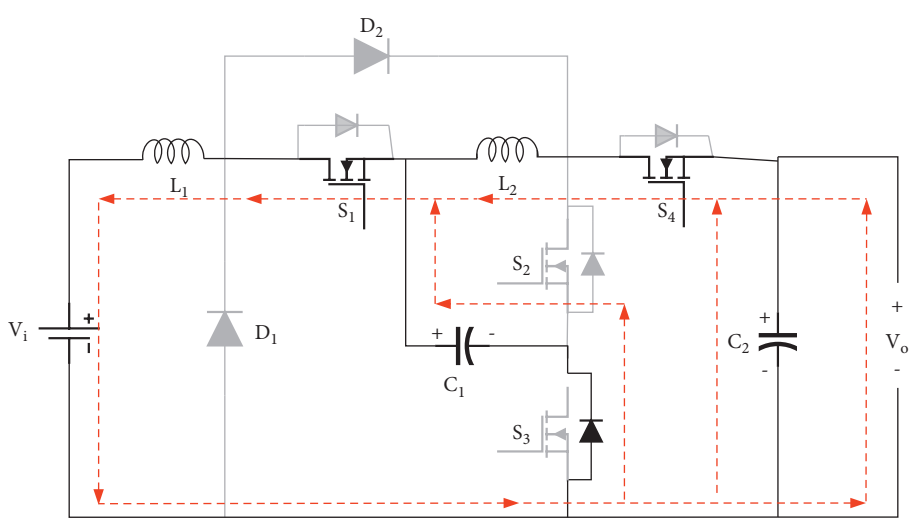

Figure 6: Convers' buck mode operation in mode 1.

capacitor value is selected for minimum output voltage ripple.

The converter is designed as per the designated parameters given in Table 2. The lithium nickel manganese cobalt (Li-NMC) battery is used for the experiment, whose parameters are given in Table 3. The inductor values are calculated to keep the converter in CICM operation even at low load conditions. The duty ratio (D) is calculated as 30% for an output voltage of 98 V with an input battery voltage of 48 V. The switching frequency (f_s) of the converter is 15 kHz.

The minimal load for the PMBLDC motor constitutes the switching losses in VSI, copper, iron, and windage losses. Thus, a minimal burden of 40 W is considered for calculations.

$$V_{co} = V_o = \frac{V_i}{(1-D)^2}, \tag{7}$$

$$V_i \times I_{L1} = V_o \times I_o. \tag{8}$$

No-load power = 40 W.

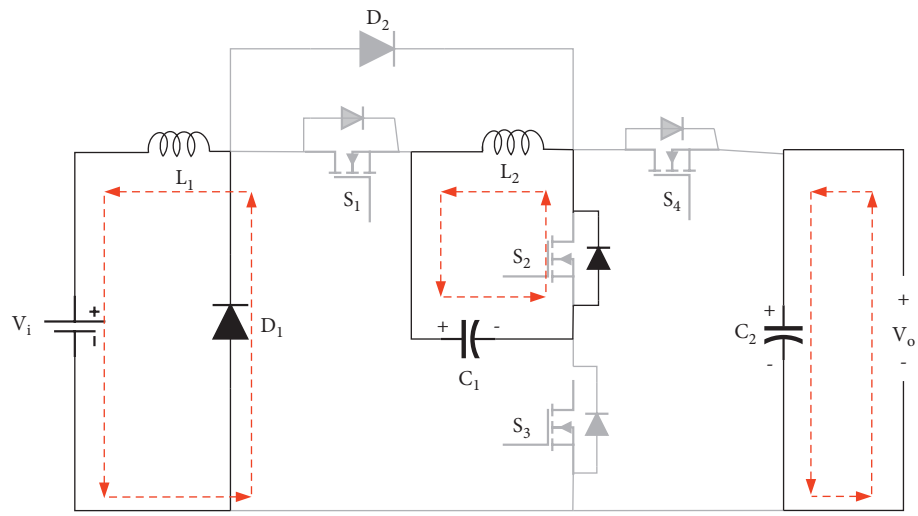

Figure 7: Converter buck mode operation in mode 2.

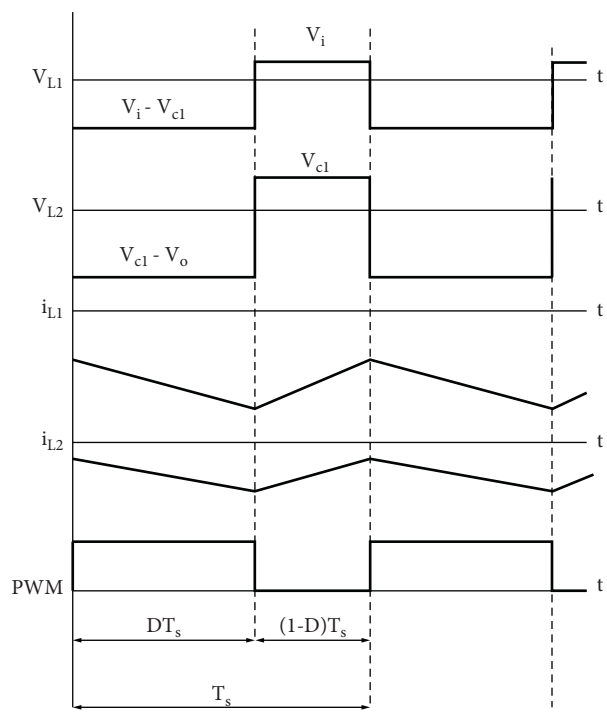

Figure 8: Converter's voltage and current waveform in buck mode.

$$I_{L1} = \frac{P_{\min}}{V_i} = 0.8A, \tag{9}$$

$$\Delta I_{L1} = 1.6A, \tag{10}$$

$$V_i = L_1 \times \frac{\Delta I_{L1}}{DT_s}. \tag{11}$$

From (11), the value of input inductor L_1 is calculated as 0.6 mH. Thus, for CICM operation, a higher value of inductance, i.e., 1 mH, is selected in this work. The calculation for L_2 is done as follows:

$$I_{L1} = \frac{I_o}{(1-D)^2}, \tag{12}$$

$$I_{L2} = \frac{I_o}{(1-D)}. \tag{13}$$

The calculated value of I_{L2} at minimum load is 0.56 A. Thus, the current ripple at boundary condition is 1.12 A.

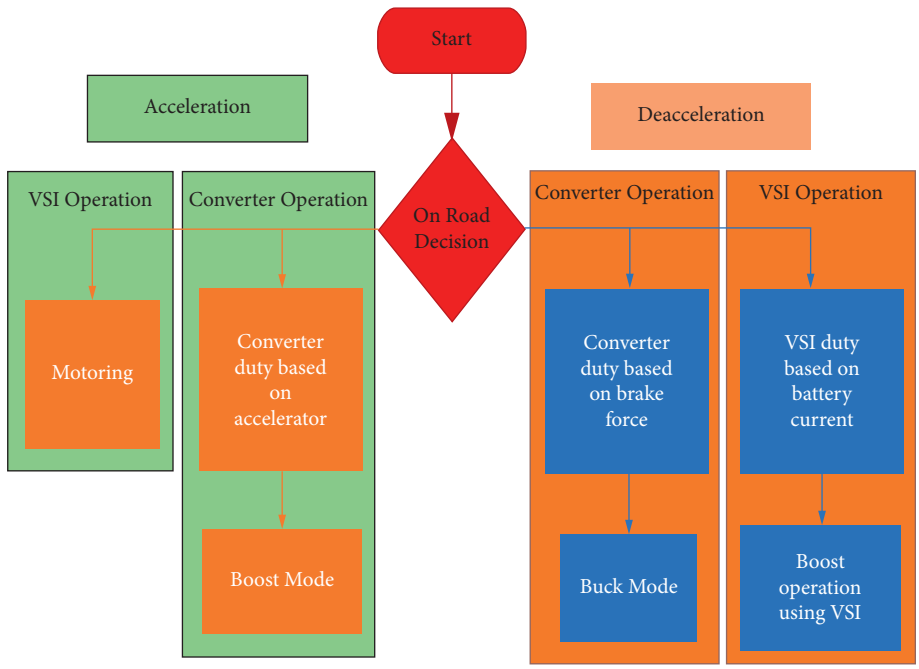

Figure 9: Flow diagram of the converter operation in EV.

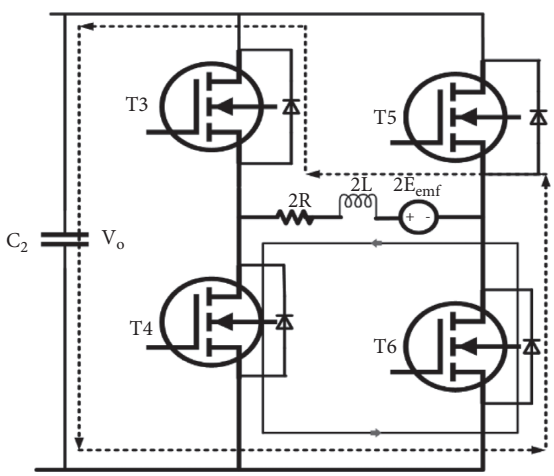

Figure 10: Equivalent circuit of two active phases of VSI during regenerative braking.

$$V_{C1} = \frac{V_i}{1-D}, \tag{14}$$

$$V_{c1} = L_2 \times \frac{\Delta V_{L2}}{DT_s}. \tag{15}$$

The value of inductor L_2 is calculated using (15) as 1.2 mH. Thus, for CICM operation, a higher value of inductance, i.e., 1.5 mH, is selected in this work. The calculation for C_1 is as follows:

$$I_c = C_1 \times \frac{dV_{c1}}{dt}, \tag{16}$$

$$I_c = -I_{L2}, \tag{17}$$

$$I_{L2} = C_1 \times \frac{\Delta V_{c1}}{DT_s}. \tag{18}$$

Taking $\Delta V_{C1} = 10\%$ of V_{C1}, the value of capacitor C_1 is calculated as 43 μF. The readily available capacitor of 47 μF is selected in this work.

$$I_{co} = C_2 \times \frac{dV_{co}}{dt}, \tag{19}$$

$$I_{L2} - I_o = C_2 \times \frac{\Delta V_{co}}{(1-D)T_s}. \tag{20}$$

For $\Delta V_{co} = 2\%$ of V_{co} and $f_s = 15$ kHz, the value of C_2 is calculated as 102 μF. The commercially available capacitor with a higher value of 220 μF is selected for this work. The calculated values of passive components in buck mode of operation are lower than that of boost mode operation. Thus, for the CICM operation of the converter, the boost mode values of passive components are selected for converter design.

The voltage stresses on switches S_1, S_2, and S_4 are calculated as

$$V_{S1} = \frac{V_i}{1-D},$$

$$V_{S2} = V_{S4} = \frac{V_i}{(1-D)^2}. \tag{21}$$

The voltage stress on switches is low as compared to the converter in [1, 3].

With the help of equations (7)–(20) and the value of V_i, V_o, and I_o, all parameters, i.e., L_1, L_2, C_1, and C_2 can be calculated. The calculated parameters of the converter are given in Table 4.

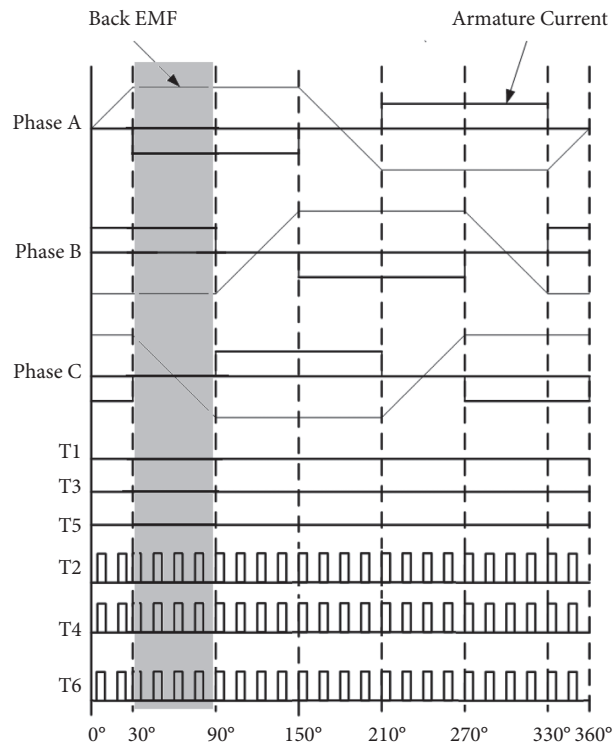

Figure 11: Switching signal of VSI during regenerative braking.

Table 2: Design parameters.

Parameter	Value
Input voltage (V_i)	48 V
Output power (P_o)	10^3 W
Output voltage (V_o)	98 V
Operating frequency (f_s)	15 kHz

Table 3: Battery parameters.

Parameter	Value
Type	Li-NMC
Open circuit voltage	52.5 V
% SOC	90%
Ah rating	25 Ah
Nominal discharge current	10 A

5. Simulation Results

The bidirectional quadratic converter and VSI for the PMBLDC motor are simulated using the MATLAB/Simulink software package. The vehicular load is simulated by an inertial load of 0.1 kg·m^2. The inertial load is connected to a PMBLDC motor having parameters, as given in Table 5. The system is simulated for 7 s with 0–5 s in motoring mode and 5–7 s in regenerative mode. The intended regenerative action is observed as per the simulation results shown in this manuscript. The steady-state inductor currents with a gate driving signal in the converter's boost mode operation are shown in Figure 12.

In boost mode, when the switch is ON, both inductor's current increases, and when the switch is OFF, both inductor's current decreases. In steady-state, the average value of current i_{L1} is 3.3 A, and current i_{L2} is 2.35 A, as shown in Figure 12. Figure 13 shows the steady-state output voltage (V_o), voltage (V_{c1}) of capacitor C_1, and battery voltage (V_i) in boost (motoring) mode operation. In boost mode, the steady-state output voltage V_o is 98 V, and capacitor (C_1) voltage V_{c1} is 68.5 V with battery voltage $V_i = 48$ V at 30% duty ratio, as shown in Figure 13.

The battery voltage (V_i) and state of charge (SOC) are shown in Figure 14. It is depicted that during motoring (boost) mode, the battery SOC decreases, and a dip in battery voltage is observed during 0–5 s of simulation. At $t = 5$ s, regenerative braking is applied; then, the converter starts to operate in buck mode, and battery voltage and SOC increase. In buck (regenerative braking) mode, the steady-state inductor currents are $I_{L1} = -5$ A and $I_{L2} = -4$ A, respectively. The negative value of inductor currents means the current is flowing from load to source, as shown in Figure 15. Figure 16 shows the voltage stress on switches S_1 and S_2 during boost mode operation of the converter.

From time 0 s to time 5 s, the motor speed in boost mode reached 2000 rpm. At 5 s, regenerative braking is applied. As shown in Figure 17, the motor speed starts to decrease in

Table 4: Converter parameters.

Parameter	Value
L_1	1 mH
L_2	1.5 mH
C_1	47 μF
C_2	200 μF

Table 5: Motor parameters.

Parameter	Value
Per phase resistance (R_a)	1.09 Ω
Per phase inductance (L_a)	3.37 mH
Voltage constant (K)	51.3 V/krpm
Inertia (J)	0.00014 kg m^2
Pole pair (P)	2

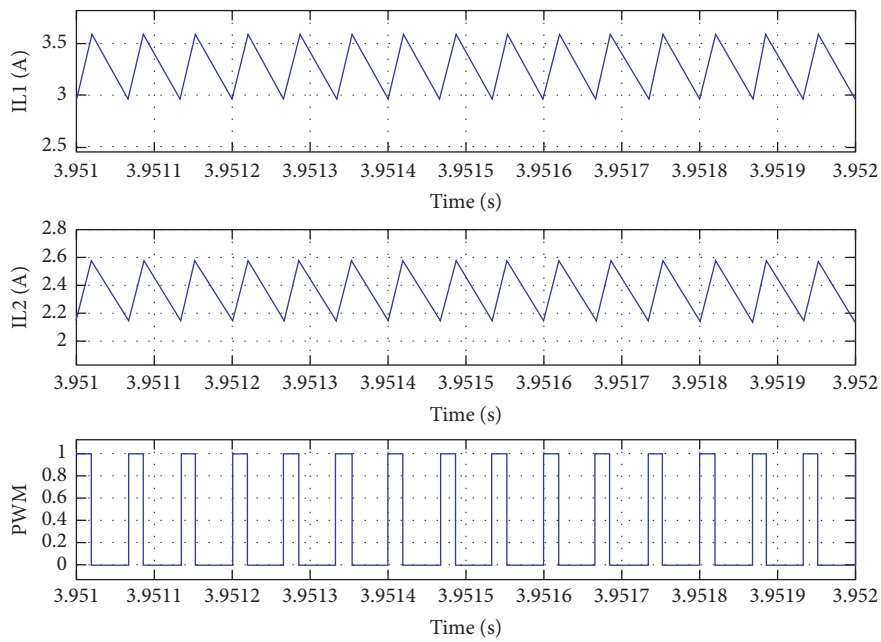

Figure 12: Inductor currents I_{L1} and I_{L2} with switching PWM during boost mode.

braking mode and reaches 650 rpm in 7 s. The performance of the PMBLDC motor under different levels of inertia is simulated in MATLAB. Regenerative braking is applied at different inertial loads, and energy is fed back into the battery from the stored energy of the inertial load. The plot between the percentage energy recovery and inertia is shown in Figure 18.

6. Validation through Developed Prototype

An experimental setup is developed to test the proposed system and the converter prototype. The system employs a 1.1 HP PMBLDC motor coupled with an inertia of the flywheel ($J = 0.1$ kg m^2). The TMS320F28335 DSP microcontroller controls the developed DC-DC converter and the VSI in both the motoring and regenerative modes. Figure 19 shows the setup for the experimental verification of the proposed system.

A PMBLDC motor coupled with a high inertia flywheel is used to emulate the vehicular load. To reduce the impulse torque condition and safety of the system, a pulley belt system is employed for mechanical coupling of the motor and inertial load. Figure 20 shows different voltages, battery voltage, capacitor voltage V_{c1}, and output voltage in a steady state during boost mode operation of the converter at a 30% duty ratio. The steady-state inductor currents I_{L1}, I_{L2}, and switching PWM are shown in Figure 21 for boost mode operation. The waveforms and the values are confirmative of those obtained, as shown in Figure 12. Both the inductors charge during the ON time of the switch and discharge during the OFF time. The voltage stress on switches S_1 and S_2 during the boost mode of the converter is shown in Figure 22. Figure 23 shows the transition of the system operation from motoring to the RB mode.

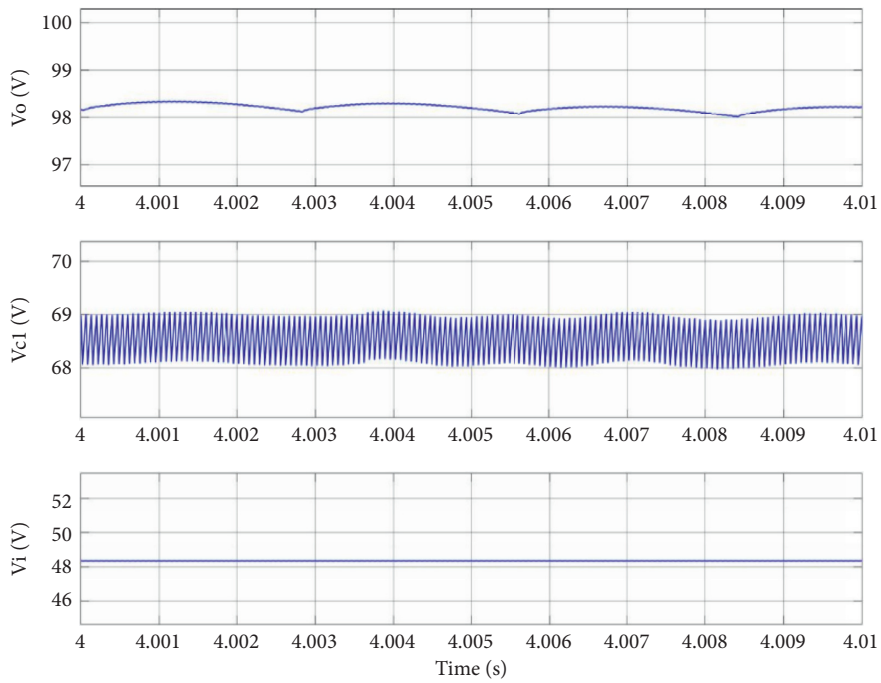

Figure 13: Output voltage V_o, capacitor voltage V_{c1}, and battery voltage V_i during boost mode.

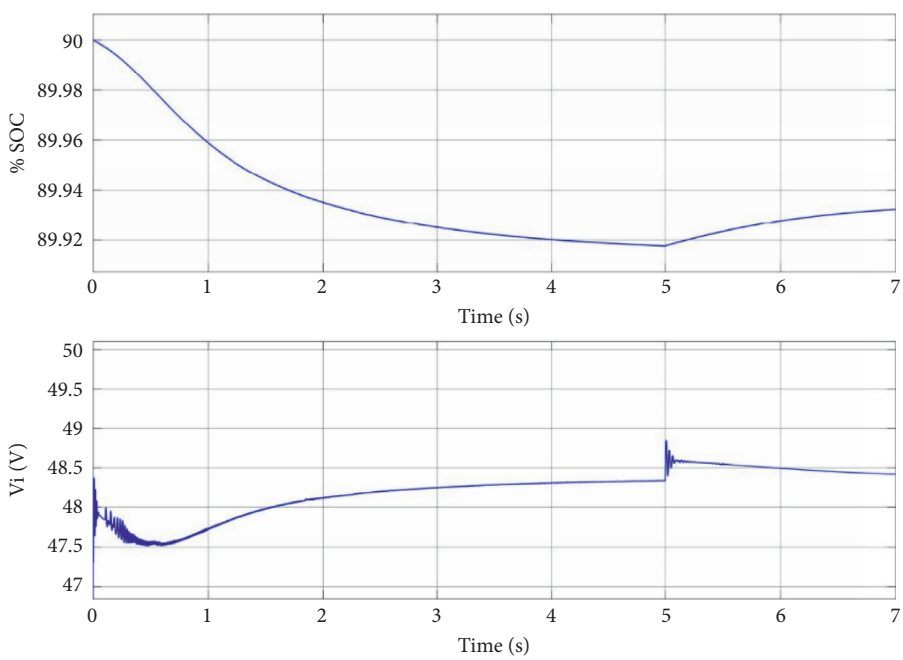

Figure 14: Battery voltage and % SOC during motoring and regenerative braking.

The negative currents are indicative of the regenerative mode operation. During RB, the steady-state inductor currents I_{L1}, I_{L2}, and switching PWM are presented, as shown in Figure 24, aligned with those obtained in the simulation. It indicates the converter operation in the buck mode and the successful energy transfer from the PMBLDC motor to the battery. The value of inductor currents during RB is matched with the simulation result.

The continuous charging of the output capacitor due to VSI performing the boosting operation keeps the DC link voltage almost constant during the initial period of the braking process. The efficiency curve during boost mode is shown in Figure 25.

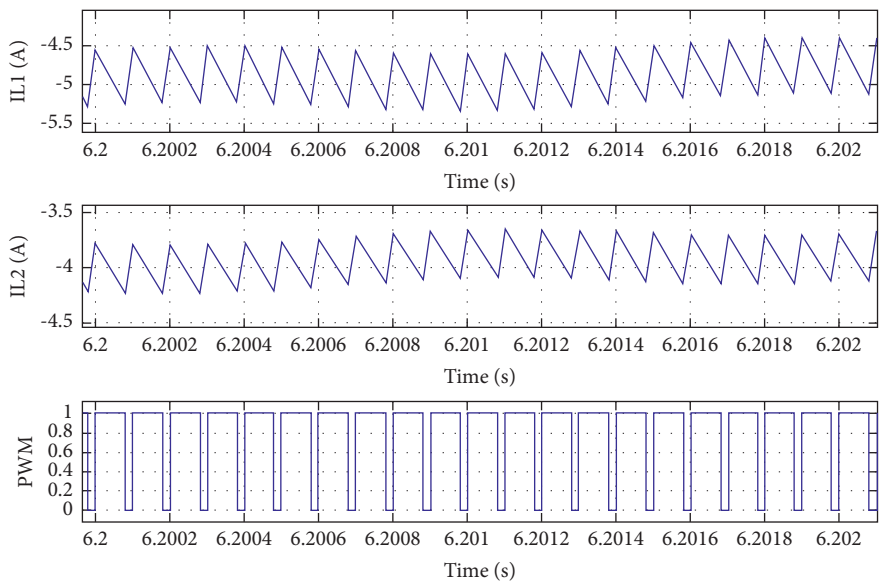

Figure 15: Inductor currents I_{L1} and I_{L2} with switching PWM during regenerative braking.

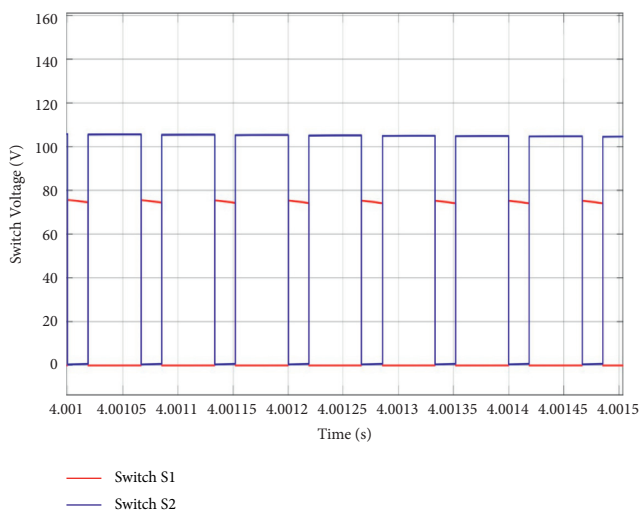

Figure 16: Voltage stress on switches S_1 and S_2 during boost mode operation of the converter.

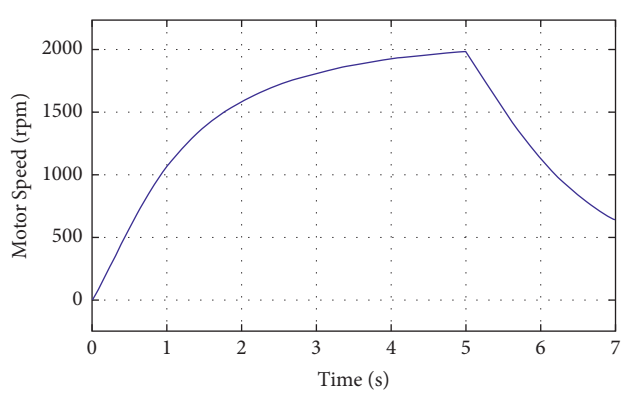

Figure 17: Motor speed characteristics during motoring and regenerative braking.

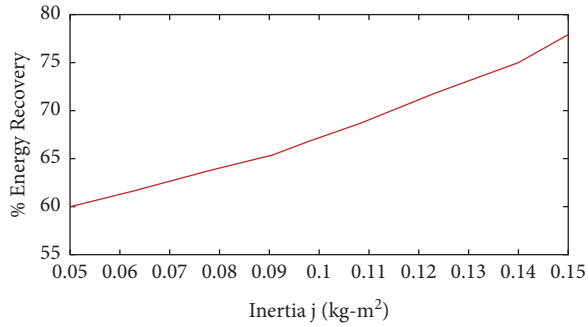

Figure 18: Plot of % energy recovery vs. inertia j (kg m^2).

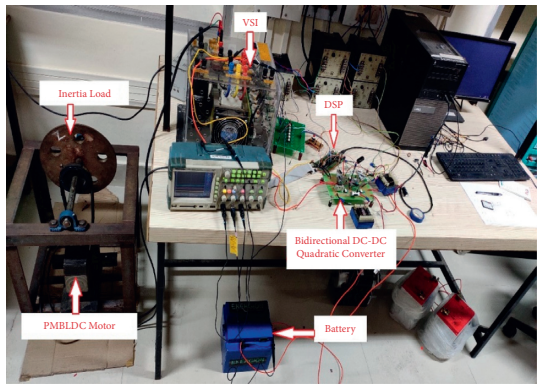

Figure 19: Hardware setup.

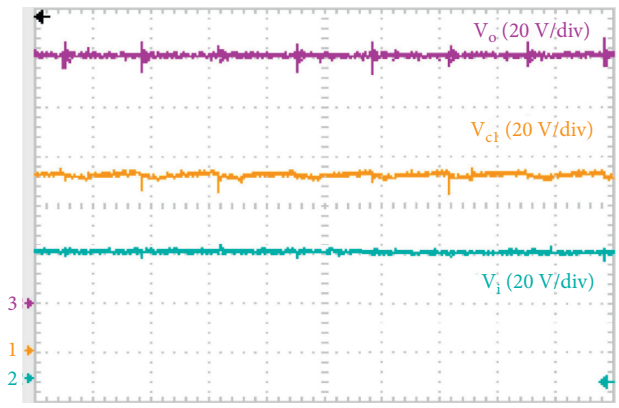

Figure 20: System voltages in steady-state boost operation of the converter: V_{c1} (channel 1); V_i (channel 2); V_o (channel 3).

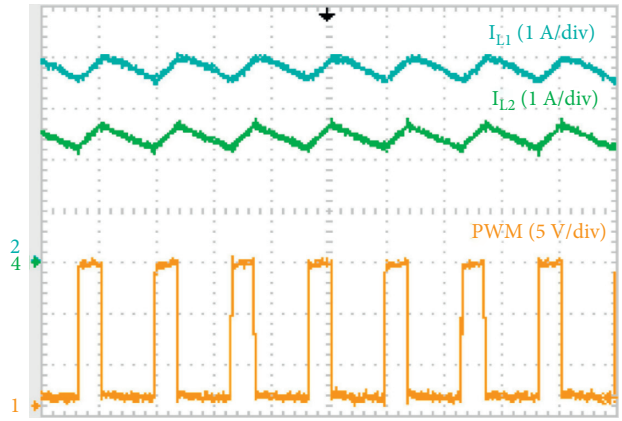

Figure 21: Boost mode operation of the converter: switching PWM (channel 1); I_{L1} (channel 2); I_{L2} (channel 4).

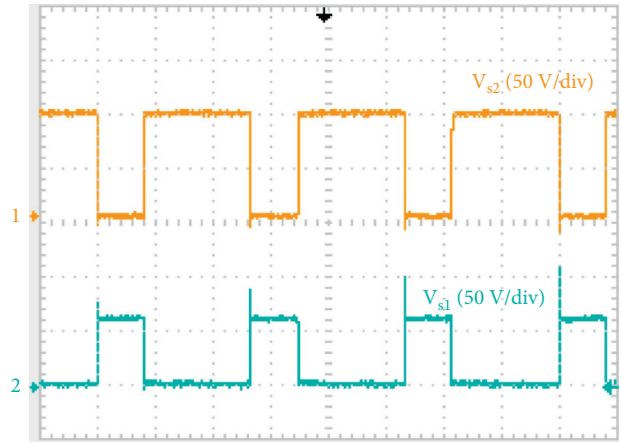

Figure 22: Voltage stress on switches V_{S1} (channel 2) and V_{S2} (channel 1) in boost mode operation of the converter.

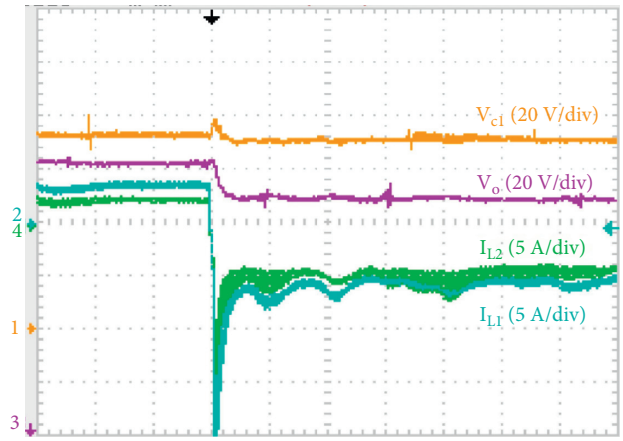

Figure 23: Transition of the motor from motoring mode to regenerative braking mode: V_{c1} (channel 1); I_{L1} (channel 2); V_o (channel 3); I_{L2} (channel 4).

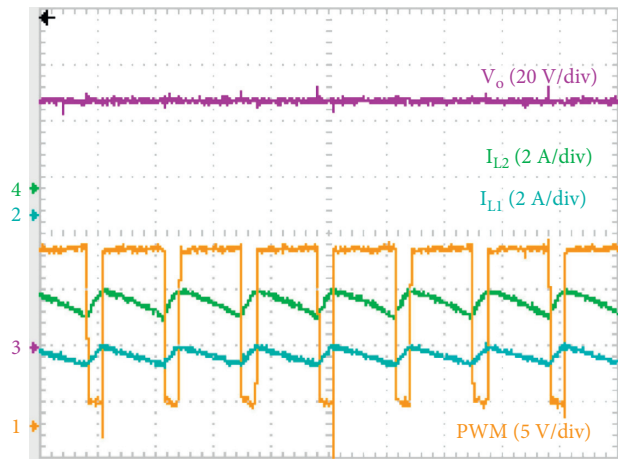

Figure 24: Buck mode operation of the converter: switching PWM (channel 1); I_{L1} (channel 2); V_o (channel 3); I_{L2} (channel 4).

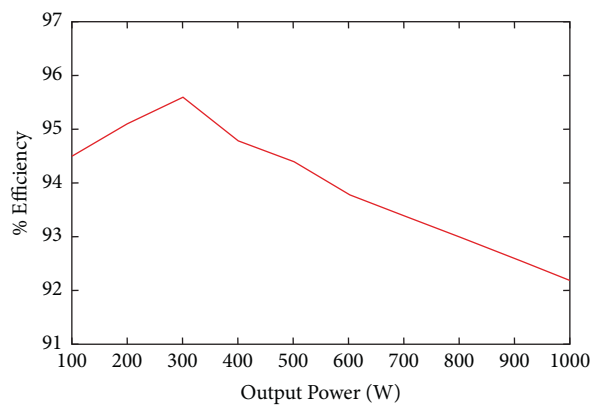

Figure 25: The curve between % efficiency and output power during boost mode.

7. Conclusion

This study designs, develops, and tests a BDQC for RB application in LEV. The power flow direction is controlled successfully by changing the working mode of the VSI and the BDQC. The inertial load's mechanical energy is converted to electrical energy in the regenerative braking and fed back to the battery, as evident from the results. A control strategy is implemented to boost the back EMF of the PMBLDC motor by controlling the VSI and using the self-inductance of the motor. The bidirectional DC-DC quadratic converter operates at a maximum efficiency of 95.4% at a 30% duty ratio during boost mode operation. The implemented strategy and the system configuration proposed in this study have shown an economical and practical approach to eliminate the drawbacks of regenerative braking in the buck mode of BDC.

Data Availability

The data used to support the findings of this study are available from the author Mukesh Kumar upon request (email: mukeshk.rs.eee16@iitbhu.ac.in).

Conflicts of Interest

The authors declare that they have no conflicts of interest.

Acknowledgments

The authors thank the Electrical Machine and Drive Lab of the Department of Electrical Engineering at the Indian Institute of Technology (BHU), Varanasi, Uttar Pradesh, India, and the Department of Electrical and Computer Engineering, Hawassa University, Hawassa, Ethiopia.

References

[1] Z. Wang, P. Wang, B. Li, X. Ma, and P. Wang, "A bidirectional DC-DC converter with high voltage conversion ratio and zero ripple current for battery energy storage system," *IEEE Transactions on Power Electronics*, vol. 36, no. 7, pp. 8012–8027, 2021.

[2] P. S. Tomar, M. Srivastava, and A. K. Verma, "An improved current-fed bidirectional DC-DC converter for reconfigurable split battery in EVs," *IEEE Transactions on Industry Applications*, vol. 56, no. 6, pp. 6957–6967, 2020.

[3] S. Mousavinezhad Fardahar and M. Sabahi, "High step-down/high step-up interleaved bidirectional DC-DC converter with low voltage stress on switches," *IET Power Electronics*, vol. 13, no. 1, pp. 104–115, 2020.

[4] W. Hassan, J. L. Soon, D. Dah-Chuan Lu, and W. Xiao, "A high conversion ratio and high-efficiency bidirectional DC-

DC converter with reduced voltage stress," *IEEE Transactions on Power Electronics*, vol. 35, no. 11, pp. 11827–11842, 2020.

[5] Y. Raj Kafle, M. J. Hossain, and M. Kashif, "Quasi-Z-source-based bidirectional DC-DC converters for renewable energy applications," *International Transactions on Electrical Energy Systems*, vol. 31, Article ID e12823, 2021.

[6] B.-R. Lin and G.-Y. Wu, "Bidirectional resonant converter with half-bridge circuits: analysis, design, and implementation," *Energies*, vol. 11, 2018.

[7] Y. Xie, J. Sun, and J. S. Freudenberg, "Power flow characterization of a bidirectional galvanically isolated high-power DC/DC converter over a wide operating range," *IEEE Transactions on Power Electronics*, vol. 25, no. 1, pp. 54–66, 2010.

[8] Z. Yao and T. Liu, "Boost and full-bridge integrated converter for wide input-voltage range application," *International Transactions on Electrical Energy Systems*, vol. 31, Article ID e12916, 2021.

[9] T. F. Wu, Y. C. Chen, J. G. Yang, and C. L. Kuo, "Isolated bidirectional full-bridge DC-DC converter with a flyback snubber," *IEEE Transactions on Power Electronics*, vol. 25, no. 7, pp. 1915–1922, 2010.

[10] V. Cardoso, S. L. Brockveld Junior, T. B. Lazzarin, and G. Waltrich, "Double boost-flyback converter," *IET Power Electronics*, vol. 13, no. 6, pp. 1163–1171, 2020.

[11] S. Pal, B. Singh, and A. Shrivastava, "An efficient wide input wide output CrCM flyback converter in high-power LED lighting," *International Transactions on Electrical Energy Systems*, vol. 30, Article ID e12445, 2020.

[12] C.-M. Lai, J. Teh, Y.-C. Lin, and Y. Liu, "Study of a bidirectional power converter integrated with battery/ultracapacitor dual-energy storage," *Energies*, vol. 13, 2020.

[13] Y. Mei, Q. Jiang, H. Yang, W. Li, X. He, and S. Li, "Non-isolated stacked bidirectional soft-switching DC-DC converter with PWM plus phase-shift control scheme," *Journal of Modern Power Systems and Clean Energy*, vol. 5, no. 4, pp. 631–641, 2017.

[14] C. C. Lin, L. S. Yang, and G. W. Wu, "Study of a non-isolated bidirectional DC-DC converter," *IET Power Electronics*, vol. 6, no. 1, pp. 30–37, 2013.

[15] A. Sah, K. Chaudhary, and V. V. Ratnam, "Non-isolated multiphase buck-boost converter design for electric vehicle applications," in *Proceedings of the 2014 Annual International Conference on Emerging Research Areas: Magnetics, Machines and Drives (AICERA/iCMMD)*, vol. 1–6, Kottayam, India, July 2014.

[16] M. Kumar, K. Kumar, and K. Chaudhary, "Modified non-isolated bidirectional DC-DC converter for regenerative braking for electric vehicle applications," in *Proceedings of the Symposium on Power Electronic and Renewable Energy Systems Control*, S. Mohapatro and J. Kimball, Eds., pp. 77–88pp. 77–, Bhubaneswar, India, December 2021.

[17] K. Choobdari Omran and A. Mosallanejad, "SMES/battery hybrid energy storage system based on bidirectional Z-source inverter for electric vehicles," *IET Electrical Systems in Transportation*, vol. 8, no. 4, pp. 215–220, 2018.

[18] E. P. Wiechmann, P. Aqueveque, R. Burgos, and J. Rodriguez, "On the efficiency of voltage source and current source inverters for high-power drives," *IEEE Transactions on Industrial Electronics*, vol. 55, no. 4, pp. 1771–1782, 2008.

[19] S. Rostami, V. Abbasi, N. Talebi, and T. Kerekes, "Three-port DC-DC converter based on quadratic boost converter for stand-alone PV/battery systems," *IET Power Electronics*, vol. 13, no. 10, pp. 2106–2118, 2020.

[20] A. R. Saxena and D. Kumar, "Transformerless high-gain battery-integrated DC-DC boost converter for fuel-cell stacks: design, analysis, and control," *International Transactions on Electrical Energy Systems*, vol. 31, Article ID e12722, 2021.

[21] M. Zaid, S. Khan, M. D. Siddique, A. Sarwar, J. Ahmad, and A. Iqbal, "A transformerless high gain dc–dc boost converter with reduced voltage stress," *International Transactions on Electrical Energy Systems*, vol. 31, Article ID e12877, 2021.

[22] G. Li, X. Jin, X. Chen, and X. Mu, "A novel quadratic boost converter with low inductor currents," *CPSS Transactions on Power Electronics and Applications*, vol. 5, no. 1, pp. 1–10, 2020.

[23] V. F. Pires, A. Cordeiro, D. Foito, and J. F. Silva, "Control of bidirectional quadratic DC-DC converters for storage support of DC power grids," in *Proceedings of the 2018 7th International Conference on Renewable Energy Research and Applications (ICRERA)*, pp. 227–232, Paris, France, October 2018.

[24] S.-W. Lee and H.-L. Do, "Quadratic boost DC-DC converter with high voltage gain and reduced voltage stresses," *IEEE Transactions on Power Electronics*, vol. 34, no. 3, pp. 2397–2404, 2019.

[25] X. Nian, F. Peng, and H. Zhang, "Regenerative braking system of electric vehicle driven by brushless DC motor," *IEEE Transactions on Industrial Electronics*, vol. 61, no. 10, pp. 5798–5808, 2014.

[26] F. Naseri, E. Farjah, and T. Ghanbari, "An efficient regenerative braking system based on battery/supercapacitor for electric, hybrid, and plug-in hybrid electric vehicles with BLDC motor," *IEEE Transactions on Vehicular Technology*, vol. 66, pp. 3724–3738, 2017.

[27] K. A. Singh and K. Chaudhary, "Design and development of a new three-phase AC-DC single-stage wind energy conversion system," *IET Power Electronics*, vol. 14, no. 2, pp. 302–312, 2021.